University of Strathclyde

Department of Mechanical & Aerospace Engineering

Metallurgical and mechanical property assessment of advanced grid stiffened structures produced by a modified rolling process

Andrew J H Garrick

A thesis submitted in fulfilment of the requirements for the degree of

Doctor of Philosophy

2023

Declaration of Authenticity and Author’s rights

This thesis is the result of the author’s original research. It has been composed by the author and has not been previously submitted for examination which has led to the award of a degree.

Signed: Drew Garrick

Date: 28/04/2023

Abstract

Advanced grid stiffened structures (AGS) are lightweight structures with a high strength to weight ratio, originally developed for the aerospace industry. Isogrid is a type of AGS which has been employed in a number of high-profile projects from Atlas rockets to the recent James Webb space telescope. The utilisation of AGS structures throughout wider industry is an opportunity to reduce the demand for raw materials and their associated environmental impact; however, the conventional method of AGS production by computer numerically controlled (CNC) milling is time consuming, costly, and creates a high level of material waste. To address this, a modified rolling process was conceived to manufacture Isogrid which is faster with low material waste.

This thesis records the experimental development of the novel rolling method and reports the body of scientific data generated during the microstructural and mechanical assessment of its output. The microstructural evolution during this novel rolling process was characterised via a combination of optical microscopy, electron backscatter diffraction and microhardness measurement. The varying degrees of deformation required to form the Isogrid geometry produced areas of greater and lesser cold work, with commensurate levels of hardness. Rolling Isogrid's asymmetrical geometry also generated shear deformation textures alongside standard rolling textures.

Mechanical testing in tension and bending was performed to explore the impact of the microstructural findings. This work demonstrated that rolled Isogrid is stronger than its CNC milled equivalent in tension and bending and stronger than its billet material in bending. Rolled Isogrid was found to be isotropic in the thickness direction for out of plane loading and more isotropic than the CNC milled Isogrid for in plane loading. Comparisons of both sample groups in their as produced and post-annealed condition revealed the degree to which cold work had strengthened each sample. Fatigue testing was performed to assess the influence of rolled Isogrid's microstructural features on its fatigue performance. Rolled Isogrid performed poorly in comparison to CNC milled Isogrid under fatigue loading. The rolled Isogrid performed poorly in fatigue relative to CNC Isogrid, which was attributed to microstructural inhomogeneity after SEM fractography and supplementary fatigue testing of rolled specimens in the post-annealed condition.

Acknowledgements

I would like to thank my supervisors, Dr Athanasios Toumpis and Professor Alexander Galloway for their tireless support, advice, and mentorship on a professional, academic, and personal level. Their initial faith in this project made it possible, and their continued interest in my development has greatly contributed to my growth over the past few years. It has been a privilege to study under their guidance.

I would like to thank the Advanced Material Research Laboratory for its support of this project, and thank Dr Tiziana Marrocco, Dr Maider Olasolo, and Dr Fiona Sillars for their advice and technical assistance throughout.

I would like to thank James Kelly and James Gillespie for their help, knowledge and experience in the labs, and their friendship over the course of my studies.

I am grateful to be a part of the Mechanical and Aerospace Engineering department, it has been a home from home since I started my undergraduate degree in 2015. I would like to thank the academic staff for their support and guidance and the administrative staff for their help throughout. I would also like to extend my sincere thanks to the MAE workshop for the many hours spent assisting this project.

The support and friendship of Ocean Kinetics Ltd. in supplying materials and advice has been greatly appreciated. I owe much of my development as an engineer to their tutelage and guidance.

Finally, I would not have been able to achieve this work without the support of my wonderful friends and family. I am grateful to my longstanding friends Aidan Redpath, David MacRae, Graye Broughton-Stuart and Connor Knight for their friendship and patience as I've conducted this research. I am also deeply grateful to Amy Kemp, who has been there for me as a caring companion throughout these studies. During this work, I have been lucky to have excellent colleagues who have become close friends. Specifically, I would like to thank Ronnie Woodward, Gihad Karrar, Bea Casares Fernández, Miguel Ubago Torres, Jonathan Draper, Iain Sword, Michail Dellepiane and Andrew England for their camaraderie and friendship.

My parents, James and Elizabeth Garrick, and sister, Lindsay Garrick, have been there every step of the way with love and support. My uncles, John and Jim Ratter have expressed a keen interest in this project from the beginning and have continued to encourage me through engaging discussions on the matter. It is a regret of mine that this project was conceived after my late uncle, Frank Ratter, passed away. I believe he would have taken great interest, and I would like to dedicate this body of work to his memory.

Table of contents

Table of Figures

Table of Tables

Structure of the thesis

This thesis is structured to report each stage in the development and characterisation of the novel Isogrid rolling method in the following manner.

Rather than one literature review, each results chapter begins with an overview of the theory and recent work relevant to its content. Chapter 1 introduces the origins and theory of grid stiffened lightweight materials to provide context to the aims and motivation of this thesis. Chapter 2 reports previously implemented and conventional methods for the production of Isogrid, discussing their advantages and disadvantages to give insight into the current state of Isogrid manufacturing. Chapter 3 details the materials and methods used throughout this work. Chapter 4 reports the design process and implementation of the Isogrid rolling concept, with some preliminary findings on the resultant Isogrid.

Chapter 5 details the microstructural characterisation of rolled Isogrid and CNC milled Isogrid in their as produced and post-annealed conditions. All sample types were sectioned and etched to examine the microstructural evolution which takes place during the novel rolling process and related microhardness maps are provided. Analysis on microstructural texture, and the size and aspect ratio of grains was enabled via electron backscatter diffraction.

The mechanical behaviour of rolled and CNC milled Isogrid is reported in Chapter 6, through tensile and bending tests performed on the same sample groups from Chapter 5. These tests were performed in various orientations to ascertain the isotropy of each sample group. The contribution of cold work to mechanical properties was determined by comparing the results of samples in their as produced and post-annealed conditions.

The fatigue performance of rolled Isogrid and CNC Isogrid is examined and compared in Chapter 7. To this end, samples were subjects to cyclical loading, and failures were analysed via SEM fractography, and S-N curves were plotted. The discussion of fatigue incorporates the results reported within previous chapters, and the differences between rolled Isogrid in its cold worked and post-annealed conditions are explored.

Chapter 8 summarises the major contributions to science throughout each chapter with reference to any relevant results in other chapters, provides concluding comments on the thesis, and details potential directions of future work.

1 Advanced grid stiffened structures and Isogrid

1.1 Lightweight materials and the origins of Isogrid and advanced grid stiffened structures

1.1.1 Material selection, lightweight materials, and shape

Material selection within engineering design is often based on the trade-off between conflicting aims [1.1,1.2]. In structural applications, materials must withstand the weight of the overall structure as well as applied loads [1.3]. In the automotive [1.4,1.5] and aerospace sectors [1.6,1.7], materials must also withstand dynamic loading; however, increasing the overall mass of the vehicle increases dynamic loads, reduces fuel efficiency, and requires more power generation to achieve the same acceleration. The same type of trade-off can be applied to what percentage of a freight ship is cargo and what percentage comprises the containers and structure of the vessel itself [1.8]. In these examples, the mass of the material itself counteracts its function. A popular example of this issue is in the design of a space tether, or elevator, where a structure orbiting in space is connected to the ground by means of a cable to facilitate improved access to space [1.9]. An obstacle limiting the development of such technology is that traditional lightweight materials, including non-metallic materials, are still too dense to produce such a structure, since it would collapse under its own weight [1.10,1.11].

It follows from the above examples that the performance of a lightweight material can be expressed as a ratio of some desired functional property divided by its density (this is then known as a specific property such as specific stiffness, or specific strength) [1.12–1.14]. This is an underpinning concept of the work conducted by Ashby [1.15–1.17] on materials choice and the categorisation and ranking of materials within a materials property space. Using this method, the relative merits of a material for a given application can be obtained by graphing a key property on the y axis (often a mechanical property such as Young's modulus or yield strength) and density on the x axis (Figure 1.1). This type of plot was named an Ashby diagram, and the conceptual domain of properties graphed is referred to in the literature as materials property space [1.18,1.19]. The various regions of the graph show families of materials which exhibit very similar properties and behaviours, and therefore facilitates quick and intuitive comparisons. Graphing a line with a gradient of 1 onto the materials space shown in Figure 1.1 creates a contour of materials which have the same specific stiffness. Any materials above this line have a higher specific stiffness than materials below it, which is a useful result for components in plain tension.

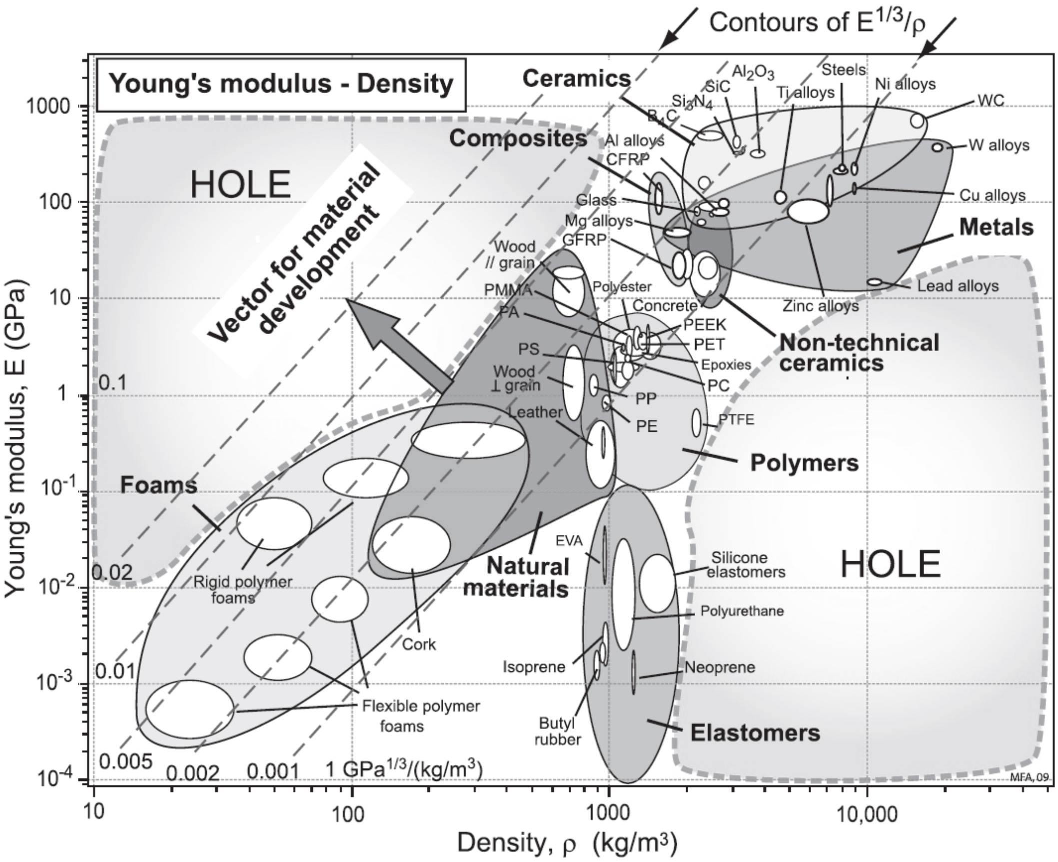

Figure 1.1 An Ashby diagram plotting Young's modulus against density. The dotted lines are contours of equal specific stiffness and material indices for minimal mass design. [1.20].

Using this method, the best possible materials available can be determined for a given purpose [1.17]; however, selecting the optimal material using only one metric is not always appropriate. Other considerations must be taken into account including cost, environmental impact, material availability, and processability [1.17].

Mass efficient design and the use of lightweight materials are environmentally beneficial via the reduction in consumption of raw materials they deliver. Metal production is a large consumer of energy and a significant contributor of CO_2 according to environmental impact reviews of the minerals and mining processing industry [1.21,1.22]. Farjana et al. [1.21,1.22] found that the production of aluminium releases 12kg of CO_2 per kilogramme of aluminium produced. Aluminium was the material with the greatest energy cost identified by Dixit [1.23], as the energy required to electrolyse aluminium from primary ores is high. Engineers and designers are increasingly encouraged by policymakers to consider the ecological impact of their work through the lens of embodied energy [1.24–1.26], which is a measure of the energy required to manufacture a component per unit mass of that component [1.23]. Mitigations such as sourcing carbon neutral energy for production processes and recycling existing aluminium go some way towards reducing this embodied energy; however, the total energy expended, and environmental impact can be directly improved by reducing the overall mass of a component [1.27,1.28]. This line of reasoning was fully explored by Allwood and Cullen [1.29] who support lightweight design and topological optimisation as standard practice for reduced environmental impact.

The areas of material property space in which no materials exist are referred to as holes. These holes represent combinations of material properties which do not currently exist for use within engineering design. The space tether is an excellent example, as it is still a subject of research whether a material exists which could support such an application [1.10,1.11]. There are many such holes where combinations of properties exist capable of enabling future technologies and improving the efficiency and effectiveness of existing processes [1.18,1.19,1.30]. These holes (Figure 1.1) exist between many sets of material properties, especially where one property tends to negate the other, such as ductility and hardness [1.30]. Bulk materials are no longer making significant progress on filling these holes in materials space, so research has shifted towards other methods of tailoring material properties [1.13,1.14,1.20,1.31].

Foams, lattices, hybrid materials and hierarchically designed structures offer the opportunity to develop materials which fill these holes in material property space [1.12,1.18,1.19,1.30]. A review performed by Evans [1.32] gave insight into this progress on these materials, describing the theory underlying their design and their place in the materials property space. This was also demonstrated by Jia et al. [1.30] in their work on the design of hierarchical structures which employed biomimicry to create hybrid materials that exhibit unusual pairings of properties such as “strong and tough “ or “stiff and dissipative”. These materials take full advantage of the shape factor effect, which is a measure of the topological optimisation within a structure relative to some loading regime [1.17]. Ashby [1.17] stated that high strength to mass ratios can be achieved using the shape factor effect regardless of intrinsic properties like yield strength and Young's modulus. I-beams are an example of this concept, as the flanges of an I-beam in bending have been distanced from the neutral axis by the web hence they provide disproportionate bending resistance relative to their weight [1.17]. Shape optimisation has continued to be an effective lightweighting strategy as hybrid materials such as grid stiffened structures and low-density core sandwich panels have consistently performed well and integrated well with novel material technologies [1.12,1.18,1.19,1.30,1.32].

1.1.2 Grid stiffened structures

Grid stiffened structures are a family of hybrid materials composed of a lattice which reinforces an outer shell [1.33]. They utilise the shape factor effect to maximise their strength to mass ratio as a lightweight material in bending as the lattice component creates a high second moment of area [1.34]. This is a design which emulates nature as implementations of the concept can be seen in a diverse array of situations: from the leaves of the Victoria Amazonica or "Amazonian Lilypad" (Figure 1.2-A), which utilises a lattice of turgid water channels to create a stiff floating leaf, to architectural landmarks such as the Crystal palace (Figure 1.2-B) [1.35].

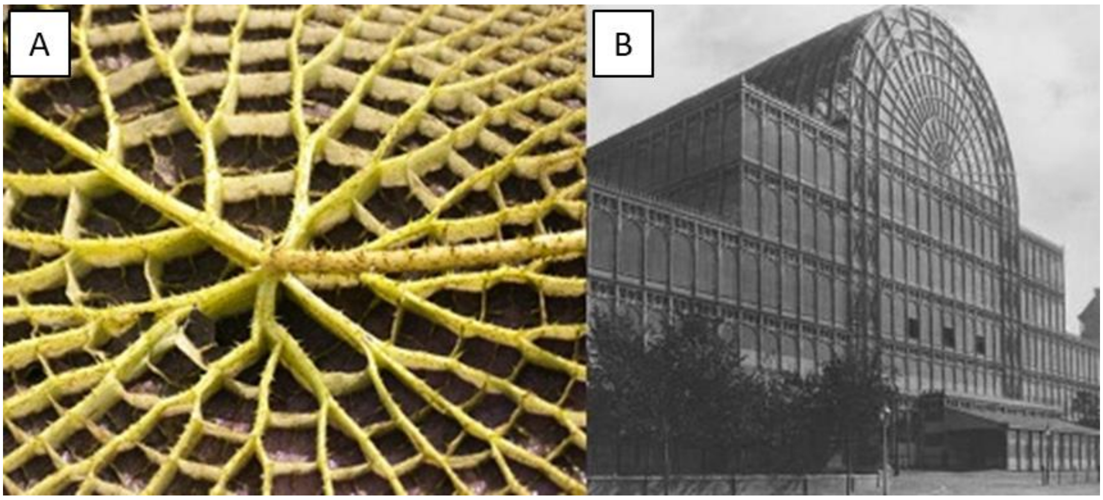

Figure 1.2 Structural ribs on the underside of an Amazonian Lilypad (left) [1.36] and the Crystal palace (right) [1.37] which it inspired.

Grid stiffened structures were introduced as a lightweight design choice for fuselage construction during the rapid development of aerospace vehicles in the 20th century [1.38,1.39]. During World War 2, materials shortages and the need for high performance aircraft gave rise to grid stiffened designs such as the frame of the Vickers Wellington (Figure 1.3-A) [1.40]. Its construction shows that the core concept of skin and stiffened structures was already being considered. In this instance, the fuselages were constructed from many reinforcing elements fastened into a frame, onto which the skin was attached.

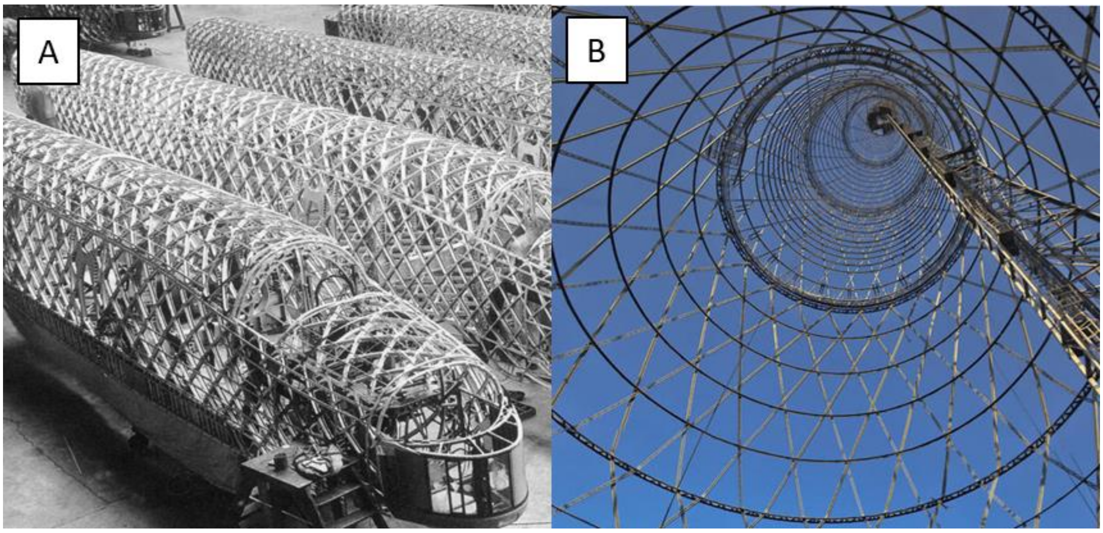

Figure 1.3 The Vickers Wellington, an iconic geodesic fuselage design [1.41]. The Shukhov tower, a precursor to lattice and grid stiffened structures design in Russia [1.42].

The high demand for reliable, lightweight sheet materials for the space industry later in the 20th century coupled with the advent of numerically controlled machining led to the development of “Advanced Grid Stiffened structures” (AGS) or “Integrally stiffened structures” [1.43–1.45]. These materials combined the entire skin and rib structure in one construction with no fasteners or rivets, by machining pockets from thick stock material to produce a thin-walled rib and skin structure [1.46]. These integrally stiffened plate structures, which were initially developed for use in the booster stages of rockets, found usage across multiple aerospace applications in launch vehicles and space structures [1.34,1.47]. While the manufacturing process for the generation of AGS structures was expensive, the reductions in payload related to cost was high enough for viability in these niche aerospace applications [1.34,1.46–1.49]. Vasiliev et al. [1.50] describes a parallel route to the development of AGS and grid structures citing the Moscow radio tower designed by Shukhov [1.42] (Figure 1.3-B) built in 1921 as an early example of lattice style construction.

Grid stiffened structures are particularly optimal for use in bending applications [1.34,1.48,1.51,1.52], where their increased section height has a profound impact on the second moment of area. This is a characteristic shared with cellular materials such as foams and lattices, which often tend to have lower density [1.18,1.53–1.55]. This realisation led to the creation of low density core sandwich panels, with cores made from metallic foams or honeycomb structures. Like I-beams, grid stiffened structures and sandwich panels are both optimised to resist bending loads by placement of the outer skin away from the neutral axis of bending. This takes full advantage of the shape factor effect, removing the concentration of mass from an area where it isn't being loaded effectively [1.4,1.18,1.52,1.56–1.59].

Grid stiffened structures were also developed within civil engineering for large steel and concrete structures [1.60]. Troitsky [1.60] states that this method of construction was developed in lieu of a materials shortage, and that it then gained popularity due to its economic advantages and structural performance. This development took place as a method of conserving available materials, and has remained in usage after the shortages came to an end.

1.1.3 Isogrid

Isogrid is a special case within the family of advanced grid stiffened structures which the Isogrid design handbook defines as "a lattice of intersecting ribs forming an array of equilateral triangles" [1.34]. This lattice of ribs is usually – but not always – attached to a skin section as in other integrally stiffened structures. It has many unique properties which make it attractive compared to other grid stiffened structures, and is instantly recognisably by its triangular pattern as seen in Figure 1.4. The handbook [1.34] provides a comprehensive summary and overview of Isogrid, analyses of its mechanical properties and design data/equations with worked examples for specific use cases.

Isogrid was developed at McDonnel Douglas for the National Aeronautics and Space administration (NASA) as a lightweight material for use within the US space industry [1.34,1.46,1.49,1.61]. NASA had sought to improve on its existing stiffening methodologies which primarily employed square patterns or squares rotated through 45°, often referred to as Orthogrid due to the orthogonal arrangement of its structural members [1.56,1.57,1.62]. Orthogrid performed poorly against in-plane loading due to the statically underdeterminate nature of a quadrangular lattice (the skin section is all that prevents the lattice folding like a scissor mechanism or four bar linkage). This was solved using an equilateral triangular lattice, Isogrid, which performed better than orthogrid in both in-plane and out-of-plane loading due to its statically determinate nature.

Slysh et al. [1.49,1.61] described the benefits, properties and potential usage cases for aluminium Isogrid structures. Isogrid was proposed as the structural component of rocket fairings and adapters as it offered a 37% reduction in weight with a 10% reduction in cost compared to existing methods. The strength of Isogrid in bending, compression and torsion is highly disproportionate to its mass, with one optimised design reported to increase the bending stiffness of the underlying skin 192 times by adding only the skin's weight in ribs [1.34]. These factors made it a clear choice for development and inclusion in several high-profile space industry programs such as Thor-Delta [1.63], Boeing Starliner [1.64] and Skylab [1.34,1.65]. While early development of Isogrid was driven by the need for lightweight materials in the construction of launch vehicles [1.34,1.46,1.61,1.66], other applications quickly became apparent such as fortified military components [1.61] and aircraft fuselages [1.38,1.67]. Greathouse et al. [1.68] used Isogrid as the main structural component for the development of a small Satellite called "Isosat" [1.68]. According to the same report [1.68], Isogrid was also used within the engine shrouds of the Boeing 777. More recently, the Advanced Lattice Structures for Composite Airframes (ALaSCA) project focused on developing an AGS fuselage for aircraft structures [1.69]. The project succeeded in the design of two such concepts, one with the skin on the outside of the plane, the other with the ribs on the exterior covered by a secondary aerodynamic skin.

Secondary benefits of the Isogrid design are its isotropic mechanical properties and high degree of damage resilience [1.34]. Isotropic properties are properties which do not depend on direction [1.70]. The triangular Isogrid lattice displays isotropic mechanical properties which allow the entire lattice to be represented as an equivalent flat layer. This reduces the computational cost of its analysis and optimisation, since it can be represented as a simplified structure. This was attractive given the computational power available during its early development [1.34,1.66]. This is also the origin of Isogrid's name, which came from "Isotropic grid". Further analysis and development of grid stiffened structures has discredited Isogrid as a fully Isotropic material [1.52,1.71], as directionality in properties develop during extreme out of plane deformations and failure modes leading the literature to begin describing it as "quasi isotropic".

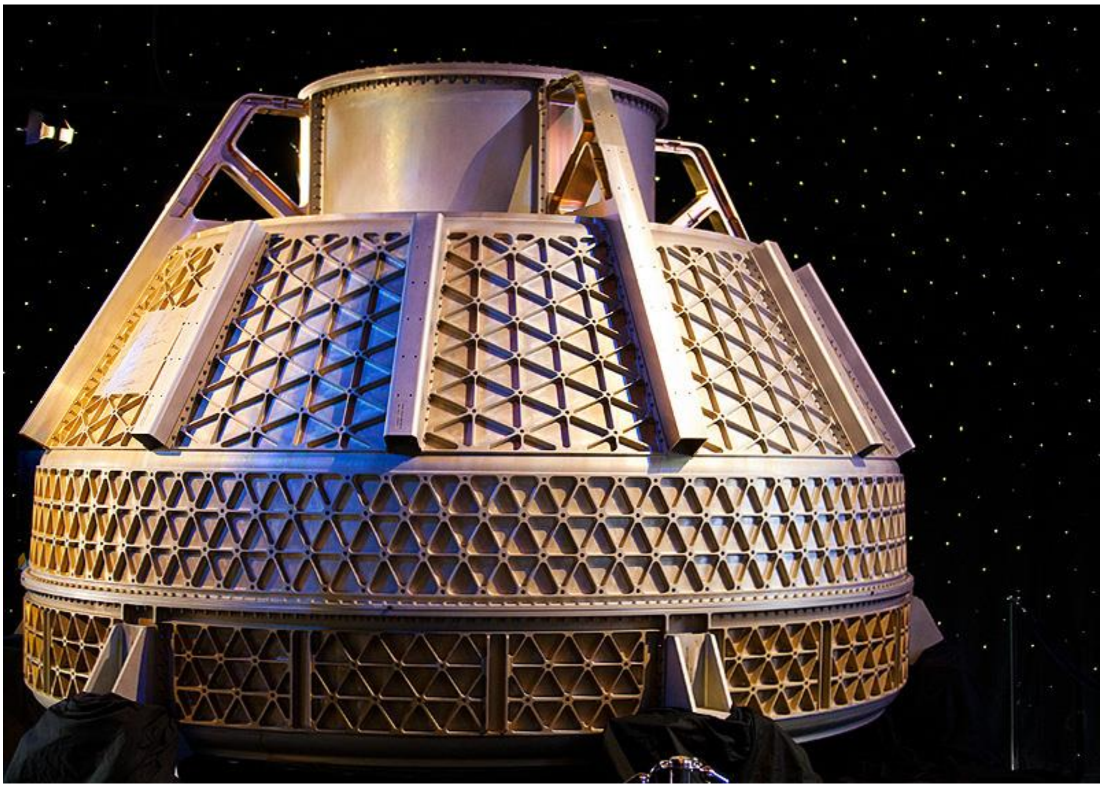

Figure 1.4 Isogrid panels used on the Boeing CST-100 Starliner [1.64].

There is a high degree of redundancy in the loading paths of the Isogrid lattice which makes it very resilient to cut-outs and localised damage [1.34,1.72]. The addition of design features such as doors and bulkheads was easy as the lattice could be reinforced in the area close to the feature. The triangular unit cell of Isogrid lattices fits the circular or arc based geometry which portholes and doors/bulkheads on spacecraft designs often require for strength [1.34,1.48,1.73]. The use of Isogrid reduced the number of components and required section depth in a vessels structural design with comparison to a stringer-skin style construction, while also providing mounting points for instrumentation and secondary systems via blind holes at the nodes [1.34,1.46].

Isogrid continues to see usage in the space industry as a key structural component for the Titan, Atlas and Delta launch vehicles [1.56] with research ongoing for its use in many other projects. The James Webb space telescope is a recent example which employed Isogrid machined from 1.6m panels of isostatically pressed beryllium [1.74–1.78]. Despite the relative age of the technology, technical reports and design studies still recommend the implementation of Isogrid as an advanced material architecture throughout NASA's publicly available documentation [1.74–1.81].

The success of Isogrid within the aerospace industry is in stark contrast to its adoption within other industries. This can mainly be attributed to the cost of manufacturing associated with the methods which have been developed for Isogrid, rather than the utility and merits of the material itself [1.82,1.83].

1.1.4 Computer numerically controlled milling

Computer numerically controlled (CNC) milling was the obvious choice of process for manufacturing integrally stiffened structures such as Isogrid at its inception (Figure 1.5), as it removes the triangular recessed areas of the geometry through a process known as pocket milling. Figure 1.5 shows the advantageous adaptability of CNC milling for Isogrid production, as the method readily creates the change in the rib geometry at the edge of the lattice to a rectangular layout . This may be a reinforced section, or the edge of a component where it must join to a straight edge. This fits very well with the cut-out and reinforcement modifications mentioned in section 2.1.3.

This method is costly due to the large volume of material which must be machined away relative to the remaining structure. A study performed by Tayon et al. [1.82] places this waste volume at 90% of the initial material, incurring a loss of $8 million per tank for the space shuttle program. Other costs must also be considered, including the capital cost for a large custom CNC mill gantry, the time taken to remove >90% of the stock material through machining and the physical space and personnel to process materials in this manner. This combined cost (time, material, energy and machinery) present a barrier for many applications which would benefit from grid stiffened structures.

The primary challenge to reduce the cost of manufacturing Isogrid is to develop a manufacturing method which will facilitate high-volume production [1.84]. CNC machining is an excellent solution for the low volume, high performance rib geometries required within aerospace applications; however, it is not a cost-effective solution for the mass-manufacture of grid stiffened structures which would have potential ecological and performance benefits for many applications at a lower price point [1.85].

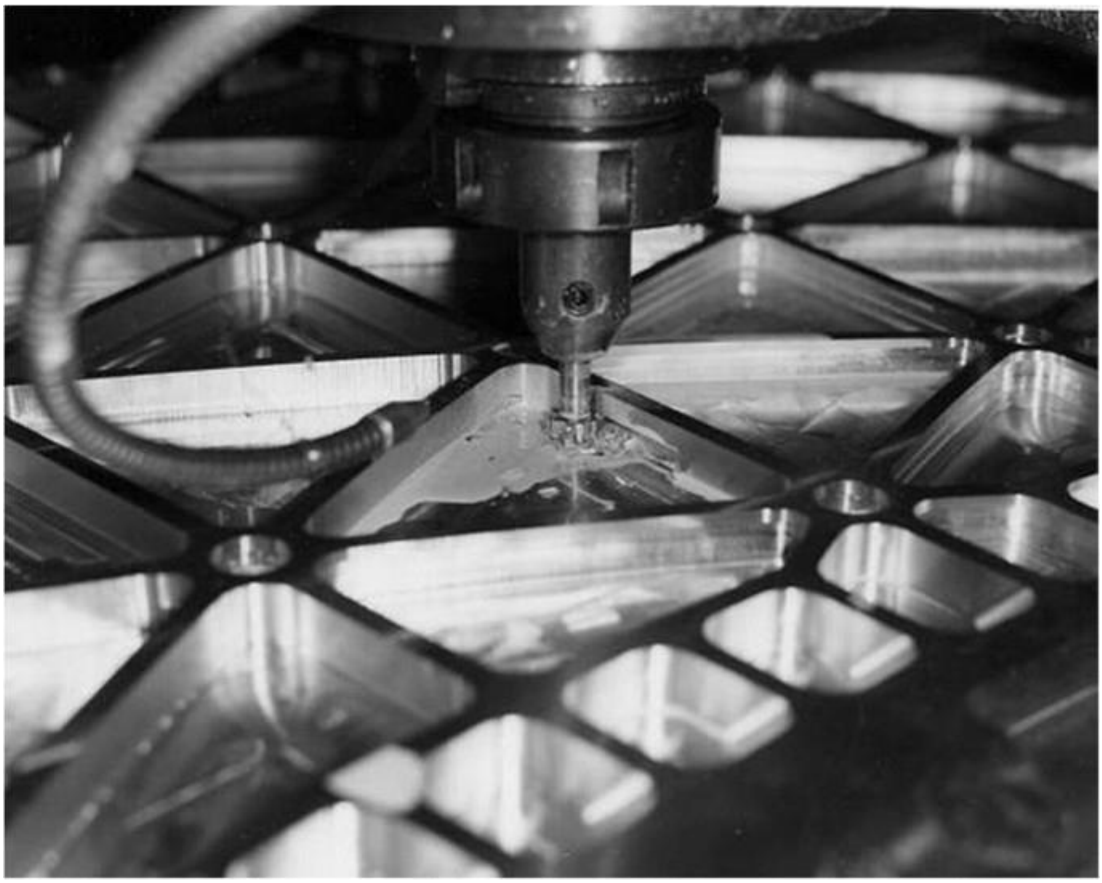

Figure 1.5 Isogrid being machined in a CNC mill [1.86].

1.1.5 Rolling mills

Rolling is a common high-volume manufacturing technique in which a billet is deformed between two metal rollers to reduce its thickness [1.87]. It is highly suited to mass manufacturing of metallic products [1.87,1.88] and is most often employed to produce sheet metal, as it can reliably produce continuous flat sheets with consistent and precise dimensions.

A key characteristic of the rolling process is that the material between the rollers is subjected to 2D stresses in a plane strain deformation mechanism [1.87–1.89]. Material preferentially deforms in the rolling direction and there is minimal lateral material flow [1.90]. As such, the rolling process is often reduced to a 2D simplification for the purposes of analysis, as any cross section taken along the roll gap is experiencing identical conditions [1.87,1.89]. This simplification is practical for calculating forces on the rolling mill, but it breaks down when analysing the rolling process at a more detailed level [1.90,1.91]; for example, forces along the roll gap induce bending into the rollers which must be taken into account for precision rolling. This can lead to the billet exiting the gap with a thickened centre and thinned edges. Several methods have been devised to mitigate this effect, such as roller crowning in which the profile of the roller is reinforced along its length [1.91–1.94] and multi-stand rolling mills in which backup rollers support the primary roller throughout its rotation [1.87,1.93,1.94].

Rolling mills can also be employed to produce other cross-sectional geometries, including structural members (I beams/columns/angle iron), rail tracks, and seamless pipes [1.95–1.97]. These geometries are more complex than the rectangular cross section of sheet metal, so they employ multiple rollers to generate the target cross section. I-beams and railway tracks are rolled using 4-roller mills operating in 2 axes whilst seamless pipes are manufactured using 3 rollers at helical angles to one another, with a trapped mandrel generating the inner diameter [1.95–1.97].

Primary metal production processes are often conducted using both hot and cold rolling depending on the condition of the cast ingot or continuously cast slab. Hot rolling facilitates large deformation and refinement without cracking of the material, whereas cold rolling is utilised where the initial thickness of the cast slab/ingot is closer to the desired output dimension [1.87,1.91].

Further processing can also be performed using rolling mills to harden metallic materials or emboss patterns into them. During cold rolling, the grains of the feed material are deformed, leading to a change in microstructure and material properties [1.98,1.99]. This is often implemented for work hardenable aluminium alloys, which exhibit superior mechanical properties, such as tensile strength, stiffness, and hardness, due to the cold work imparted into their grain structure via cold rolling [1.100,1.101]. Treadplate is a sheet material covered in embossed diamond or chequer patterns for increased surface roughness. These surface properties are designed to facilitate its usage for flooring within industrial contexts and beyond, providing additional grip where there is the potential for slippery conditions. In comparison to grid stiffened structures, treadplate has a shallow surface pattern when compared to the overall thickness of the plate.

Based on the above discussed ability of rolling mills to create patterned materials, this project adapted the rolling process for the production of Isogrid patterns in aluminium plate. The development of such a process for flat sheet materials offers the potential for mass-manufacture of Isogrid sheets within the full context of industrial rolling mill technologies and infrastructure. Flat sheet materials have been the focus of the work conducted during this project; however, the aforementioned alternative applications (rail, structural members, pipe) would benefit from this work.

1.1.6 Motivation, aim and scope of thesis

AGS structures offer excellent mechanical properties and function well as a lightweighting strategy which expands the usable domain of material property space [1.14,1.20,1.50,1.52,1.72]. These structures, such as Isogrid, have been limited to the aerospace industry due to the prohibitive costs for mass production, despite the benefits previously discussed. Isogrid currently excels in bespoke, small-batch applications which value performance above all else, despite the cost [1.74–1.81].

This thesis proposes that a mass production method for Isogrid structures is required for its widespread environmental, economic and performance benefits to be realised outwith the Aerospace industry. For this purpose, the production of Isogrid via a rolling mill method has been investigated, as it is a continuous process, capable of significantly faster production. The impression of ribs to the required depth during a rolling process to produce Isogrid structures is new ground, and the process requires trial and characterisation of its outputs to explore its full potential. An experimental implementation of the process was designed and rolled Isogrid samples were manufactured for mechanical and microstructural comparison to its machined counterpart.

This thesis studies the output of the prototype Isogrid rolling process, in relation to an equivalent CNC milled geometry. The comparison of the two structures across multiple characteristics, such as microstructure, mechanical behaviour and fatigue performance, will facilitate a scientific evaluation of the potential merit of this novel, high-volume manufacturing process.

The aim of this thesis is to assess the viability of the proposed rolling method as a process for the industrial mass production of Isogrid and other advanced grid stiffened structures. To achieve this aim, the following objectives have been identified:

- Selection of an appropriate material for experimental proof of concept trials.
- Design and implementation of the rolling process in the laboratory setting.
- Creation of Isogrid samples using the proof of concept rolling mill and conventional CNC milling methods for comparison.
- Microstructural characterisation of the Isogrid specimens using standard metallographic techniques .
- Mechanical property assessment of the Isogrid specimens in terms of tensile strength, bending strength and fatigue performance.

Modelling approaches to this work would allow exploration and optimisation of the proposed process; however, physical results are more pertinent to the initial assessment of this process. Simulating the large deformations proposed would require bespoke commercial FEA software such as Forge or DEFORM. These software packages represent a large investment in expertise and cost; therefore, strong justification is required for their usage (such as physical results). This work will be done through purely experimental methodologies to provide a clear proof of concept for this process.

1.2 List of references

[1.1] Morimoto T, Kobayashi S, Nagao Y, Iwahori Y. A new cost/weight trade-off method for airframe material decisions based on variable fuel price. Cogent Eng 2017;4. https://doi.org/10.1080/23311916.2017.1285483.

[1.2] Kravchenko M, Pigosso DCA, McAloone TC. Sustainability-related trade-off situations: Understanding needs and criteria. International Design Conference - Design 2020 2020:265–74. https://doi.org/https://doi.org/10.1017/dsd.2020.137.

[1.3] Leslie T, Panchaseelan S, Barron S, Orlando P. Deep space, Thin Walls: Environmental and material precursors to the Postwar Skyscraper. Journal of the Society of Architectural Historians 2018;77:77–96. https://doi.org/10.1525/jsah.2018.77.1.77.

[1.4] Czerwinski F. Current trends in automotive lightweighting strategies and materials. Materials 2021;14. https://doi.org/10.3390/ma14216631.

[1.5] Benedyk JC. Aluminum alloys for lightweight automotive structures. Materials, Design and Manufacturing for Lightweight Vehicles 2010:79–113. https://doi.org/10.1533/9781845697822.1.79.

[1.6] Zhu L, Li N, Childs PRN. Light-weighting in aerospace component and system design. Propulsion and Power Research 2018;7:103–19. https://doi.org/10.1016/j.jppr.2018.04.001.

[1.7] Medikonda S, Sridharan S, Acharya S, Doyle J. Light weighting solutions for additively manufactured aviation components. ASME International Mechanical Engineering Congress and Exposition, Proceedings (IMECE) 2019;2A-2019:1–13. https://doi.org/10.1115/IMECE2019-10805.

[1.8] Buchanan CA, Charara M, Sullivan JL, Lewis GM, Keoleian GA. Lightweighting shipping containers: Life cycle impacts on multimodal freight transportation. Transp Res D Transp Environ 2018;62:418–32. https://doi.org/10.1016/j.trd.2018.03.011.

[1.9] Cartmell MP, McKenzie DJ. A review of space tether research. Progress in Aerospace Sciences 2008;44:1–21. https://doi.org/10.1016/j.paerosci.2007.08.002.

[1.10] Pearson J, Levin E, Oldson J, Wykes H. The lunar space elevator. International Astronautical Federation - 55th International Astronautical Congress 2004 2004;5:3133–43. https://doi.org/10.2514/6.iac-04-iaa.3.8.3.07.

[1.11] Edwards BC. Design and deployment of a space elevator. Acta Astronaut 2000;47:735–44. https://doi.org/10.1016/S0094-5765(00)00111-9.

[1.12] Ashby M. Designing architectured materials. Scr Mater 2013;68:4–7. https://doi.org/10.1016/j.scriptamat.2012.04.033.

[1.13] Evans AG, Hutchinson JW, Ashby MF. Cellular metals n.d.

[1.14] Ashby MF, Bréchet YJM. Designing hybrid materials. Acta Mater 2003;51:5801–21. https://doi.org/10.1016/S1359-6454(03)00441-5.

[1.15] ASM Handbook Committee. Materials Selection and Design. ASM International: Materials Park, OH 1997;20:2005. https://doi.org/10.1007/978-981-4560-38-2.

[1.16] Ashby MF. Selection of Material and Shape. Materials Selection in Mechanical Design 2011:243–76. https://doi.org/10.1016/b978-1-85617-663-7.00009-6.

[1.17] Ashby MF. Overview No. 92: Materials and shape. Acta Metallurgica Et Materialia 1991;39:1025–39. https://doi.org/10.1016/0956-7151(91)90189-8.

[1.18] Ashby MF. Hybrids to fill holes in material property space. Philosophical Magazine 2005;85:3235–57. https://doi.org/10.1080/14786430500079892.

[1.19] Ashby M. Hybrid materials to expand the boundaries of material-property space. Journal of the American Ceramic Society 2011;94:s3–14. https://doi.org/10.1111/j.1551-2916.2011.04559.x.

[1.20] Ashby M. Designing architectured materials. Scr Mater 2013;68:4–7. https://doi.org/10.1016/j.scriptamat.2012.04.033.

[1.21] Farjana SH, Huda N, Parvez Mahmud MA, Saidur R. A review on the impact of mining and mineral processing industries through life cycle assessment. J Clean Prod 2019;231:1200–17. https://doi.org/10.1016/j.jclepro.2019.05.264.

[1.22] Farjana SH, Huda N, Mahmud MAP. Impacts of aluminum production: A cradle to gate investigation using life-cycle assessment. Science of the Total Environment 2019;663:958–70. https://doi.org/10.1016/j.scitotenv.2019.01.400.

[1.23] Dixit MK. Embodied energy and cost of building materials: correlation analysis. Building Research and Information 2017;45:508–23. https://doi.org/10.1080/09613218.2016.1191760.

[1.24] Sustainability and Net Zero Design Guide-Sustainability Annex. 2022.

[1.25] Liu Z, Geng Y, Lindner S, Zhao H, Fujita T, Guan D. Embodied energy use in China’s industrial sectors. Energy Policy 2012;49:751–8. https://doi.org/10.1016/j.enpol.2012.07.016.

[1.26] Curmi L, Weththasinghe KK, Tariq MAUR. Global Policy Review on Embodied Flows: Recommendations for Australian Construction Sector. Sustainability 2022;14:14628. https://doi.org/10.3390/su142114628.

[1.27] Paraskevas D, Kellens K, Van De Voorde A, Dewulf W, Duflou JR. Environmental Impact Analysis of Primary Aluminium Production at Country Level. Procedia CIRP 2016;40:209–13. https://doi.org/10.1016/j.procir.2016.01.104.

[1.28] Brough D, Jouhara H. The aluminium industry: A review on state-of-the-art technologies, environmental impacts and possibilities for waste heat recovery. International Journal of Thermofluids 2020;1–2. https://doi.org/10.1016/j.ijft.2019.100007.

[1.29] Allwood JM, Cullen JM. Sustainable materials with both eyes open. Cambridge: 2012.

[1.30] Jia Z, Yu Y, Wang L. Learning from nature: Use material architecture to break the performance tradeoffs. Mater Des 2019. https://doi.org/10.1016/j.matdes.2019.107650.

[1.31] Czerwinski F. Current trends in automotive lightweighting strategies and materials. Materials 2021;14. https://doi.org/10.3390/ma14216631.

[1.32] Evans AG. Lightweight Materials and Structures. MRS Bull 2001;26:790–7. https://doi.org/10.1557/mrs2001.206.

[1.33] Huybrechts SM, Meink TE, Wegner PM, Ganley JM. Manufacturing theory for advanced grid stiffened structures. Compos Part A Appl Sci Manuf 2002. https://doi.org/10.1016/S1359-835X(01)00113-0.

[1.34] Meyer RR, Harwood OP, Harmon MB, Orlando JI. Isogrid design handbook. NASA 1973.

[1.35] Pollard J. The eccentric engineer: taking inspiration from nature for the Crystal Palace. IET n.d. https://eandt.theiet.org/content/articles/2019/10/the-eccentric-engineer-taking-inspiration-from-nature-for-the-crystal-palace/ (accessed June 18, 2021).

[1.36] Amazonian Lilypad n.d. https://www.nybg.org/blogs/plant-talk/2012/08/gardens-and-collections/botanical-behemoth/ (accessed June 18, 2021).

[1.37] Crystal Palace Building London. Encyclopaedia Britannica n.d. https://www.britannica.com/topic/Crystal-Palace-building-London.

[1.38] Vasiliev V v., Razin AF. Anisogrid composite lattice structures for spacecraft and aircraft applications. Compos Struct 2006;76:182–9. https://doi.org/10.1016/j.compstruct.2006.06.025.

[1.39] Wegner PM, Ganley JM, Huybrechts SM, Meink TE. Advanced grid stiffened composite payload shroud for the OSP launch vehicle. IEEE Aerospace Conference Proceedings 2000;4:359–65. https://doi.org/10.1109/aero.2000.878447.

[1.40] Tsai SW. Manufacture and design of composite grids. Technical Report 1997;1997:59–71. https://doi.org/10.3989/mc.1997.v47.i247-248.495.

[1.41] BAE Systems. Vickers Wellington B Mk1 https://www.baesystems.com/en/heritage/vickers-wellington (accessed June 18, 2021).

[1.42] World Monument Fund. The Shukhov tower https://www.wmf.org/project/shukhov-tower (accessed June 18, 2021).

[1.43] Wagner J, Domack M, Tayon W, Bird RK. Innovative Manufacturing of Launch Vehicle Structures - Integrally Stiffened Cylinder Process. Nasa 2017:2016–7.

[1.44] Lam ACL, Shi Z, Yang H, Wan L, Davies CM, Lin J, et al. Creep-age forming AA2219 plates with different stiffener designs and pre-form age conditions: Experimental and finite element studies. J Mater Process Technol 2015;219:155–63. https://doi.org/10.1016/j.jmatprotec.2014.12.012.

[1.45] Pettit RG, Wang JJ, Toh C, Metschan S. Validated Feasibility Study of Integrally Stiffened Metallic Fuselage Panels for Reducing Manufacturing Costs Cost Assessment of Manufacturing / Design Concepts. Technical Report: NASA/CR-2000-209342 2000.

[1.46] Slysh P. Picking the best high-strength, lightweight structures. Machine Design 1990;62:85–9.

[1.47] Meyer RR, March V. Isogrid - A Simple, Efficient, Stiffening Concept. NASA 1973. https://doi.org/10.2514/6.1973-365.

[1.48] Slysh P. Isogrid Structures Technology and Applications. San Diego: Society for Allied Weight Engineers; n.d.

[1.49] Slysh P, Ringwald RS, Dyer JE, Browing DL. 1063. Isogrid Weight Optimum Structures. 34th Annual Conference, Seattle, Washington, May 5-7 1975.

[1.50] Vasiliev V v., Barynin VA, Rasin AF. Anisogrid lattice structures - Survey of development and application. Compos Struct 2001. https://doi.org/10.1016/S0263-8223(01)00111-8.

[1.51] Totaro G. Flexural, torsional, and axial global stiffness properties of anisogrid lattice conical shells in composite material. Compos Struct 2016;153:738–45. https://doi.org/10.1016/j.compstruct.2016.06.072.

[1.52] Huybrechts S, Tsai SW. Analysis and behavior of grid structures. Compos Sci Technol 1996;56:1001–15. https://doi.org/10.1016/0266-3538(96)00063-2.

[1.53] Li G, Chakka VS. Isogrid stiffened syntactic foam cored sandwich structure under low velocity impact. Compos Part A Appl Sci Manuf 2010. https://doi.org/10.1016/j.compositesa.2009.10.007.

[1.54] Banhart J, Seeliger HW. Aluminium foam sandwich panels: Manufacture, metallurgy and applications. Adv Eng Mater 2008;10:793–802. https://doi.org/10.1002/adem.200800091.

[1.55] Merklein M, Geiger M. New materials and production technologies for innovative lightweight constructions. J Mater Process Technol, vol. 125–126, 2002, p. 532–6. https://doi.org/10.1016/S0924-0136(02)00312-6.

[1.56] Huybrechts SM, Hahn SE, Meink TE. Grid Stiffened Structures: A Survey of Fabrication Analysis and Design Methods. International Conference on Composite Materials 1999.

[1.57] Jiang S, Sun F, Fan H, Fang D. Fabrication and testing of composite orthogrid sandwich cylinder. Compos Sci Technol 2017. https://doi.org/10.1016/j.compscitech.2017.02.009.

[1.58] Birman V, Kardomateas GA. Review of current trends in research and applications of sandwich structures. Compos B Eng 2018. https://doi.org/10.1016/j.compositesb.2018.01.027.

[1.59] Mccarville D, Hilburger MW. Modeling and Analysis of Fluted-Core Composite Structures for Aerospace Applications. NASA Report 2021.

[1.60] Troitsky MS, Azad AK. Stiffness Method of Analysis of Orthotropic Steel Bridge Deck. 1973:311–2.

[1.61] Slysh P. Isogrid Structural Applications. Conference of the Society of Allied Weight Engineers 1976:27.

[1.62] Jaunky N, Knight NF, Ambur DR. Formulation of an improved smeared stiffener theory for buckling analysis of grid-stiffened composite panels. Compos B Eng 1996;27:519–26. https://doi.org/10.1016/1359-8368(96)00032-7.

[1.63] Knighton D. Delta Launch Vehicle Isogrid Structure Nastran Analysis. 1972.

[1.64] Photo by Bob Montanaro. The CST-100 Starliner https://rangetracking.com/2015/11/14/cst-100-starliner-pressure-vessel/ (accessed June 18, 2021).

[1.65] Smithsonian. Inside Skylab Orbital Workshop 2020. https://airandspace.si.edu/multimedia-gallery/4571640jpg?id=4571 (accessed February 5, 2020).

[1.66] Slysh P, Dyer JE, Furman JH, Key JE. Isogrid Structures. AIAA/ASME/SAE 16th Structures, Structural Dynamics, and Materials Conference 1975. https://doi.org/10.2514/6.1975-816.

[1.67] Świech L. Experimental and numerical studies of low-profile, triangular grid-stiened plates subjected to shear load in the post-critical states of deformation. Materials 2019;12. https://doi.org/10.3390/ma12223699.

[1.68] Greathouse JP, Hines M v, Jezak KK, Moore RG, Nielsen RM, Ridenoure R. The isosat small satellite a design in isogrid technology n.d.

[1.69] Hühne C. Advanced Lattice Structures for Composite Airframes (ALaSCA) Project Final Report. German Aerospace Centre, Brauhnschweig: 2013.

[1.70] Ericksen JL, Rivlin RS. Stress-Deformation Relations for Isotropic Materials. Journal of Rational Mechanics and Analysis 1955;4:911–1013.

[1.71] Totaro G, de Nicola F. Recent advance on design and manufacturing of composite anisogrid structures for space launchers. Acta Astronaut 2012;81:570–7. https://doi.org/10.1016/j.actaastro.2012.07.012.

[1.72] Huybrechts S, Meink TE. Advanced grid stiffened structures for the next generation of launch vehicles. IEEE Aerospace Applications Conference Proceedings, vol. 1, 1997, p. 263–9. https://doi.org/10.1109/aero.1997.574417.

[1.73] Sabu A, Ss R, Jose A. Design of an Interstage Structure in Launch Vehicle : Isogrid Construction. International Research Journal of Engineering and Technology 2019:940–4.

[1.74] Kendrick SE, Reed T, Streetman S, Byrd DA, Hadaway JB. Design and test of semirigid beryllium mirrors for lightweighted space applications: SBMD cryogenic performance update and AMSD design approach. Optomechanical Engineering 2000, vol. 4198, SPIE; 2001, p. 221–9. https://doi.org/10.1117/12.417345.

[1.75] Kendrick SE, Reed T, Streetman S. In-process status of the 1.4-m beryllium semi-rigid Advanced Mirror System Demonstrator (AMSD). Optical Manufacturing and Testing IV, vol. 4451, SPIE; 2001, p. 58–66. https://doi.org/10.1117/12.453654.

[1.76] Hadaway JB, Geary JM, Reardon PJ, Peters BR, Stahl HP, Eng R, et al. Cryogenic optical testing results for the Subscale Beryllium Mirror Demonstrator (SBMD). Optical Manufacturing and Testing IV, vol. 4451, SPIE; 2001, p. 15–26. https://doi.org/10.1117/12.453625.

[1.77] Chaney DM, Brown RJ, Kendrick SE, Reardon PJ, Hadaway JB, Carpenter J, et al. Results of the beryllium AMSD mirror cryogenic optical testing. Optical, Infrared, and Millimeter Space Telescopes, vol. 5487, SPIE; 2004, p. 833. https://doi.org/10.1117/12.549956.

[1.78] Nella J, Atkinson C, Bronowicki A, Bujanda E, Cohen A, Davies D, et al. James Webb Space Telescope (JWST) observatory architecture and performance. A Collection of Technical Papers - AIAA Space 2004 Conference and Exposition, vol. 2, 2004, p. 1383–95. https://doi.org/10.1117/12.548928.

[1.79] Papathakis K v. Design and Development of Nano-electro Fuel Batteries and Rim-driven Motors for Electrified Aircraft Applications. 2021.

[1.80] Oleson S, Schmitz PC, Runyon K, Bussey B, Ostdiek P, Colozza AJ, et al. Dynamic Radioisotope Power System (DRPS) Permanently Shadowed Region (PSR) Demonstrator Rover 2021.

[1.81] Oleson S, Fittje J, Schmitz P, Tian L, Klefman B, Korn S, et al. Power System Design Trades for a Pressurized Lunar / Mars Rover 2019.

[1.82] Tayon WA, Rudd MT, Domack MS, Hilburger MW. Development of Advanced Manufacturing Approaches for Single-Piece Launch Vehicle Structures 2022.

[1.83] Ivanco ML, Domack MS, Stoner MC, Hehir AR. Cost-benefit analysis for the advanced near net shape technology (ANNST) method for fabricating stiffened cylinders. AIAA Space and Astronautics Forum and Exposition, SPACE 2016 2016:1–19. https://doi.org/10.2514/6.2016-5488.

[1.84] A J Allen AJ, K G Swift KG. Manufacturing Process Selection and Costing. Proc Inst Mech Eng B J Eng Manuf 1990;204:143–8. https://doi.org/10.1243/PIME_PROC_1990_204_057_02.

[1.85] Hashish M. Controlled-depth milling of isogrid structures with AWJs. Journal of Manufacturing Science and Engineering, Transactions of the ASME 1998. https://doi.org/10.1115/1.2830106.

[1.86] Slysh P. Image of isogrid being milled. Isogrid SST Website 2014. http://web.archive.org/web/20140315131052/http://isogrid-sst.com/Machine Design5.JPG (accessed March 15, 2014).

[1.87] Lenard JG. Primer on Flat Rolling. 2007. https://doi.org/10.1016/B978-0-08-045319-4.X5000-1.

[1.88] Malinowski Z, Pietrzyk M, Lenard JG. Analysis of the flat-rolling process: one-dimensional and finite-element models. Journal of Materials Processing Tech 1993;39:373–87. https://doi.org/10.1016/0924-0136(93)90170-B.

[1.89] Barata Marques MJM, Martins PAF. A solution to plane strain rolling by the weighted residuals method. Int J Mech Sci 1990;32:817–27. https://doi.org/10.1016/0020-7403(90)90161-B.

[1.90] Ren Z, Xiao H, Liu X, Yan Z. An analysis of the metal transverse flow in the roll gap for ultra-thin strip rolling using the energy method. ISIJ International 2018;58:309–15. https://doi.org/10.2355/isijinternational.ISIJINT-2017-519.

[1.91] Ataka M. Rolling technology and theory for the last 100 years: The contribution of theory to innovation in strip rolling technology. ISIJ International 2015;55:89–102. https://doi.org/10.2355/isijinternational.55.89.

[1.92] Tseng AA, Tong SX, Chen TC. Thermal expansion and crown evaluations in rolling processes. Mater Des 1996;17:193–204. https://doi.org/10.1016/S0261-3069(96)00061-1.

[1.93] Overhagen C, Mauk PJ. A fast three-dimensional model for strip rolling. Key Eng Mater 2016;716:566–78. https://doi.org/10.4028/www.scientific.net/KEM.716.566.

[1.94] Ma X, Wang D, Liu H. Coupling Mechanism of Control on Strip Profile and Flatness in Single Stand Universal Crown Reversible Rolling Mill. Steel Res Int 2017;88:1–10. https://doi.org/10.1002/srin.201600495.

[1.95] Jewett RA. Structural Antecedents of the I-Beam , 1800-1850 Published by : The Johns Hopkins University Press and the Society for the History of Technology Stable URL : https://www.jstor.org/stable/3101720 REFERENCES Linked references are available on JSTOR for this 1967;8:346–62.

[1.96] Zhang W, Zhu C, Widera GEO. On the use of the upper-bound method for load determination in H-beam rolling. Adv Mat Res 2012;418–420:820–33. https://doi.org/10.1016/0924-0136(95)01895-6.

[1.97] Akiyama M, Tsubouchi K, Tsumura M, Hori H. A study of the mechanism of crack initiation on a mandrel bar for mandrel mill rolling in a seamless tube. Proceedings of the Institution of Mechanical Engineers, Part J: Journal of Engineering Tribology 2000;214:179–87. https://doi.org/10.1243/1350650001543098.

[1.98] Zaidi MA, Sheppard T. Development of microstructure throughout roll gap during rolling of aluminium alloys. Metal Science 1982;16:229–38. https://doi.org/10.1179/030634582790427334.

[1.99] Hirsch J. Texture evolution during rolling of aluminium alloys. TMS Light Metals 2008:1071–7.

[1.100]ASM Handbook Committee. ASM Handbook Volume 2: Properties and Selection: Nonferrous Alloys and Special-Purpose Materials. ASM International; 1990.

[1.101]Bay N. Cold forming of aluminium-state of the art 2000;71:76–90.

2 Production methods of Isogrid

This chapter is a review of the available scientific and technical literature on current manufacturing methods for Isogrid structures and other AGS structures, providing context for informed evaluation of the Isogrid rolling technique with conventional CNC milling methods in later chapters.

2.1 *Existing literature reviews on the manufacturing of Isogrid*

The development of manufacturing methods for Isogrid has been driven by the persistent high cost of its production processes as discussed in chapter 1 [2.1,2.2]. Huybrechts et al. [2.1,2.3–2.5] extensively researched the origins, fabrication techniques and properties of advanced grid stiffened structures. Their body of work discusses the initial implementations of Isogrid, based primarily in metals for aerospace and military applications, but focuses on future developments for the technology in the space industry. Huybrechts et al. [2.1] state that although aluminium Isogrid is a proven and reliable structure, its mass efficiency and cost of production make it undesirable in comparison to composite grid stiffened structures. However, recent developments in forming, welding and additive manufacturing have led to a revived interest in metal-based lattice materials [2.6–2.13].

Vasiliev et al. [2.14,2.15] conducted a survey of the development of Anisogrid, which is an Isogrid derivative. Anisogrid structures are identical to Isogrid structures in their definition except that the rib lattice does not contain nodes where all 3 rib orientations intersect [2.11,2.13–2.15]. Instead, the ribs are offset as seen in Figure 2.1. Vasiliev et al. [2.14] concluded that Anisogrid lattice structures had potential for usage outside the space industry, citing aircraft components and structural elements of civil engineering installations as suitable applications. However, the proprietary and often classified nature of Isogrid's origins had prevented international cooperation in the development of this technology [2.14]. For this reason, it was noted that the review by Huybrechts et al. [2.1] was an incomplete record of technological progress to date [2.14]. To the same end, it should be considered that there may still be classified documents relevant to this body of work.

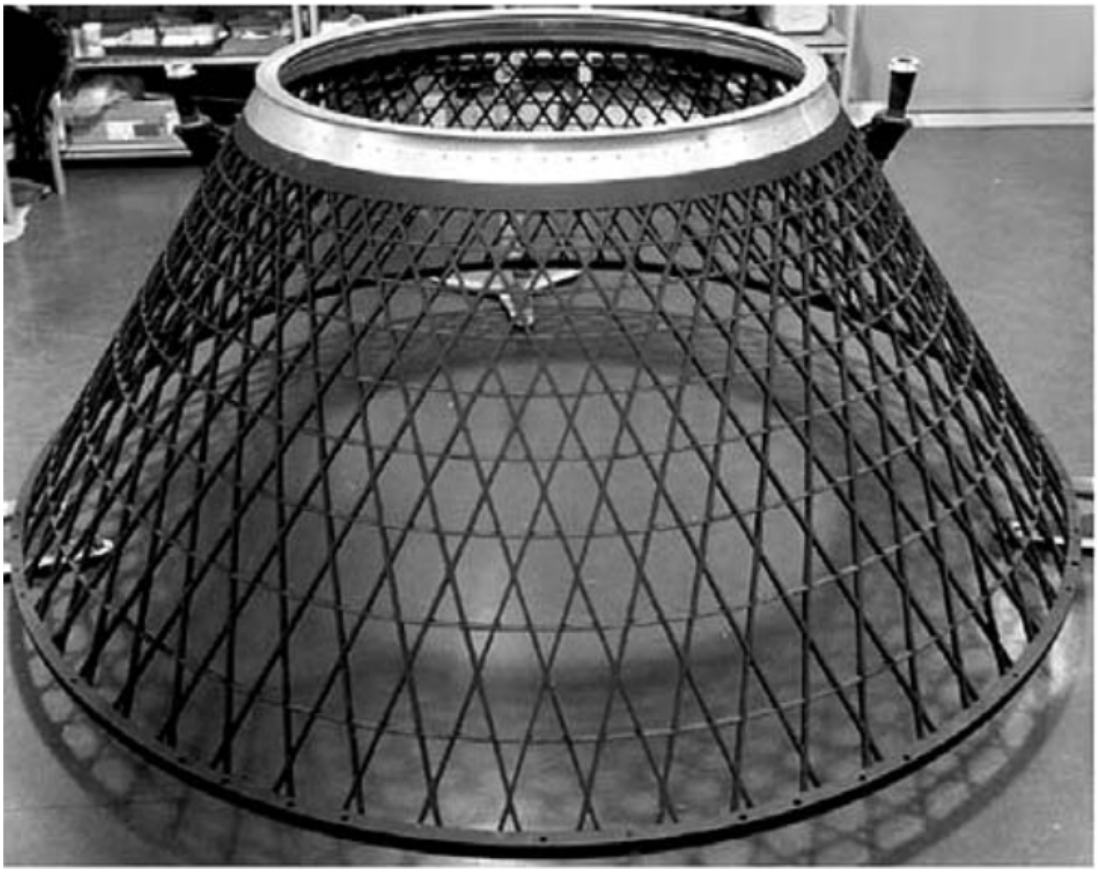

Figure 2.1 Anisogrid structure [2.14]

2.2 Milling

The original manufacturing method for metallic Isogrid and other AGS structures as discussed in chapter 1 was manual milling [2.16]. These machines were operated by skilled machinists to remove material in a time-consuming and high material waste process with a rotating cutter on an XYZ gantry. The time taken to produce 10 Isogrid components (approximately 150x150x15mm) in this manner was calculated by Schultz [2.16] as 712 operator-hours (30 days). In the same article [2.16], numerically controlled (NC) milling was shown to take 332 hours (14 days), which was 2.15 times faster due to automation [2.16]. The material waste of milling Isogrid is up to 90% of the base material [2.2,2.17,2.18].

The time taken to manufacture Isogrid via milling is compounded by post processing requirements [2.19]. To obtain a usable final geometry for applications such as structural rocket panels, the milled Isogrid sheets are formed into cylindrical sections using rollers or a break press [2.17,2.19]. Figure 2.2 shows all the steps in an extended Isogrid manufacturing process, where computer numerically controlled (CNC) milling was used to create the initial Isogrid structure. Complex curvature was difficult to obtain using these post-processing methods, so components using Isogrid were restricted to cylindrical or conical forms [2.17,2.19–2.22]. Slysh [2.19] described a wide range of processes to achieve more advanced geometries. These include explosive forming [2.19] (Figure 2.2), hydrostatic pressing [2.19] and creep age forming [2.19,2.23]. Further levels of automation, notably CNC milling, have since improved the efficiency of Isogrid milling [2.9,2.16,2.19] and it is currently effective for low-volume, bespoke components as required for aerospace applications. Multi axis CNC milling has developed to the extent AGS structures can be machined into the faces of objects with complex curvature (Figure 2.3) [2.9]. The mechanical performance of milled Isogrid can also be configured by engineers during the design stage, as parameters such as rib height to skin thickness are not limited by the process. Despite these benefits, Isogrid milling is largely inappropriate for large production volumes due to high production times, material waste and post-processing requirements [2.2,2.22].

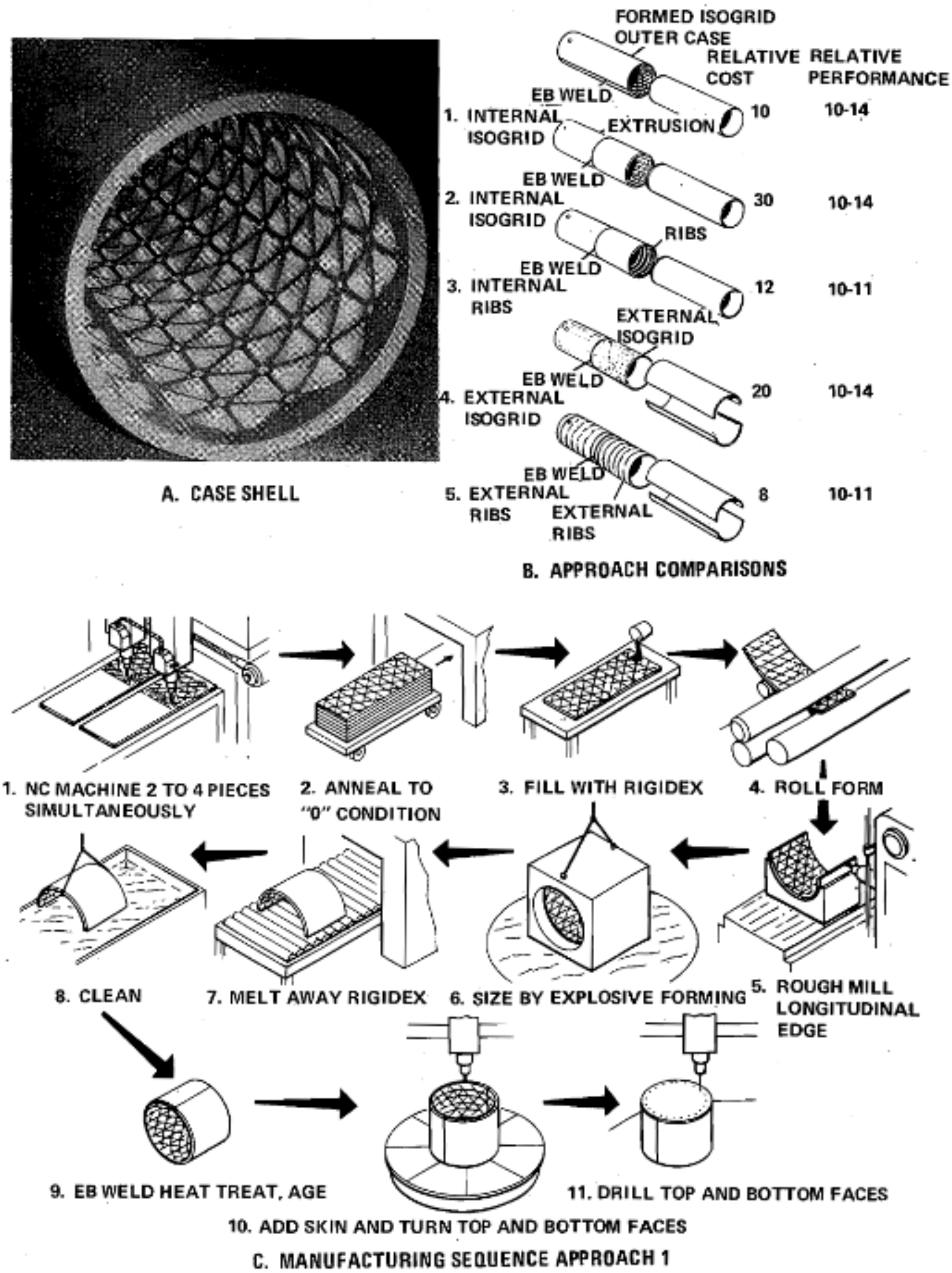

Figure 2.2 Example of Isogrid manufacturing process [2.19]

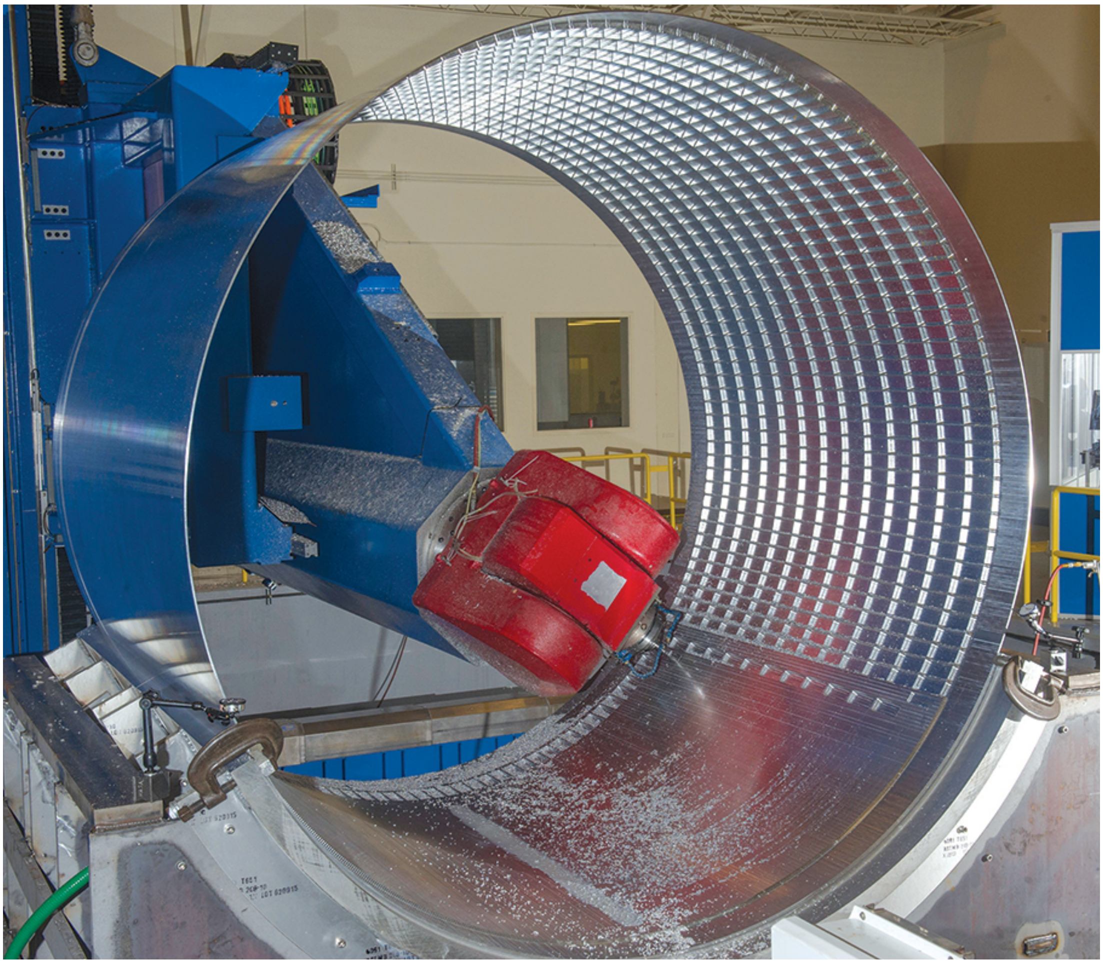

Figure 2.3 Integrally stiffened structure milling on a non-flat surface with multi-axis mill [2.9].

2.3 Chemical and abrasive milling

Slysh et al. [2.2,2.22] proposed chemical milling as a potential manufacturing method for Isogrid. This technique employs a corrosive etchant to chemically dissolve stock material with which it comes into contact [2.24]. Material is selectively removed by employing a masking layer to protect the rib lattice from the material removal process. This method is effective for thin structures; however, its slow rate of milling (13-33µm/min) and safety concerns surrounding chemical handling are key disadvantages. Taller Isogrid structures require longer exposure to the etchant to remove sufficient depth from the stock material; however, long milling times increase the incidence of defects such as undercut, and deeper cuts suffer poor surface finishes [2.24]. The etchant needs to be renewed after saturation with the base material [2.24], limiting the mass of material which can be milled away efficiently. This restricts chemical milling to a small batch process, and it is therefore not suitable for industrial production [2.25,2.26]. The efficiency of Isogrid is a function of the relative height of the rib lattice [2.17], putting chemically milled structures at a performance disadvantage.

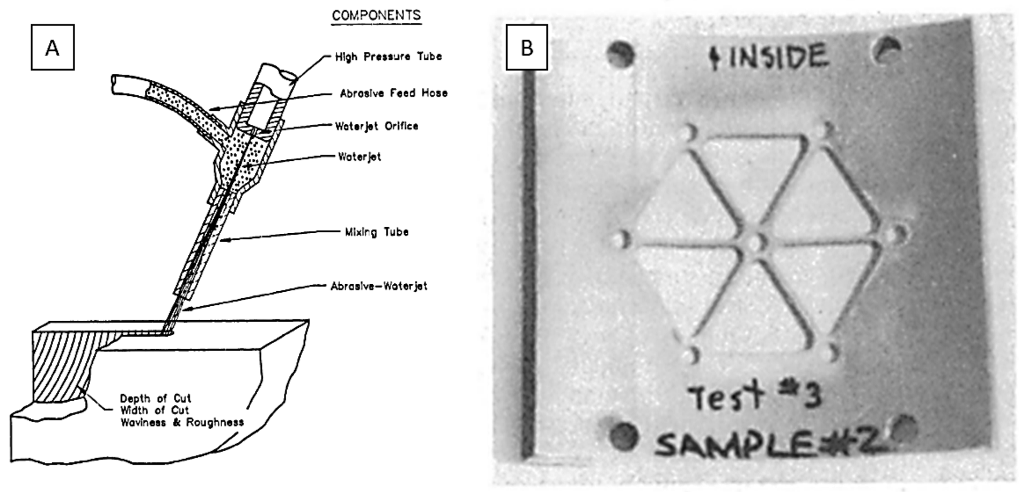

Figure 2.4 A- Abrasive waterjet milling process[2.27] B- Sample section of abrasive waterjet milled Isogrid [2.28]

A waterjet milling method was proposed by Hashish et al. [2.27] in which a high-pressure jet of water carrying abrasive media performs material removal (Figure 2.4-A). Like chemical milling, a steel mask covers areas of the billet which are not to be removed, leaving a rib lattice in the case of Isogrid (Figure 2.4-B). The waterjet milling method can remove material more rapidly than chemical milling; however, the time taken was still relatively high at 4.5 hours for an Isogrid structure made from 1220mmx305mm of aluminium plate [2.27]. Waterjet milling is capable of removing deeper pockets than chemical milling to create a greater range of efficient geometries; however, the steel masks erode rapidly and require replacement regularly [2.27].

2.4 Near net shape forming

Near-net shape forming (NNSF) is a process which aims to reduce machining time, cost and waste material by forming a geometric approximation of the final part, then post processing with a combination of additive and subtractive manufacturing methods to achieve the desired geometry [2.29–2.32]. NNSF was reviewed as a promising technique for the production of Isogrid and other AGS structures [2.29,2.32]. Ivanco et al. [2.32] states that a cost saving of 50% could be made by employing near net shape production methods, and that this was largely attributable to a reduction in labour required for machining, welding, and inspection.

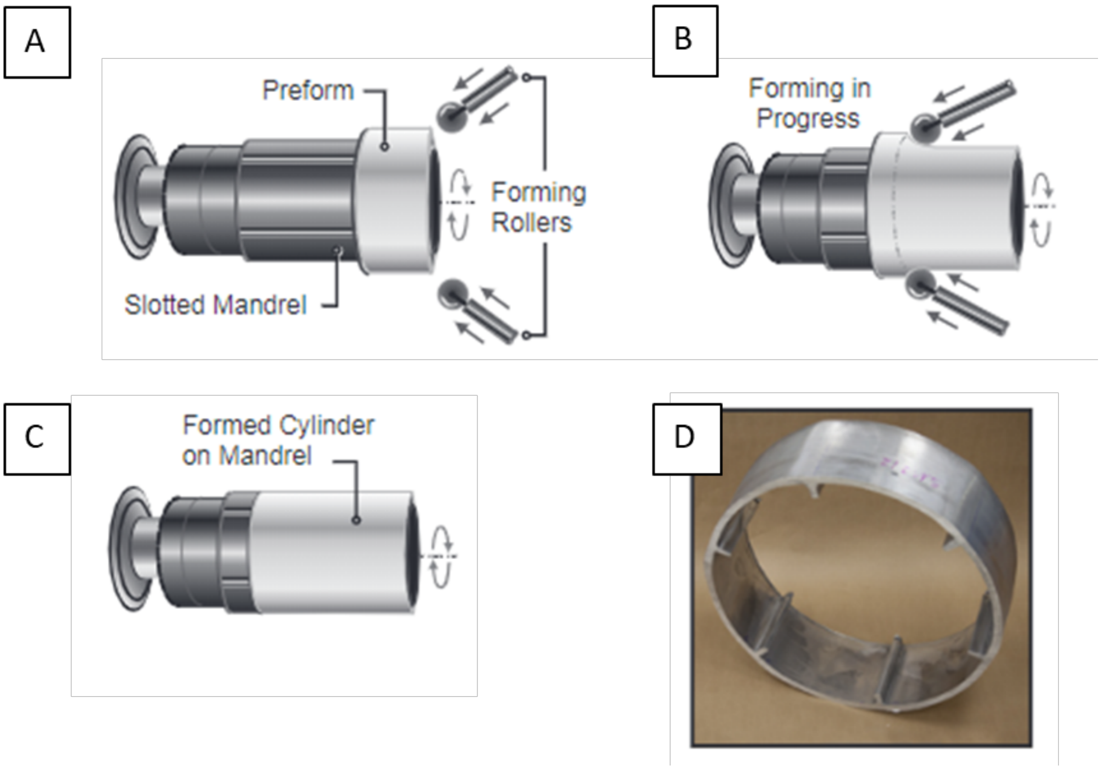

Figure 2.5 A – C, Near net shape forming process of a longitudinally stiffened cylinder on a slotted mandrel, D- Cross section of resultant longitudinally stiffened cylinder [2.33]

Wagner et al. [2.34] proposed a related forming method which details how integrally stiffened cylinders can be formed on a slotted mandrel via a process called spin forming [2.29,2.32,2.34]. This method yields cylinders with one direction of reinforcing ribs (Figure 2.5) which provide excellent compressive performance and reduce the welding and joining required for use as the structural component of rockets [2.35]. Ivanco et al. [2.32] considered spin forming in a cost-benefit study as a method for producing integrally stiffened cylinders and found it to represent a significant reduction in cost compared to conventional metallic production methods. Further studies [2.29,2.34,2.35] developed this method to produce a structure with one orientation of stiffening ribs to which other ribs could be welded in post-processing to create an Isogrid AGS cylinder. A recent article has explored spin forming for the production of AGS structures with two orientations of helical ribs [2.36]. Initial trials of flow forming helical AGS structures produced good results in line with predictions from finite element simulation of the process; however, further refinement is required to reduce minor geometric defects present in the formed stiffeners [2.36].

Ivanco et al. [2.29,2.32] concluded that a weight and cost saving was associated with spin forming as an NNSF method when compared to conventional (CNC) methods of producing aluminium Isogrid. The NNSF method discussed by Wagner et al. was also found to be 35-58% cheaper than an equivalent composite structure [2.32]. However, forming methods are limited in their output geometries [2.37], and highly efficient rib to skin ratios may require intensive post-processing.

2.5 Incremental forming

Incremental forming is a manufacturing method in which a sheet metal part is formed in incremental steps using progressive dies or a single point tool [2.38]. Incremental forming has successfully produced grid stiffened sheet geometries [2.39–2.43], and is effective for the testing and development of stiffened components because the single point incremental forming (SPIF) method does not require unique tooling for each component. Incremental forming is capable of generating larger deformations in plate structures than stamping due to shear deformation mechanisms which has been shown to increase the forming limits of aluminium [2.44]. Further development of incremental forming for AGS structures has potential for the production of specific grid-stiffened components; however, the output cannot be classified as an integrally stiffened structure since the stiffening ribs are hollow. As such, incrementally formed Isogrid structures would not exhibit damage resistance or quasi-isotropy as expected [2.17].

2.6 Additive manufacturing

The development of additive manufacturing (AM) has facilitated a series of research articles on topological optimisation of lattice structures such as Isogrid, because the creation of complex geometries has become affordable for low production volumes [2.45–2.52]. These studies use numerical tools like finite element analysis to explore the mechanical properties and behaviours of lattice materials, 3D infill lattices, metamaterials and auxetic structures; then, the results are validated experimentally using 3D printed samples. The polymer-based 3D printing techniques seen throughout these studies are a more mature technology than the additive manufacturing of metals; however, recent reviews suggest that AM metallic lattice structures are becoming more common [2.53,2.54]. Figure 2.6 shows a nozzle which has been additively manufactured using directed energy deposition sintering, which sinters metal powder together in layers to form a component [2.55]. Wire Arc Additive Manufacturing (WAAM) also deposits sequential layers of material to build up components using well established arc welding technologies [2.56,2.57]. Isogrid structures have been successfully manufactured by Shi et al. [2.58] using WAAM. AM can produce complex and optimised structures such as Isogrid without the high material loss or extensive post processing seen throughout the subtractive manufacturing methods discussed so far [2.59]. However, there are serious disadvantages to the use of metallic additive manufacturing. The production time required for AM components is high, and the equipment and consumable materials (such as feedstock powder and shielding gases) are expensive [2.59,2.60]. Further disadvantages can also be seen in the properties of the resultant AM structure, such as poor surface quality [2.60], high risk of porosity and microcracking [2.61], and scatter in the mechanical properties of the produced structure [2.62]. As such, the use of AM for high-volume production of Isogrid structures is unlikely.

Figure 2.6 Additively manufactured Isogrid nozzle [2.63]

2.7 Fibre reinforced composite methods

Both Huybrechts et al. [2.1,2.3–2.5,2.64] and Vasiliev et al. [2.14] agreed that fibre reinforced composites were more promising materials for the ongoing development of grid stiffened structures. Fibre reinforced composites are anisotropically strong in the fibre direction. As such, an increase in lattice efficiency can be achieved by aligning the fibres of a composite material with the rib directions of an Isogrid structure [2.4,2.65–2.68]. This strengthening mechanism is unavailable to lattices composed of metals, and a subsequent preference for composite Isogrid structures within Aerospace applications has become apparent in the literature [2.4,2.26,2.66,2.67,2.69–2.76].

Composite Isogrid structures have been shown to exhibit damage tolerance [2.77]; however, free edge effects increase interlaminar stresses significantly and create a risk of delamination, ply failure and matrix cracking which serve as initiation sites for further damage to the structure [2.78]. Bellini et al. [2.79] compared identical structures made from a carbon fibre reinforced polymer (CFRP) and Titanium Ti6Al4V. The CFRP Isogrid cylinder provided an almost identical stiffness to the titanium alloy while weighing 66% less.

The manufacturing methods for composite structures are generally expensive, involving manual steps and large specialised equipment. Composite Isogrid structures are primarily produced by either layup methods, in which the fibres are placed manually into moulds [2.77,2.80], or by filament winding, in which fibres are wound onto a mould using a robotic arm and a spool [2.13,2.66,2.72,2.75,2.79,2.81–2.83]. The automated filament winding methods have been found to produce better mechanical properties and higher quality finishes than hand layup samples [2.72,2.75]. However, thermally expanding mould blocks have been developed within layup methods which deliver improved rib density and mechanical properties [2.3,2.5,2.84]. The methods for producing composite Isogrid structures are effective and well established for the production of highly optimised structures, but the cost of materials, manufacturing time and batch processing methods they employ are best suited to application specific production [2.1,2.14,2.84].

2.8 Summary of manufacturing methods

Isogrid has proven to be a reliable and effective lightweight structure, which explains its persistent usage throughout the aerospace industry despite its high cost of production [2.85–2.89]. This cost stems from various process parameters associated with the permutations of machining, forming, joining, and additive manufacturing discussed in this chapter which are used to produce Isogrid [2.2,2.22,2.58,2.90]. The available manufacturing methods for Isogrid structures have been developed over time to minimise these issues, automating manual processes and optimising material usage; however, a fully continuous process for high volume production of Isogrid has not been developed.

Composite Isogrid structures have superior mechanical properties, and are likely to continue as the focus of performance driven research in stiffened structural materials for aerospace applications. CNC milled Isogrid is a proven, effective structure for the space industry, which has already developed the infrastructure to support the production volumes of Isogrid it requires. Additive manufacturing is likely to play a central role in the development of novel frontiers for lightweight topologies and stiffened components. However, none of these methods are suitable for high-volume production. This gap exists because the intended application for each method discussed in this chapter has required very high performance for a limited number of components. In other words, Isogrid structures have always been constructed for a specific purpose, and never produced generally to be used as a stock material for unspecified applications.

This body of work aims to prove the concept of Isogrid rolling to address the mass-producibility gap in Isogrid manufacturing. As discussed in chapter 1, rolling is an established, scalable method of production, which is already utilised to produce the sheet metal products and structural sections which are used ubiquitously throughout industry. By combining these concepts, the beneficial aspects of grid stiffened structures may be applied to existing stock products such as sheet metal for use throughout wider industry.

2.9 List of References

[2.1] Huybrechts SM, Hahn SE, Meink TE. Grid Stiffened Structures: A Survey of Fabrication Analysis and Design Methods. International Conference on Composite Materials 1999.

[2.2] Slysh P. Picking the best high-strength, lightweight structures. Machine Design 1990;62:85–9.

[2.3] Huybrechts SM, Meink TE, Wegner PM, Ganley JM. Manufacturing theory for advanced grid stiffened structures. Compos Part A Appl Sci Manuf 2002. https://doi.org/10.1016/S1359-835X(01)00113-0.

[2.4] Huybrechts S, Tsai SW. Analysis and behavior of grid structures. Compos Sci Technol 1996;56:1001–15. https://doi.org/10.1016/0266-3538(96)00063-2.

[2.5] Huybrechts S, Meink TE. Advanced grid stiffened structures for the next generation of launch vehicles. IEEE Aerospace Applications Conference Proceedings, vol. 1, 1997, p. 263–9. https://doi.org/10.1109/aero.1997.574417.

[2.6] Pettit RG, Wang JJ, Toh C, Metschan S. Validated Feasibility Study of Integrally Stiffened Metallic Fuselage Panels for Reducing Manufacturing Costs Cost Assessment of Manufacturing / Design Concepts. Technical Report: NASA/CR-2000-209342 2000.

[2.7] Kapania RK, Mulani SB, Tamijani A, Sunny M, Joshi P. EBF3PanelOpt: A computational design environment for panels fabricated by additive manufacturing. 51st AIAA Aerospace Sciences Meeting Including the New Horizons Forum and Aerospace Exposition 2013 2013:1–15. https://doi.org/10.2514/6.2013-212.

[2.8] Hoffman EK, Boddorff AK, Taminger KM, Mulvaney C, Stegall DE. Advanced Lightweight Metallic Fuselage Project Manufacturing Trade Study. n.d.

[2.9] Tayon WA, Rudd MT, Domack MS, Hilburger MW. Development of Advanced Manufacturing Approaches for Single-Piece Launch Vehicle Structures 2022.

[2.10] Totaro G. Flexural, torsional, and axial global stiffness properties of anisogrid lattice conical shells in composite material. Compos Struct 2016;153:738–45. https://doi.org/10.1016/j.compstruct.2016.06.072.

[2.11] Totaro G. Optimal design concepts for flat isogrid and anisogrid lattice panels longitudinally compressed. Compos Struct 2015. https://doi.org/10.1016/j.compstruct.2015.03.067.

[2.12] Totaro G. Local buckling modelling of isogrid and anisogrid lattice cylindrical shells with hexagonal cells. Compos Struct 2013. https://doi.org/10.1016/j.compstruct.2012.07.011.

[2.13] Totaro G, de Nicola F. Recent advance on design and manufacturing of composite anisogrid structures for space launchers. Acta Astronaut 2012;81:570–7. https://doi.org/10.1016/j.actaastro.2012.07.012.

[2.14] Vasiliev V v., Barynin VA, Rasin AF. Anisogrid lattice structures - Survey of development and application. Compos Struct 2001. https://doi.org/10.1016/S0263-8223(01)00111-8.

[2.15] Vasiliev V v., Razin AF. Anisogrid composite lattice structures for spacecraft and aircraft applications. Compos Struct 2006;76:182–9. https://doi.org/10.1016/j.compstruct.2006.06.025.

[2.16] Schultz LE. The Computer Aided Design/Drafting (CADD) System: Applications & Economic Factors in the Design/Manufacturing process n.d.:204–8.

[2.17] Meyer RR, Harwood OP, Harmon MB, Orlando JI. Isogrid design handbook. NASA 1973.

[2.18] Blakey-Milner B, Gradl P, Snedden G, Brooks M, Pitot J, Lopez E, et al. Metal additive manufacturing in aerospace: A review. Mater Des 2021;209. https://doi.org/10.1016/j.matdes.2021.110008.

[2.19] Slysh P. Isogrid Structures Technology and Applications. San Diego: Society for Allied Weight Engineers; n.d.

[2.20] Slysh P. Isogrid Structural Applications. Conference of the Society of Allied Weight Engineers 1976:27.

[2.21] Slysh P, Dyer JE, Furman JH, Key JE. Isogrid Structures. AIAA/ASME/SAE 16th Structures, Structural Dynamics, and Materials Conference 1975. https://doi.org/10.2514/6.1975-816.

[2.22] Slysh P, Ringwald RS, Dyer JE, Browing DL. 1063. Isogrid Weight Optimum Structures. 34th Annual Conference, Seattle, Washington, May 5-7 1975.

[2.23] Lam ACL, Shi Z, Yang H, Wan L, Davies CM, Lin J, et al. Creep-age forming AA2219 plates with different stiffener designs and pre-form age conditions: Experimental and finite element studies. J Mater Process Technol 2015;219:155–63. https://doi.org/10.1016/j.jmatprotec.2014.12.012.

[2.24] Dini JW. Chemical milling. International Metallurgical Reviews 1975;20:29–56. https://doi.org/10.1179/imtlr.1975.20.1.29.

[2.25] Kim TD. Fabrication and testing of composite isogrid stiffened cylinder. Compos Struct 1999;45:1–6. https://doi.org/10.1016/S0263-8223(98)00124-X.

[2.26] Kim TD. Fabrication and testing of thin composite isogrid stiffened panel. Compos Struct 2000. https://doi.org/10.1016/S0263-8223(99)00122-1.

[2.27] Hashish M, Marvin M, Monserud D. Abrasive-Waterjet Machining Of Isogrid Structures. 1990.

[2.28] Hashish M. Controlled-depth milling of isogrid structures with AWJs. Journal of Manufacturing Science and Engineering, Transactions of the ASME 1998. https://doi.org/10.1115/1.2830106.

[2.29] Tayon W, Domack M, Wagner J, Taminger K, Hoffman E, Newman S. Development and Characterization of the Integrally Stiffened Cylinder (ISC) Process for Launch Vehicles and Aircraft Fuselage Structures. Minerals, Metals and Materials Series, vol. 6, 2021. https://doi.org/10.1007/978-3-030-65396-5_46.

[2.30] Kudo H. TOWARDS NET-SHAPE FORMING. J Mater Process Technol 1990:307–42.

[2.31] Dean TA. The net-shape forming of gears. Mater Des 2000;21:271278.

[2.32] Ivanco ML, Domack MS, Stoner MC, Hehir AR. Cost-benefit analysis for the advanced near net shape technology (ANNST) method for fabricating stiffened cylinders. AIAA Space and Astronautics Forum and Exposition, SPACE 2016 2016:1–19. https://doi.org/10.2514/6.2016-5488.

[2.33] NASA. Innovative Manufacturing of Launch Vehicle Structures-Integrally Stiffened Cylinder Process. n.d.

[2.34] Wagner J, Domack M, Tayon W, Bird RK. Innovative Manufacturing of Launch Vehicle Structures - Integrally Stiffened Cylinder Process. Nasa 2017:2016–7.

[2.35] Tayon WA, Domack MS, Wagner JA. Characterization of 10-ft. Diameter Aluminum Alloy 2219 Integrally Stiffened Cylinders. n.d.

[2.36] Lyu W, Zhan M, Gao P, Ma F, Li R, Zhang H, et al. Rib filling behavior in flow forming of thin-walled tube with helical grid-stiffened ribs. International Journal of Advanced Manufacturing Technology 2022;119:2877–94. https://doi.org/10.1007/s00170-021-08613-y.

[2.37] Sabroff AM, Boulger FW, Henning HJ, Spretnak JW. A manual on Fundamentals of forging practice. 1964.

[2.38] Emmens WC, Sebastiani G, van den Boogaard AH. The technology of Incremental Sheet Forming-A brief review of the history. J Mater Process Technol 2010;210:981–97. https://doi.org/10.1016/j.jmatprotec.2010.02.014.

[2.39] Kubit A, Wydrzynski D, Bucior M, Krasowski B. Testing of stiffening ribs formed by incremental forming in thin-walled aircraft structures made of 2024-T3 ALCLAD aluminium alloy. AIP Conf Proc 2018;1960. https://doi.org/10.1063/1.5035041.

[2.40] Slota J, Kubit A, Trzepieciński T, Krasowski B, Varga J. Ultimate load-carrying ability of rib-stiffened 2024-t3 and 7075-t6 aluminium alloy panels under axial compression. Materials 2021;14:1–19. https://doi.org/10.3390/ma14051176.

[2.41] Trzepieciński T, Kubit A, Dzierwa A, Krasowski B, Jurczak W. Surface finish analysis in single point incremental sheet forming of rib-stiffened 2024-T3 and 7075-T6 alclad aluminium alloy panels. Materials 2021;14. https://doi.org/10.3390/ma14071640.

[2.42] Kubit A, Trzepiecinski T, Święch Ł, Faes K, Slota J. Experimental and numerical investigations of thin-walled stringer-stiffened panels welded with RFSSW technology under uniaxial compression. Materials 2019;12. https://doi.org/10.3390/ma12111785.

[2.43] Kubit A, Korzeniowski M, Bobusia M, Ochałek K, Slota J. Analysis of the Possibility of Forming Stiffening Ribs in Litecor Metal-Plastic Composite Using the Single Point Incremental Forming Method. Key Eng Mater 2022;926:802–14. https://doi.org/10.4028/p-i92gl3.

[2.44] Allwood JM, Shouler DR. Generalised forming limit diagrams showing increased forming limits with non-planar stress states. Int J Plast 2009;25:1207–30. https://doi.org/10.1016/j.ijplas.2008.11.001.

[2.45] Harvey PS, Virgin LN. Effect of stiffener geometry on the response of grid-stiffened panels. J Eng Mech 2018;144:1–7. https://doi.org/10.1061/(ASCE)EM.1943-7889.0001415.

[2.46] Porter JH, Cain TM, Fox SL, Harvey PS. Influence of infill properties on flexural rigidity of 3D-printed structural members. Virtual Phys Prototyp 2019;14:148–59. https://doi.org/10.1080/17452759.2018.1537064.

[2.47] Fan HL, Jin FN, Fang DN. Mechanical properties of hierarchical cellular materials. Part I: Analysis. Compos Sci Technol 2008. https://doi.org/10.1016/j.compscitech.2008.09.022.

[2.48] Forcellese A, di Pompeo V, Simoncini M, Vita A. Manufacturing of isogrid composite structures by 3D printing. Procedia Manuf 2020;47:1096–100. https://doi.org/10.1016/j.promfg.2020.04.123.

[2.49] Shroff S, Acar E, Kassapoglou C. Design, analysis, fabrication, and testing of composite grid-stiffened panels for aircraft structures. Thin-Walled Structures 2017;119:235–46. https://doi.org/10.1016/j.tws.2017.06.006.

[2.50] Li T, Chen Y, Hu X, Li Y, Wang L. Exploiting negative Poisson's ratio to design 3D-printed composites with enhanced mechanical properties. Mater Des 2018. https://doi.org/10.1016/j.matdes.2018.01.034.

[2.51] Kalman J, Fayazbakhsh K, Martin D. Automated draping analysis of 3D printed flexible isogrid structures for textile applications. Textile Research Journal 2021;91:2387–400. https://doi.org/10.1177/00405175211006210.

[2.52] Nguyen L, Buhl J, Bambach M. Continuous Eulerian tool path strategies for wire-arc additive manufacturing of rib-web structures with machine-learning-based adaptive void filling. Addit Manuf 2020;35:101265. https://doi.org/10.1016/j.addma.2020.101265.

[2.53] DebRoy T, Wei HL, Zuback JS, Mukherjee T, Elmer JW, Milewski JO, et al. Additive manufacturing of metallic components – Process, structure and properties. Prog Mater Sci 2018;92:112–224. https://doi.org/10.1016/j.pmatsci.2017.10.001.

[2.54] Chen LY, Liang SX, Liu Y, Zhang LC. Additive manufacturing of metallic lattice structures: Unconstrained design, accurate fabrication, fascinated performances, and challenges. Materials Science and Engineering R: Reports 2021;146:100648. https://doi.org/10.1016/j.mser.2021.100648.

[2.55] Ahn DG. Directed Energy Deposition (DED) Process: State of the Art. International Journal of Precision Engineering and Manufacturing - Green Technology 2021;8:703–42. https://doi.org/10.1007/s40684-020-00302-7.

[2.56] Derekar KS. A review of wire arc additive manufacturing and advances in wire arc additive manufacturing of aluminium. Materials Science and Technology (United Kingdom) 2018;34:895–916. https://doi.org/10.1080/02670836.2018.1455012.

[2.57] Cunningham CR, Flynn JM, Shokrani A, Dhokia V, Newman ST. Invited review article: Strategies and processes for high quality wire arc additive manufacturing. Addit Manuf 2018;22:672–86. https://doi.org/10.1016/j.addma.2018.06.020.

[2.58] Shi J, Li F, Chen S, Zhao Y. T-GMAW based novel Multi-node trajectory planning for fabricating grid stiffened panels: An efficient production technology. J Clean Prod 2019;238:117919. https://doi.org/10.1016/j.jclepro.2019.117919.

[2.59] Gardan J. Additive manufacturing technologies State of the art and trends. Additive Manufacturing Handbook, 2017.

[2.60] Chen LY, Liang SX, Liu Y, Zhang LC. Additive manufacturing of metallic lattice structures: Unconstrained design, accurate fabrication, fascinated performances, and challenges. Materials Science and Engineering R: Reports 2021;146:100648. https://doi.org/10.1016/j.mser.2021.100648.

[2.61] Mandache C. Overview of non-destructive evaluation techniques for metal-based additive manufacturing. Materials Science and Technology (United Kingdom) 2019;35:1007–15. https://doi.org/10.1080/02670836.2019.1596370.

[2.62] Roy S, Shassere B, Yoder J, Nycz A, Noakes M, Narayanan BK, et al. Mitigating scatter in mechanical properties in AISI 410 fabricated via arc-based additive manufacturing process. Materials 2020;13:1–24. https://doi.org/10.3390/ma13214855.

[2.63] BeAM Machines. Isogrid Rocket Nozzle manufactured using directed energy deposition. Https://WwwBeam-MachinesCom/Case-Studies/Adding-Features-Isogrid n.d.

[2.64] Wegner PM, Ganley JM, Huybrechts SM, Meink TE. Advanced grid stiffened composite payload shroud for the OSP launch vehicle. IEEE Aerospace Conference Proceedings 2000;4:359–65. https://doi.org/10.1109/aero.2000.878447.

[2.65] Tsai SW. Theory of Composites Design. 1992.

[2.66] TSAI SW, LIU KS, MANNE PM. Manufacture and design of composite grids. 3-D Textile Reinforcements in Composite Materials, Elsevier; 1999, p. 151–79. https://doi.org/10.1533/9781845691929.151.

[2.67] Tsai SW. Manufacture and design of composite grids. Technical Report 1997;1997:59–71. https://doi.org/10.3989/mc.1997.v47.i247-248.495.

[2.68] Chen HJ, Tsai SW. Analysis and optimum design of composite grid structures. J Compos Mater 1996;30:503–34. https://doi.org/10.1177/002199839603000405.

[2.69] Kim TD. Postbuckled behavior of composite isogrid stiffened shell structure. Advanced Composite Materials 2000;9:253–63. https://doi.org/10.1163/15685510051033467.

[2.70] Li M, Sun F, Lai C, Fan H, Ji B, Zhang X, et al. Fabrication and testing of composite hierarchical Isogrid stiffened cylinder. Compos Sci Technol 2018. https://doi.org/10.1016/j.compscitech.2018.01.040.

[2.71] Li M, Fan H. Multi-failure analysis of composite Isogrid stiffened cylinders. Compos Part A Appl Sci Manuf 2018;107:248–59. https://doi.org/10.1016/j.compositesa.2018.01.010.

[2.72] Sorrentino L, Marchetti M, Bellini C, Delfini A, Albano M. Design and manufacturing of an isogrid structure in composite material: Numerical and experimental results. Compos Struct 2016. https://doi.org/10.1016/j.compstruct.2016.02.043.

[2.73] Kanou H, Nabavi SM, Jam JE. Numerical modeling of stresses and buckling loads of isogrid lattice composite structure cylinders. International Journal of Engineering, Science and Technology 2018;5:42. https://doi.org/10.4314/ijest.v5i1.4.

[2.74] Rahimi GH, Zandi M, Rasouli SF. Analysis of the effect of stiffener profile on buckling strength in composite isogrid stiffened shell under axial loading. Aerosp Sci Technol 2013;24:198–203. https://doi.org/10.1016/j.ast.2011.11.007.

[2.75] Sorrentino L, Marchetti M, Bellini C, Delfini A, Del Sette F. Manufacture of high performance isogrid structure by Robotic Filament Winding. Compos Struct 2017. https://doi.org/10.1016/j.compstruct.2016.12.061.

[2.76] Hao M, Hu Y, Wang B, Liu S. Mechanical behavior of natural fiber-based isogrid lattice cylinder. Compos Struct 2017. https://doi.org/10.1016/j.compstruct.2017.05.028.

[2.77] Reddy AD, Valisetty RR, Rehfield LW. Continuous filament wound composite concepts for aircraft fuselage structures. J Aircr 1985;22:249–55. https://doi.org/10.2514/3.45115.

[2.78] Skrna-Jakl I, Rammerstorfer FG. Numerical investigations of free edge effects in integrally stiffened layered composite panels. Compos Struct 1993;25:129–37. https://doi.org/10.1016/0263-8223(93)90159-N.

[2.79] Bellini C, Di Cocco V, Iacoviello F, Sorrentino L. Performance index of isogrid structures: robotic filament winding carbon fiber reinforced polymer vs. titanium alloy. Materials and Manufacturing Processes 2021;00:1–9. https://doi.org/10.1080/10426914.2021.1926489.

[2.80] Bellini C, Sorrentino L. Characterization of isogrid structure in GFRP. Frattura Ed Integrita Strutturale 2018;12:319–31. https://doi.org/10.3221/IGF-ESIS.46.29.

[2.81] Totaro G, Spena P, Giusto G, de Nicola F, Kiryenko S, Das S. Highly efficient CFRP anisogrid lattice structures for central tubes of medium-class satellites: Design, manufacturing, and performance. Compos Struct 2021;258:113368. https://doi.org/10.1016/j.compstruct.2020.113368.

[2.82] Chen L, Fan H, Sun F, Zhao L, Fang D. Improved manufacturing method and mechanical performances of carbon fiber reinforced lattice-core sandwich cylinder. Thin-Walled Structures 2013. https://doi.org/10.1016/j.tws.2013.03.002.

[2.83] Giusto G, Totaro G, Spena P, De Nicola F, Di Caprio F, Zallo A, et al. Composite grid structure technology for space applications. Mater Today Proc 2019;34:332–40. https://doi.org/10.1016/j.matpr.2020.05.754.

[2.84] Huybrechts S, Meink TE, Underwood RL. Method for making advanced grid stiffened structures. US Patent: 6245274, 2001.

[2.85] Papathakis K V. Design and Development of Nano-electro Fuel Batteries and Rim-driven Motors for Electrified Aircraft Applications. 2021.

[2.86] Oleson S, Schmitz PC, Runyon K, Bussey B, Ostdiek P, Colozza AJ, et al. Dynamic Radioisotope Power System (DRPS) Permanently Shadowed Region (PSR) Demonstrator Rover 2021.

[2.87] Oleson S, Fittje J, Schmitz P, Tian L, Klefman B, Korn S, et al. Power System Design Trades for a Pressurized Lunar / Mars Rover 2019.

[2.88] Knighton D. Delta Launch Vehicle Isogrid Structure Nastran Analysis. 1972.

[2.89] Greathouse JP, Hines M V, Jezak KK, Moore RG, Nielsen RM, Ridenoure R. The isosat small satellite a design in isogrid technology n.d.

[2.90] Alexopoulos ND, Gialos AA, Zeimpekis V, Velonaki Z, Kashaev N, Riekehr S, et al. Laser beam welded structures for a regional aircraft: Weight, cost and carbon footprint savings. J Manuf Syst 2016;39:38–52. https://doi.org/10.1016/j.jmsy.2016.02.002.

3 Materials and Methods

3.1 Commercially pure aluminium

Aluminium alloy AA1050 was chosen as the billet material for Isogrid rolling for its low hardness and excellent formability. AA1050 (composition in Table 3.1) is classified as a wrought, or non-heat-treatable alloy, which indicates that it cannot be strengthened via heat treatment or “aging” like some aluminium alloys [3.1]. Such heat treatments rely on alloying elements to form precipitates which improve the mechanical characteristics of heat treatable alloys.

Table 3.1 Elemental composition of AA1050 [3.2,3.3]

Element	% Composition
Aluminium, Al	≥ 99.50 %
Copper, Cu	≤ 00.05 %
Iron, Fe	≤ 00.40 %
Magnesium, Mg	≤ 00.05 %
Manganese, Mn	≤ 00.05 %
Other, each	≤ 00.03 %
Silicon, Si	≤ 00.25 %
Titanium, Ti	≤ 00.03 %
Vanadium, V	≤ 00.05 %
Zinc, Zn	≤ 00.05 %

AA1050 is at least 99.5% pure aluminium and does not contain alloying elements to a degree suitable for aging. Non heat treatable aluminium alloys are instead strengthened via the introduction of cold work, which refines the grain structure of the material, increasing strength and hardness. It is available commercially in various temper states, such as -H18 (rolled to full hardness), -H14 (rolled to half hardness) and -O (annealed), which describe the degree to which it has been cold-worked [3.3,3.4]. The required stress applied to AA1050 for plastic deformation (flow stress) is presented in Figure 3.1 [3.5] as a function of strain.

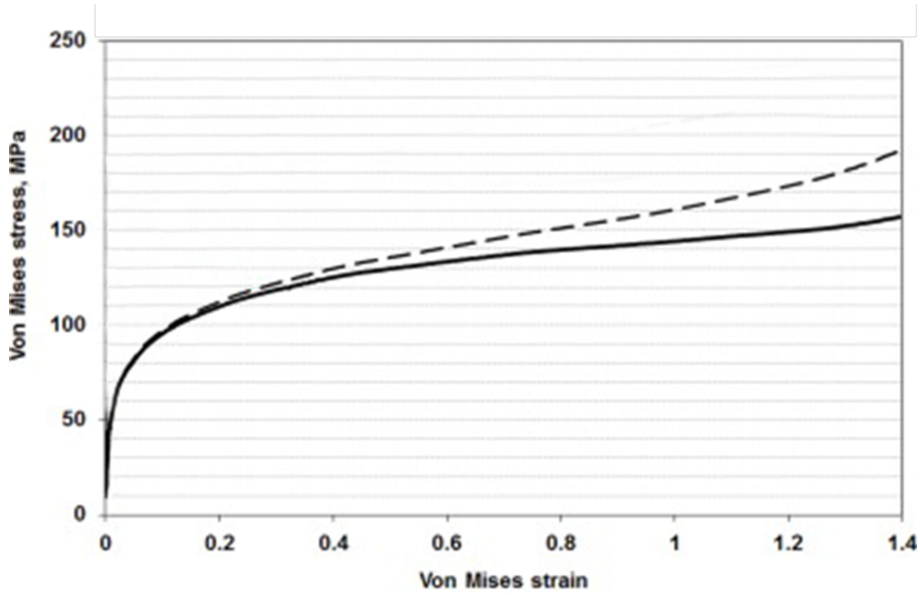

Figure 3.1 Flow stress of AA1050 in the annealed condition (adapted from [3.5])

AA1050 was sourced in the -H14 condition as a billet material for rolling. Its hardness was measured to be 41Hv, and after annealing at 535°C for a duration of 1 hour to the -O condition, the hardness was measured at 20Hv.

3.2 Methods of sample production – Rolling

Rolled Isogrid samples were manufactured in a customised Durston D158 rolling mill. The design and implementation of this process, and target Isogrid geometry are covered in Chapter 4.

3.3 Methods of sample production - CNC Isogrid milling

Isogrid samples were machined in a HAAS VF6 CNC mill to provide a control group of traditionally produced Isogrid for comparison. The rib geometry of the CNC milled Isogrid was chosen to be identical to the rolled Isogrid to provide a fair comparison. Plates of 3mm AA1050-H14 were clamped into the HAAS VF6 CNC mill and the Isogrid geometry was machined using a combination of: pocket milling operations with endmill bits, and profile milling with 30° V bits. Figure 3.2 shows a side-by-side comparison of the Isogrid manufactured by rolling and CNC milling.

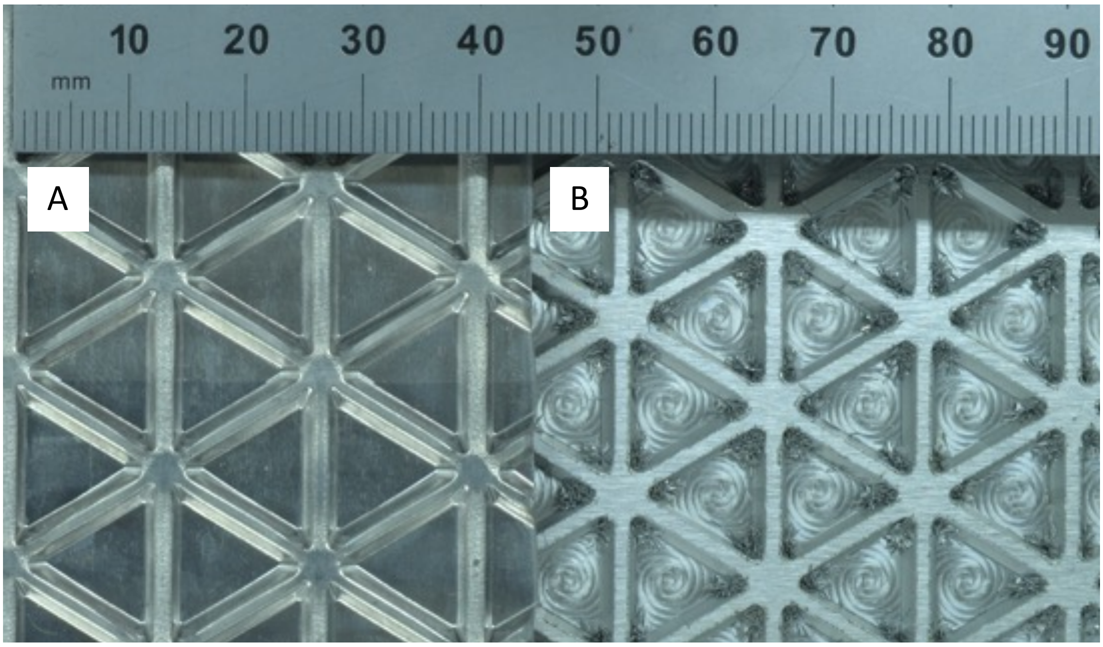

Figure 3.2 Produced Isogrid samples: A- Rolled, B- CNC milled

3.3.1 Specimen creation - CNC waterjet cutting

A waterjet abrasive cutting machine was used to produce billets for rolling and generate specimen geometries from the produced sheets of Isogrid for tensile, bending and fatigue tests. The waterjet cutter fires abrasive particles at the workpiece via an accurate high-pressure jet of water and is operated via computer control on an XY gantry, which allows the nozzle to follow a toolpath generated in a CAD package. This cutting method has a kerf of 3mm, which is effectively the width of the cut. The Isogrid plates were held in place on rigid compressed wooden boards using double sided tape. This abrasive cutting method does not deform the material surrounding the cut, thereby avoiding the introduction of cold work into the specimen hence alteration of its microstructural and mechanical properties.

3.3.2 Sample sectioning

Samples for metallographic preparation and analysis were sectioned using an abrasive cutting wheel enclosed in an ATA Brillant 230 metallographic cut off saw machine. Abrasive cutting in this manner imparts minimal strain into the surface of the cut samples which can then be ground away in the following preparation stages. The cutting assembly and sample are continuously cooled with a cutting fluid while in operation to prevent thermal build-up in the sample which may alter its properties. The samples were clamped in place using the built-in vice.

3.4 Metallographic methods and microstructural characterisation

3.4.1 Sample mounting

After sectioning, samples were mounted in cylindrical plastic mounts to facilitate grinding, polishing and further metallographic analysis methods. Hot mounting methods encased the samples in Bakelite mounts (Figure 3.3-A). Hot mounting presses heat the sample and Bakelite powder to 200°C for 15 minutes, while applying constant pressure to compact and set the thermoplastic. Cold metallographic mounting method used 2-part Epofix Epoxy which was mixed and cast into a mould with the sectioned specimen to encase the sample and allowed to set (Figure 3.3-B).

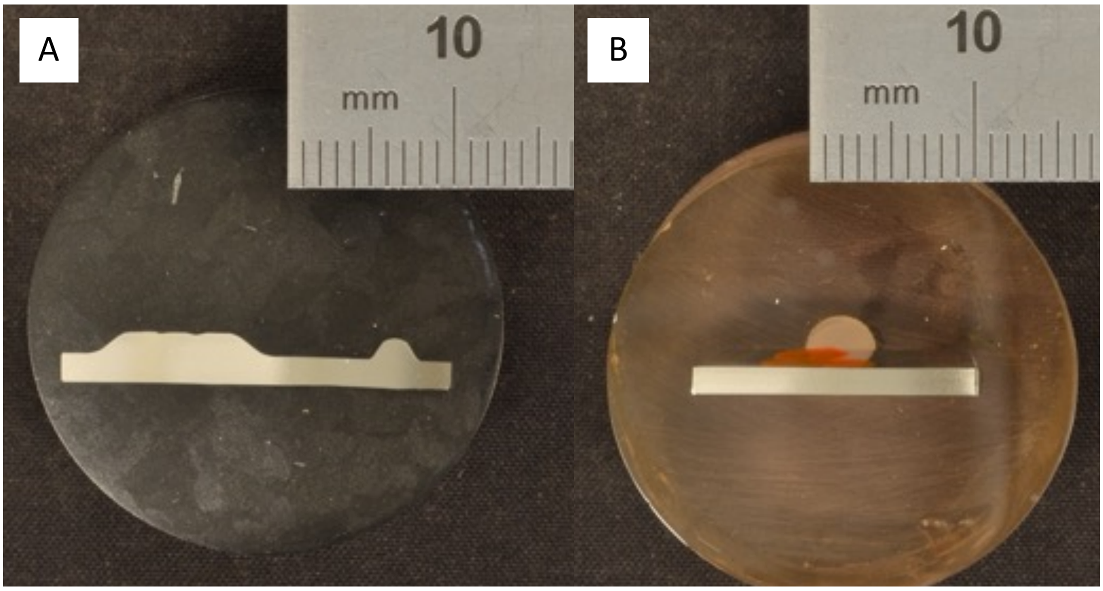

Figure 3.3 Samples mounted in: A-30mm Bakelite mount; B-30mm Epoxy mount

3.4.2 Sample polishing

Samples were ground and polished to remove surface strains from cutting processes and achieve an appropriate surface quality for further analyses. This was performed using a

Struers Rotoforce metallographic rotary grinding and polishing machine (Figure 3.4-A). All grinding operations started with a 500 grit Silicon Carbide abrasive paper, under wet grinding conditions for 2 minutes. Contrary rotation was chosen to remove material more effectively at 300rpm with 100N of force applied to a sample holder containing 3 samples. The same conditions were then repeated for 800, 1200, and 2000 grit papers.

The polishing stages were completed with diamond suspensions of 6µm and 3µm on polishing pads, then finished with an oxide polishing suspension (OPS) of colloidal silica which is equivalent to 0.05µm grit on a neoprene polishing wheel. Polishing times were 2 minutes per stage, with sympathetic rotation at 150rpm and an individual force of 30N applied to individual samples. The final stage using OPS is a combined chemical/mechanical polishing process which is effective for removing scratches and providing high quality surface finishes [3.6].

For the even finer surface finishes, the samples were put through an extra polishing stage with the OPS suspension in a vibratory polishing machine. The ATA Saphir Vibro vibratory polishing machine (Figure 3.4-B) induced an 85Hz vibration on its polishing plate covered with a soft cloth and pool of colloidal silica suspension. The vibration caused samples to travel across the cloth surface while submerged in the colloidal silica for combined mechanical/chemical attack. Weights were placed onto the samples according to their surface area and the process was run for a duration of 90 minutes.

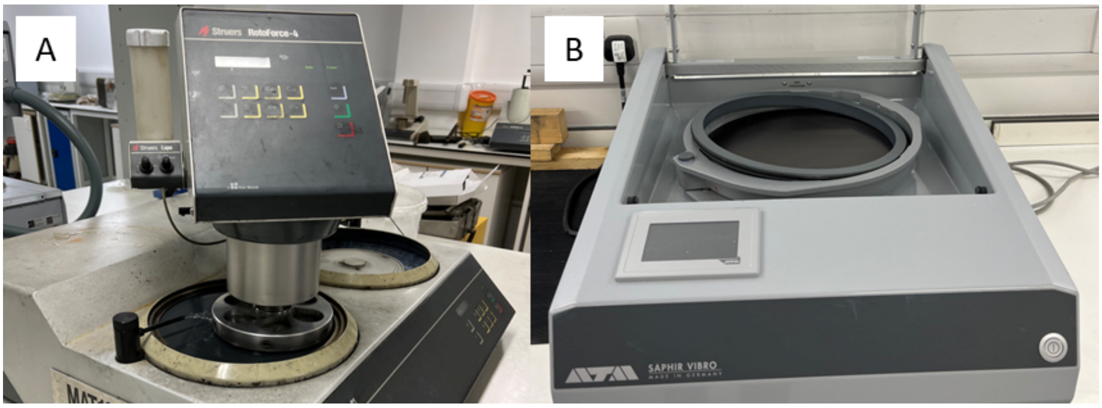

Figure 3.4 A- Struers Rotoforce grinding and polishing machine, B – ATA Saphir Vibro vibration polisher

3.4.3 Sample etching

A Barker's microstructural electrolytic etch was used to reveal grain structure in the AA1050 samples [3.6]. Samples for etching were sectioned (section 4.1.1) and mounted in epoxy (section 4.3.3). A hole was bored into the back of each mount up to the sample and a copper electrode probe inserted to make electrical contact with the back of the sample. This sample assembly was placed in a glass beaker containing Barker's reagent as seen in Figure 3.5. The 2.5% Barker's reagent was mixed from 4.5ml of Fluoroboric acid (HBF) with 200ml of deionised water. The sample to be etched was connected to the power supply as the anode of the electrolytic circuit which was set to 20V DC for 150 seconds, then the sample was removed and thoroughly rinsed. A stirring rod was used to agitate the volume of reagent and reduce incidence of bubble artefacts on the surface of the etched samples (Figure 3.6).

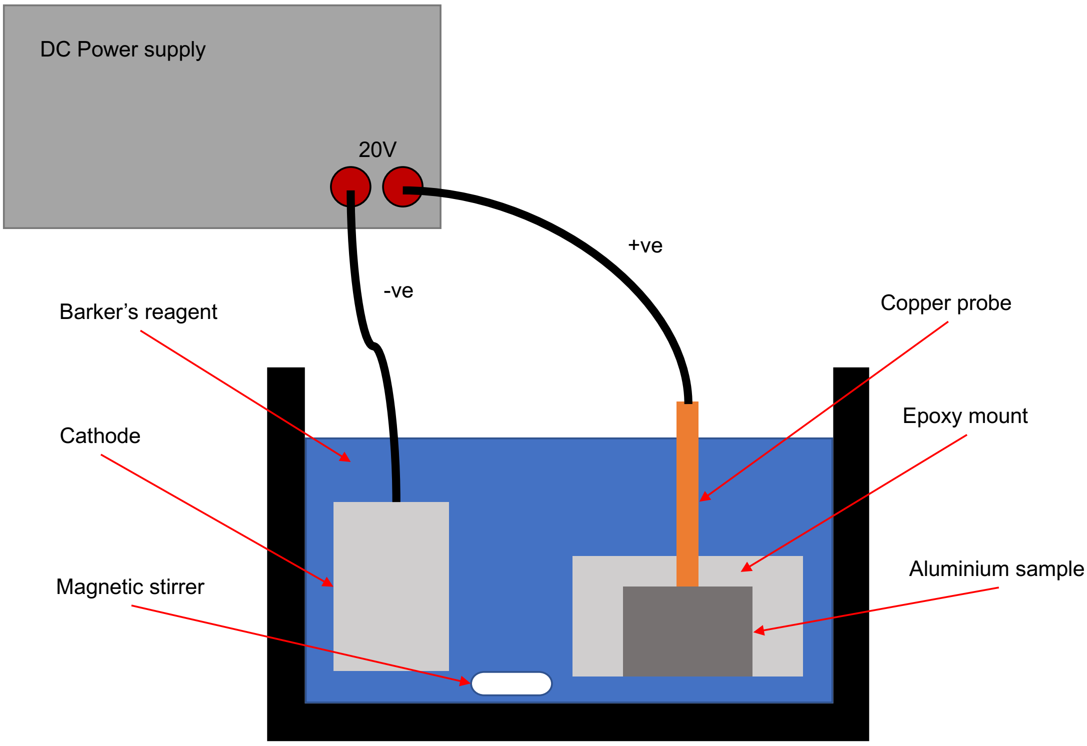

Figure 3.5 Diagram of the electrolytic etching process

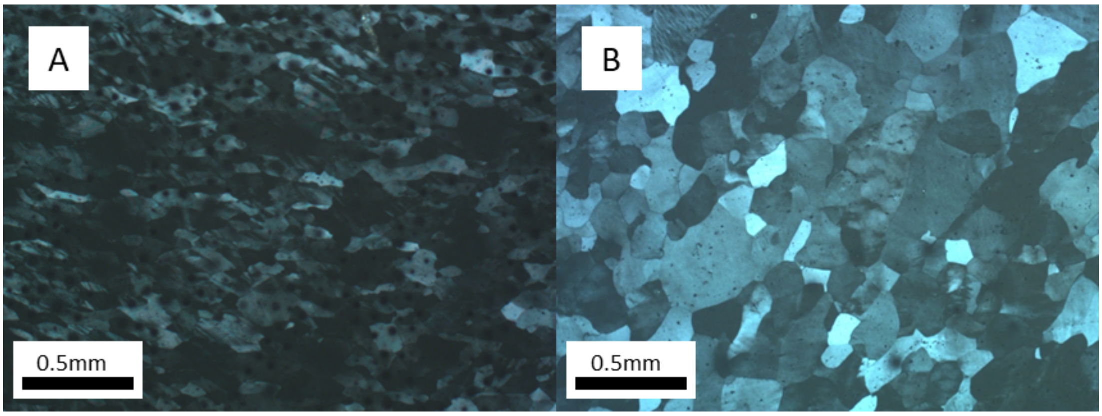

Figure 3.6 Etched micrographs of AA1050 showing A- etching without agitation and B- Etching with agitation

3.4.4 Hardness measurement

Vickers hardness was measured by applying a load to a pyramid shaped indentation tool over a set period of time then measuring the resultant indent. Macrohardness was measured using a Vickers hardness tester (Figure 3.7-A), applying a load of 500g for a dwell time of 10 seconds. Microhardness was measured on mounted and polished samples with a Qatia Qness automated microhardness tester (Figure 3.7-B), with a load of 100g for a dwell time of 10 seconds.

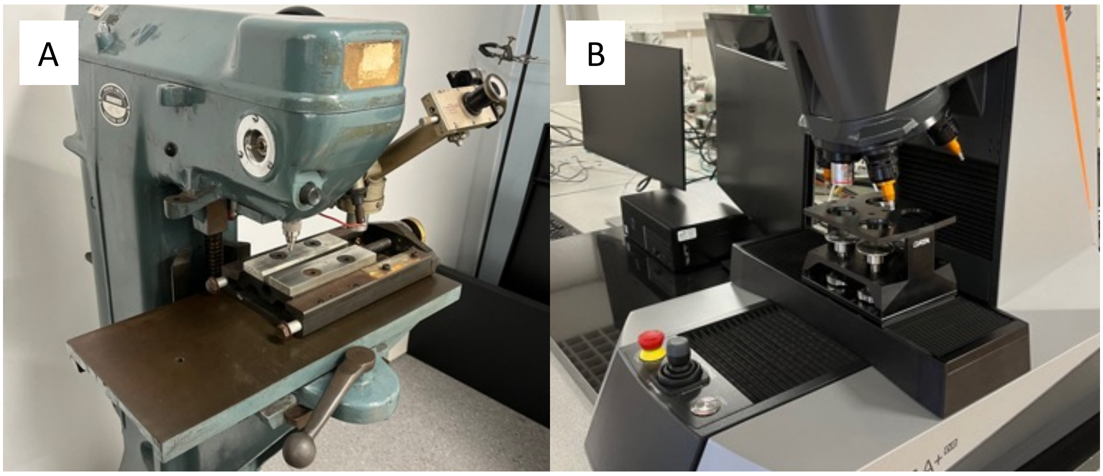

Figure 3.7 A- Vickers Hardness tester and B- Qatia Qness automated microhardness tester

3.4.5 Optical Microscopy

Etched samples were inspected on an Olympus GX-51 inverted metallographic microscope (Figure 3.8) under polarised light crossed to extinction to reveal the grain structure of the samples [3.6].

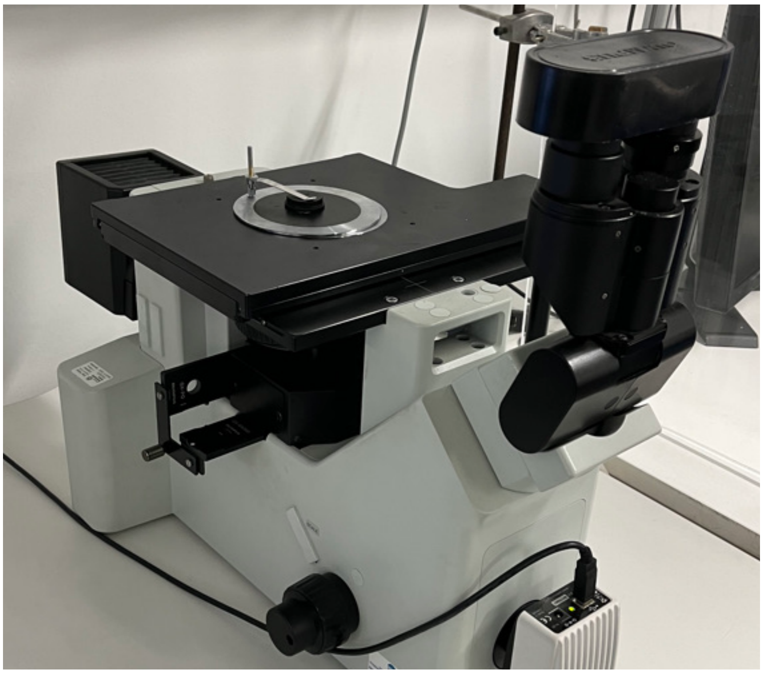

Figure 3.8 Olympus GX-51 inverted metallographic microscope

Images were taken at magnifications of x50, x100, x200 and x500. Stitched images were created for features which were larger than the available imaging space on the lowest magnification. The stage was manually manoeuvrable in X and Y via positioning knobs, and movements between images for stitching included a ~10% overlap to allow image processing software (Adobe Photoshop) to stitch the micrographs.

3.4.6 SEM microscopy

Fractography and investigations of surface quality (Figure 3.10-A) were performed using a Hitachi S3700-N scanning electron microscope (SEM) (Figure 3.10-A), which performed high magnification imaging of the sample surface using a focused beam of electrons. Samples were mounted onto a 2” sample holder using conductive adhesive tape to make an electrical connection to the stage and prevent build-up of static charge which impedes focusing. The SEM was set to an accelerating voltage of 15kV, and the working distance varied between

10-20mm due to the non-planar nature of the specimens. Images of fracture surfaces from mechanical testing were taken at x200, x500 and x1000 magnification to allow identification of smaller features and their location in the context of the larger fracture surface.

3.4.7 EBSD analysis

Electron backscatter diffraction (EBSD) is a method of analysing the crystal structure of metals. Electrons are accelerated at a point on an inclined sample surface in a field emission scanning electron microscope (FE-SEM). The underlying lattice reflects electrons which strike a phosphor screen creating a backscatter Kikuchi pattern (BKP) (Figure 3.9). A camera captures the image of the BKP which corresponds to an orientation of the underlying crystal structure. A large matrix of points is sampled which allows the creation of grain orientation maps and related statistical data. The morphology of a specimen's grain structure can be inferred from the maps of grain orientation created using EBSD, and the microstructural texture can be determined by plotting distributions of grain orientation on diagrams known as pole figures and orientation distribution functions (ODF).

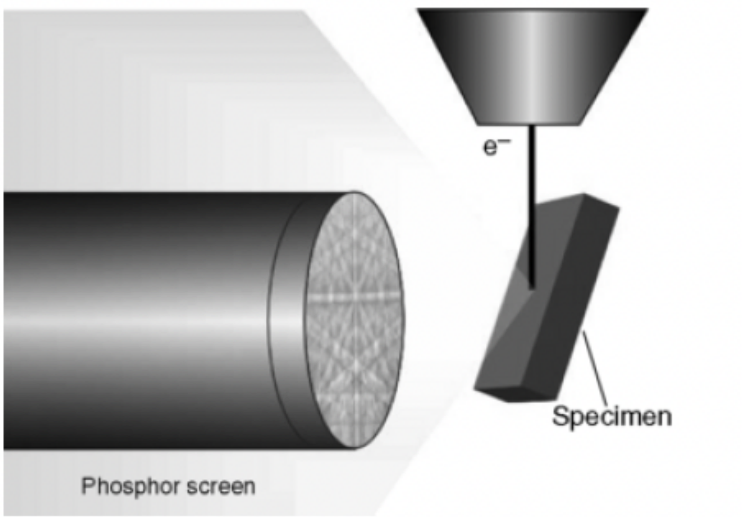

Figure 3.9 Diagram of EBSD technique [3.6]

Samples for EBSD analysis were mounted in epoxy, ground, polished and vibratory polished to achieve the very high surface quality required for EBSD. The samples were then broken out of these epoxy mounts mechanically and mounted in the Hitachi SU6600 FE-SEM (Figure 3.10-B) at 70° to the detector. The accelerating voltage of the FE-SEM was set to 20kV, and the detector was focused at x50 magnification on the sample surface, at a working distance of 20.5mm. The step size between sampled points was set to 1µm, and each point was exposed to the electron beam for 0.7s. The sensor captured the Kikuchi pattern using a 2x2 binning. EBSD data was processed in AZteC Crystal by Oxford instruments, to plot pole figures, ODFs and measure the size and aspect ratio of grains.

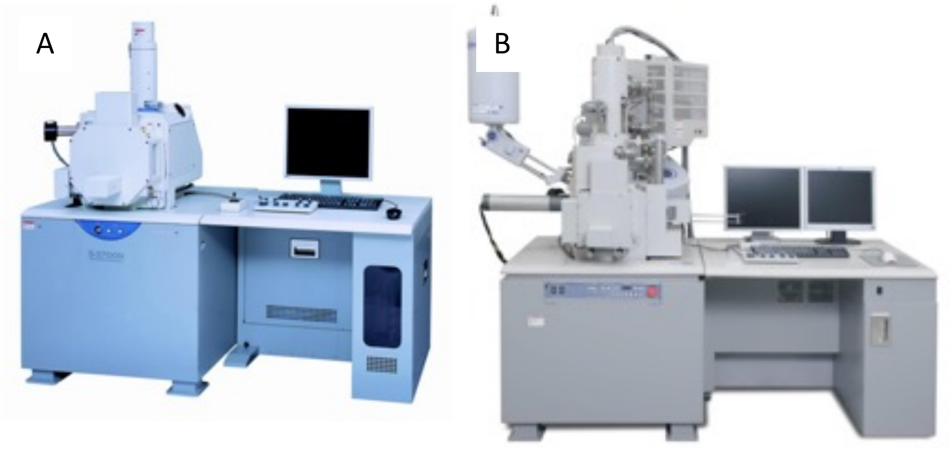

Figure 3.10 Scanning Electron Microscopes: A- Hitachi S3700-N W-SEM, B- Hitachi SU6600 FE-SEM

3.5 Methods of mechanical Testing

3.5.1 Tensile Testing

Tensile testing was conducted to assess the in-plane mechanical performance of rolled and CNC Isogrid, using Instron 100kN and 250kN universal testing machines according to international standards [3.7]. The samples were secured in the grips of the universal testing machine (Figure 3.11) and subjected to uniaxial tension as the grips moved apart at a rate of 1mm/minute, increasing to 5mm/minute after 5 minutes for highly ductile samples.

Tensile specimens were cut from rolled and CNC sheets of Isogrid at both 0° and 90° to the rolling direction. The specimen geometry was limited by the size of rolled Isogrid sheet which could be produced, so a suitable variation of specimen type 3 from annex B was chosen from BS ISO 6892 [3.7]. This sample geometry for flat specimens uses a gauge width of 25mm, with a minimum gauge length of 50mm. The maximum length of sample which could be achieved at 90° to the roll direction after being cut from the sheet was 70mm. Rolled and CNC Isogrid were tested at 0° and 90° in both the annealed and cold worked condition, with 3 samples per permutation of these parameters. The Instron's inbuilt stress calculation functionality was not utilised due to the irregular cross section of the Isogrid specimens, and the data was processed manually to ascertain key results such as yield strength, ultimate tensile strength (UTS) and ductility.

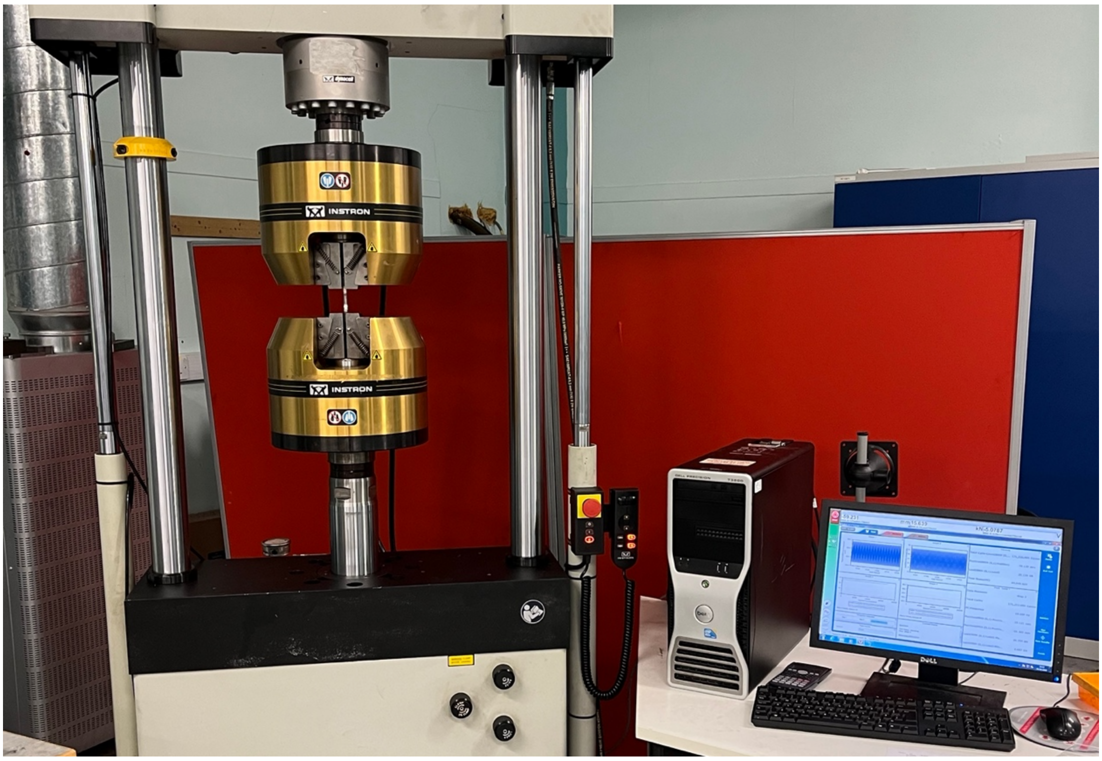

Figure 3.11 Instron 250kN universal mechanical testing machine

The tensile stress for Isogrid samples during testing was calculated using the following equation [3.8]:

$$\sigma = \frac{F}{A} = \frac{F}{b\bar{d}} \tag{3.1}$$

$\bar{d}$ is an equivalent mass thickness defined as:

$$m = V\rho = b\bar{d}L\rho, \qquad \bar{d} = \frac{m}{bL\rho} \qquad (3.2, 3.3)$$

$$\sigma = \frac{F}{b\bar{d}} = \frac{F\cancel{b}L\rho}{\cancel{b}m} = \frac{FL\rho}{m} \tag{3.4}$$

Where: σ is tensile stress (Pa); F is applied load (N); $\bar{d}$ is the equivalent mass thickness as defined in 1.3; b is sample width (m); L is sample length; m is sample mass (kg); and ρ is material density (kg/m³).

3.5.2 Bend Testing

Bend testing was performed to quantify the bending strength of the billet material, rolled Isogrid, and CNC milled Isogrid. Plain strips of AA1050-O, AA1050-H14, and strips of rolled Isogrid in the as rolled state and annealed state were tested to explore this relationship. Samples were sectioned using cooled abrasive disks into strips and finished with sandpaper. Full-U, support and former, three-point bend testing was performed using the Instron universal testing machine (Figure 3.12) as described in international standards [3.9].

For the initial tests comparing rolled Isogrid to flat plate, the strips were cut to the width of two unit cells of the Isogrid pattern (34±1mm). The distance, l, between the formers was set to 18mm as per the standard for samples of this thickness [3.9]. The test was repeated 5 times for each sample group. For subsequent tests comparing rolled Isogrid to CNC Isogrid, the sample geometry was kept consistent with the tensile sample geometry at 25mm x 70mm, with 3 samples per group over the same 8 groups as described for tensile testing.

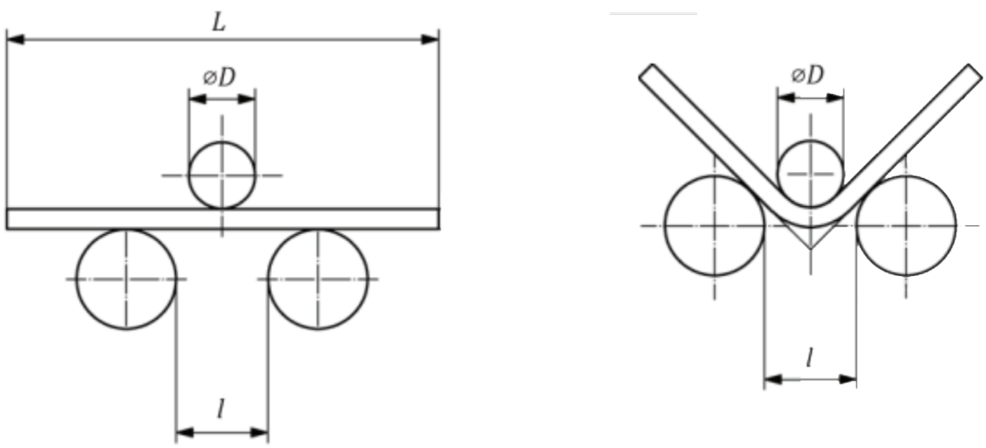

Figure 3.12 Diagram of bend test set up [3.9]

The sample dimensions, *b* (width) and *d* (height) were used to establish the bending stress of each sample from the measured data using the following equation:

$$\frac{M}{I}=\frac{\sigma}{Y}=\frac{E}{R}\Rightarrow\sigma=\frac{MY}{I} \tag{3.5}$$

The bending stress values were then divided by the mass per square meter to compare these values as “specific bending strength”. This accounted for the difference in mass as the Isogrid samples were significantly lighter than the plate samples due to extension in the rolling process. This produced the following relation which was used to find the specific bending strength of the samples from the experimental data:

$$\sigma=\frac{MY}{I}\times\frac{\bar{d}}{\rho} \tag{3.6}$$

Where,

$$M=\frac{F}{2}\times\frac{l}{2},\qquad Y=\frac{d}{2},\qquad I=\frac{bd^3}{12} \tag{3.7, 3.8, 3.9}$$

F is the force measured by the load cell, l is the distance between supports, b and d are the width and thickness of the test samples respectively. As Isogrid does not have a constant thickness, *d*, a conversion factor developed in The Isogrid Design Handbook [3.10] was used to calculate its second moment of area. This expression uses non-dimensional geometric parameters from the rib structure to modify the second moment of area of the Isogrid skin section (equations from [3.10]):

$$I=\frac{bd^3}{12}\times\frac{\beta^2}{1+\alpha} \tag{3.10}$$

Where the following non-dimensional factors are defined as:

$$\alpha=\frac{(average)\,rib\,width\ \times rib\,height}{skin\,thickness\times skin\,height} \tag{3.11}$$

$$\delta=\frac{rib\,height}{skin\,thickness} \tag{3.12}$$

$$\beta = \sqrt{3\alpha(1+\delta)^2 + (1+\alpha)(1+\alpha\delta)^2} \tag{3.13}$$

Using these equations and the standard geometric parameters defined in 3.2, the following values were calculated:

$$\alpha = 0.1255, \qquad \delta = 0.7083, \qquad \beta = 1.515 \tag{3.14}$$

Therefore, the conversion factor in (2.5) was calculated to be:

$$\frac{\beta^2}{1+\alpha} = 2.04 \tag{3.15}$$

3.5.3 Fatigue Testing

Fatigue tests were performed in tension on the Instron 100kN and 250kN universal mechanical testing machines according to international standards [3.11]. The fatigue cycles were carried out between a nominal minimum load of 0N and a specified load at 10Hz, until the specimen failed, or the sample ran out at 3 x 10^6 cycles. This represents a pulsating tension or unidirectional stress testing regime, with an R value of 0.

Fatigue testing is highly sensitive to small defects, cracks, and scratches, as these may form the initiation sites for fatigue mechanisms. As the specimens were manufactured using the waterjet cutter, the affected rough faces were sanded until a high-quality surface finish was achieved to remove any influence from production methods irrelevant to the results. The standards on fatigue testing require the surface roughness of these faces to be less than 0.2Ra [3.11]. To ensure this requirement was met, the surface roughness of relevant fatigue specimen faces was measured using a Mitutoyo Surftest SV-2000 profilometer (Figure 3.13).

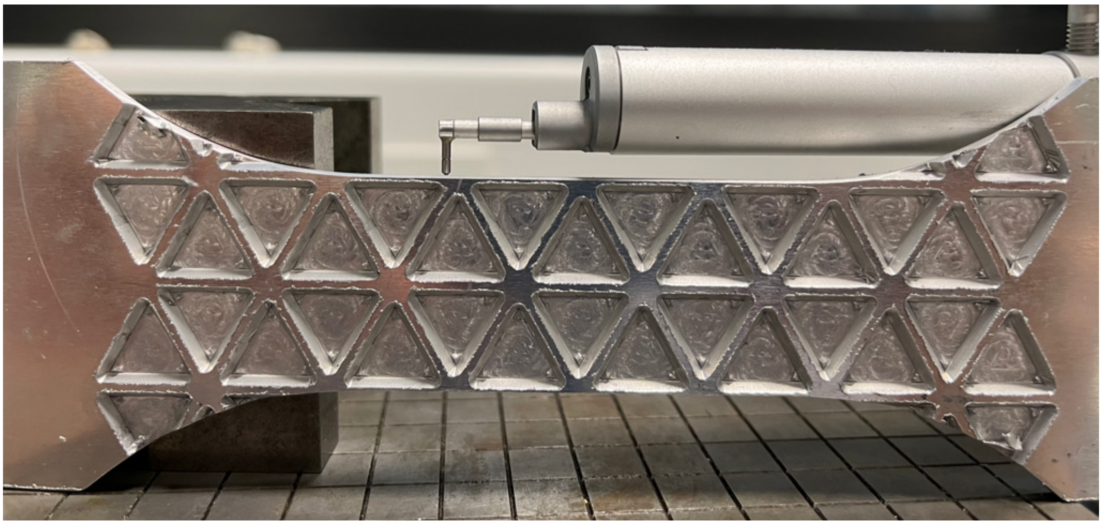

Figure 3.13 Profilometer, Mitutoyo Surftest SV-2000

Fatigue testing is generally performed on specimens with constant cross sections. Isogrid has a non-constant cross section; such thickness variation on the free edge of the specimen may have acted as a stress raiser and initiated fatigue. This was avoided throughout the gauge length by setting the width of the sample in the gauge section to twice the cell height of the Isogrid lattice (13.6mm) and placing the edges of the gauge section along the middle of a rib. Using this gauge width and a thickness of 3mm, the specimen geometry (Figure 3.14) was calculated using the parameters set out in ISO 1099 for a flat specimen [3.11].

The maximum tensile load per sample was calculated as a percentage of yield. These yield values were obtained via a tensile test from each of the sample groups on an identical specimen for calibration. Samples of rolled and CNC Isogrid were fatigue tested at 60%, 70% and 80% of their respective yield stresses. A set of annealed rolled samples were also tested at 70% of yield. Samples of rolled and CNC milled Isogrid were tested in cyclic loading as per the procedure presented in Chapter 3, at 60%, 70% and 80% of their respective yield stress measured using the tensile testing procedure in Section 3.5.1. An S-N plot of this data was generated, and the mean cycle count for each stress range was calculated [3.12,3.13]. A minimum of 5 fatigue samples were tested per group. After 3 consecutive runouts for any given sample group, no further tests were performed.

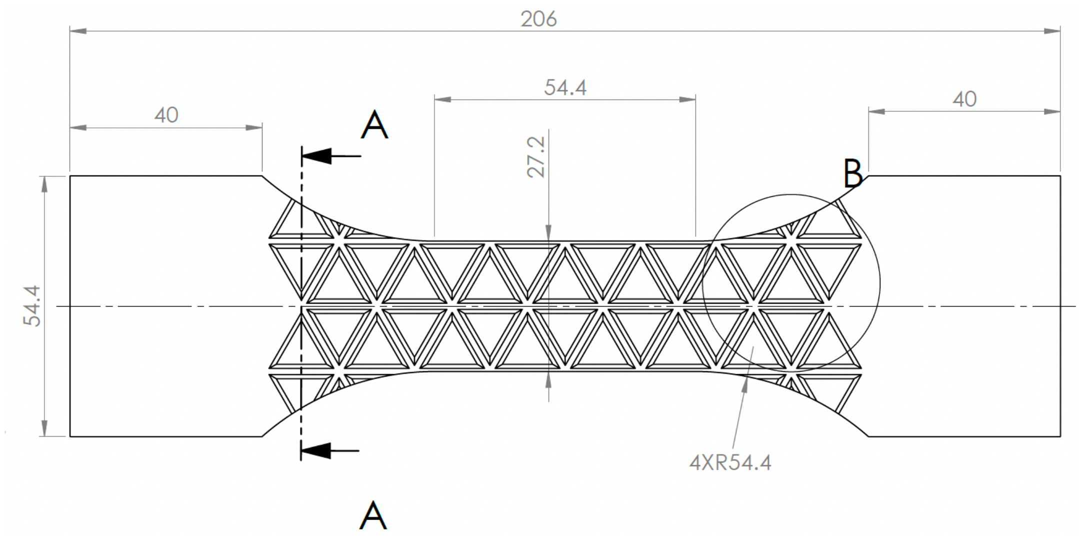

Figure 3.14 Fatigue sample schematic diagram

3.6 Reference List

[3.1] El-Danaf EA. Mechanical properties, microstructure and texture of single pass equal channel angular pressed 1050, 5083, 6082 and 7010 aluminum alloys with different dies. Mater Des 2011;32:3838–53. https://doi.org/10.1016/j.matdes.2011.03.006.

[3.2] The aluminium association. International Alloy Designations and Chemical Composition Limits for Wrought Aluminum and Wrought Aluminum Alloys. The Aluminum Association, Arlington, Virginia 2018;ISSN: 2377:34.

[3.3] ASM Handbook Committee. ASM Handbook Volume 2: Properties and Selection: Nonferrous Alloys and Special-Purpose Materials. ASM International; 1990.

[3.4] Bay N. Cold forming of aluminium-state of the art 2000;71:76–90.

[3.5] Mohebbi MS, Akbarzadeh A, Yoon YO, Kim SK. Flow stress analysis of ultrafine grained AA 1050 by plane strain compression test. Materials Science and Engineering A 2014;593:136–44. https://doi.org/10.1016/j.msea.2013.11.027.

[3.6] Handbook CAI. ASM Metals Handbook, Volume 09 Metallography and Microstrustures Handbook. ASM International 2004;9:2733.

[3.7] British Standards Institute. BS EN ISO 6892-1-2019 - metallic materials - tensile testing n.d.

[3.8] Garrick AJH, Toumpis AI, Galloway AM. Developing a novel manufacturing method to produce stiffened plate structures. International Journal of Advanced Manufacturing Technology 2021:2805–13. https://doi.org/10.1007/s00170-020-06525-x.

[3.9] British Standards Institute. BS EN ISO 7438 - Metallic materials — Bend test 2016.

[3.10] Meyer RR, Harwood OP, Harmon MB, Orlando JI. Isogrid design handbook. NASA 1973.

[3.11] British Standards Institute. BS ISO 1099-2017 - Metallic materials - Fatigue testing - Axial force-controlled method 2017.

[3.12] Murakami Y, Takagi T, Wada K, Matsunaga H. Essential structure of S-N curve: Prediction of fatigue life and fatigue limit of defective materials and nature of scatter. Int J Fatigue 2021;146. https://doi.org/10.1016/j.ijfatigue.2020.106138.

[3.13] Schneider C, Maddox S. Best practice guide on statistical analysis of fatigue data. 2003.

4 Rolling mill design and process development

The Isogrid rolling process, as developed throughout this research, aims to produce Isogrid as described in the Isogrid design handbook [4.1], as a thin skin reinforced by a stiffening network of ribs in 3 directions, each at 60° to one another [4.1–4.4]. As such, the process includes one standard cylindrical roller to maintain a flat face and one modified roller to impart the rib lattice into the opposing surface. Similar processes using geometrically modified rollers in combination with plain rollers have historically been developed to produce sheet metal products with shallow patterns for either aesthetic purposes or functional applications, such as increased surface roughness [4.5,4.6]. Wang et al. [4.7–4.10] found that a modified roller with axially oriented corrugation in combination with a plain roller is effective for the cold roll bonding of dissimilar metals to create laminated structures.

4.1 Process design

To implement the proposed Isogrid rolling technique, a Durston D4 158 rolling mill (Figure 4.2) was modified with a prototype patterned roller containing grooves to imprint the desired Isogrid structure. This was designed by choosing the target Isogrid geometry and subtracting it from the cylindrical face of the roller. Corresponding to the rib lattice of the Isogrid structure, the face of the custom roller contains 3 directions of grooves, each at a constant helix angle of 60° to the others. No such rolling method was found in the technical literature which could guide the design of the groove geometry. Therefore, the assumption was made that the billet would deform into the grooves but may not entirely fill the available volume. The aspect ratio of the patterned roller was considered sufficiently robust such that varying the radius over its length to account for bending due to rolling forces (crowning of the roller) was not necessary. Crowning or similar techniques should be considered to ensure dimensional tolerancing at an industrial scale [4.11]. One groove was aligned with the roll direction (0°) to minimise variation in forces over a revolution of the roller, as seen in Figure 4.2-A. The pattern could be rotated on the cylindrical surface;

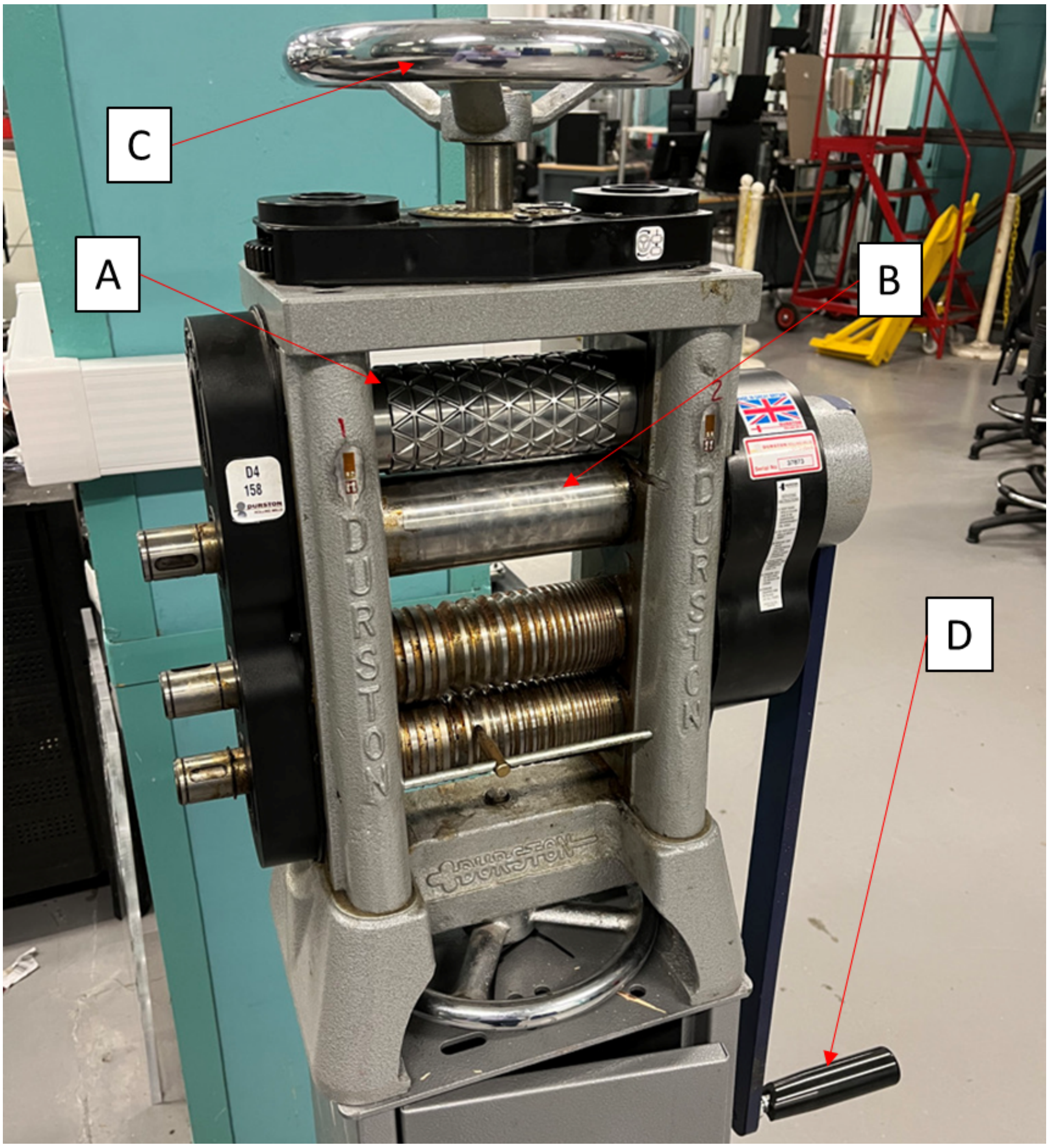

Figure 4.1 Modified Durston rolling mill: A- Isogrid roller, B- Plain roller, C- roll gap adjustment mechanism, D- Crank handle

however, if a groove were to be aligned axially along the roller (perpendicular to the roll direction, Figure 4.2-B), the roller would experience cyclic forces as this groove engaged and disengaged, which would reduce the service life of the equipment. These uneven rolling forces were reported by Li et al. [4.9] during a corrugated roll bonding process. Figure 4.2-C represents a roller where the grooves are unaligned with any significant process direction.

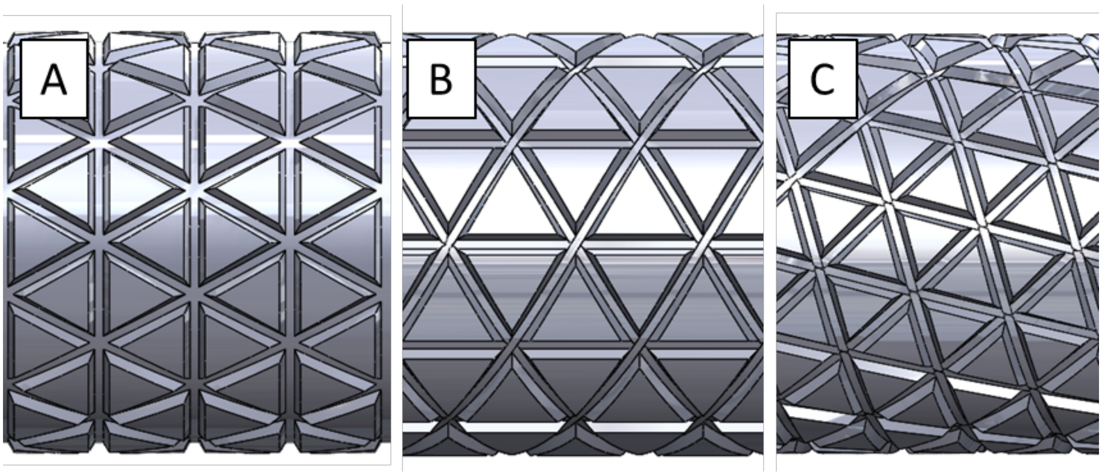

Figure 4.2 Front view of rollers showing A- rib lattice aligned with rib direction, B- rib lattice aligned with axial direction, C- rib lattice oriented at a 15° angle to the rolling direction

The original Durston roller was 60mm in diameter by 158mm long on the roll face. Dimensions *a* and *b*, which define the repeating unit cell of the Isogrid geometry, are linked to the roller radius (Figure 4.3). The grooves over the roller face must be continuous, so that multiple revolutions can be made without introducing discontinuities to the rib lattice. The pattern nodes are located where all three rib directions intersect; an equal spacing of 12 helical grooves around the 60mm diameter roller resulted in a node spacing of *a*=15.7mm, and cell height of *b*=13.6mm (Figure 4.3- B).

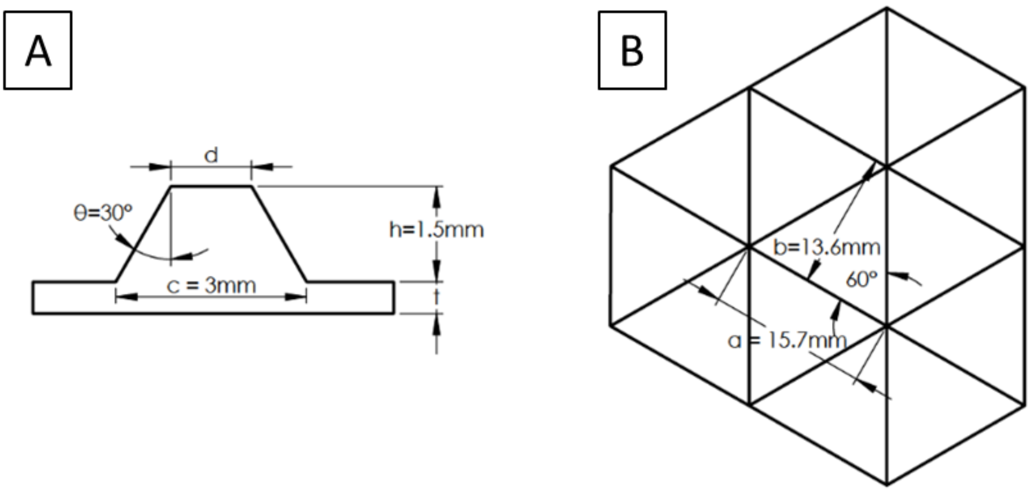

Figure 4.3 a) The target rib profile b) The target rib spacings

A draft angle of 30° was added to the rib profile (Figure 4.3-A) to facilitate the egress of the formed Isogrid from the roller. Each rib must mesh and unmesh with the roller during forming, as though it were part of a rack and pinion gear pair. Rack and pinion gear pairs employ involute gear tooth geometry to ensure that they do not bind [4.12]. An involute curve is approximately linear over the depth of the groove due to its shallow nature with respect to the full radius of the roller. Therefore, 30° was chosen as a linear draft angle to approximate an involute curve for a groove 1.5mm deep on a roller of radius 30mm. This straight-line approximation was tested against potential values of *c* and *h* in SolidWorks and was found to be suitable with no interference as the billet and roller profile moved relative to each other.

Further refinement of the rib profile was conducted by using a volume relation (Equations 4.1-4.3) to define a groove geometry which can accommodate the equivalent mass thickness of a sheet, approximately 0.5mm thick. The cross-sectional area, thus volume of the grooves, was defined by the base width and maximum height of each rib, *c* and *h,* which were set to be 3mm and 1.5mm, respectively, for the target equivalent mass thickness (Figure 4.3-A).

The following equations are derived based on a single equilateral triangular unit cell (Figure 4.4):

$$Volume_{isogrid} = Volume_{skin} + Volume_{ribs} - Volume_{intersection} \tag{4.1}$$

$$V(a,b,c,d,h,t,) = \frac{\sqrt{3}}{4}a^2t + \frac{3}{2}ah\left(\frac{c+d}{2}\right) - 3h\left(\frac{c+d}{2}\right)^2 \times \sin{(60°)} \tag{4.2}$$

$$Equivalent\ mass\ thickness\ (mm) = \bar{d} = \frac{Volume_{isogrid}}{Area_{skin}} = \frac{V(a,b,c,d,h,t,)}{\frac{\sqrt{3}}{4}a^2} \tag{4.3}$$

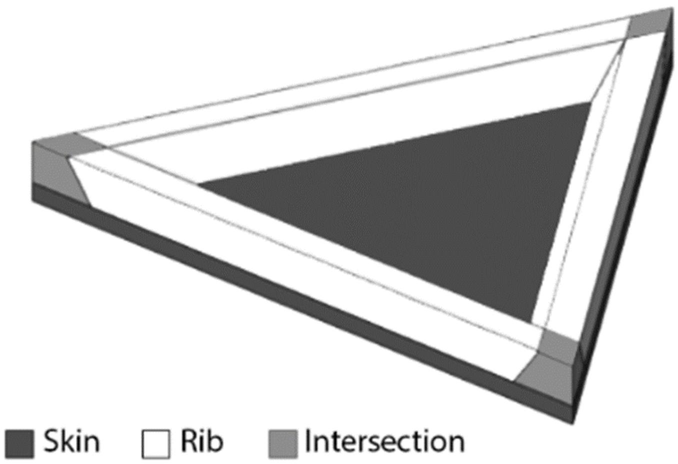

Figure 4.4 Diagram of segments of the unit cell used in calculation of Isogrid volume

The Isogrid roller (Figure 4.5) was designed as seen in Figure 4.6 and manufactured by CNC milling. The roller was then mounted into the Durston mill (Figure 4.2). The material chosen for the roller was high strength AISI4140 steel, which is equivalent to EN19. The roller hardness was measured to be 270Hv in the as produced condition. The roller was left in its machinable state, as hardening may have created warping or embrittled the groove geometry, creating a risk of chipping. Machining marks from the CNC milling process used to manufacture the roller can be seen in Figure 4.7, the effects of which will be discussed in Chapter 7.

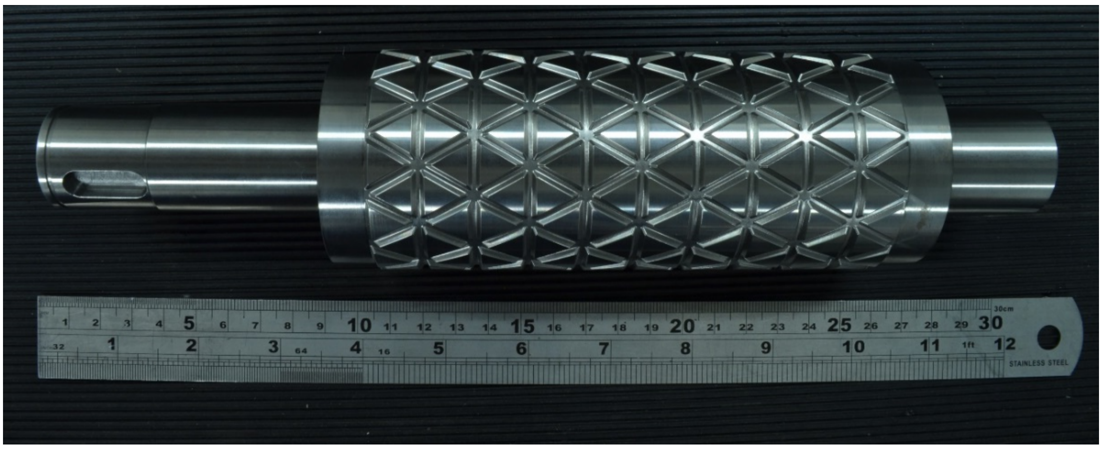

Figure 4.5 The custom Isogrid roller as received

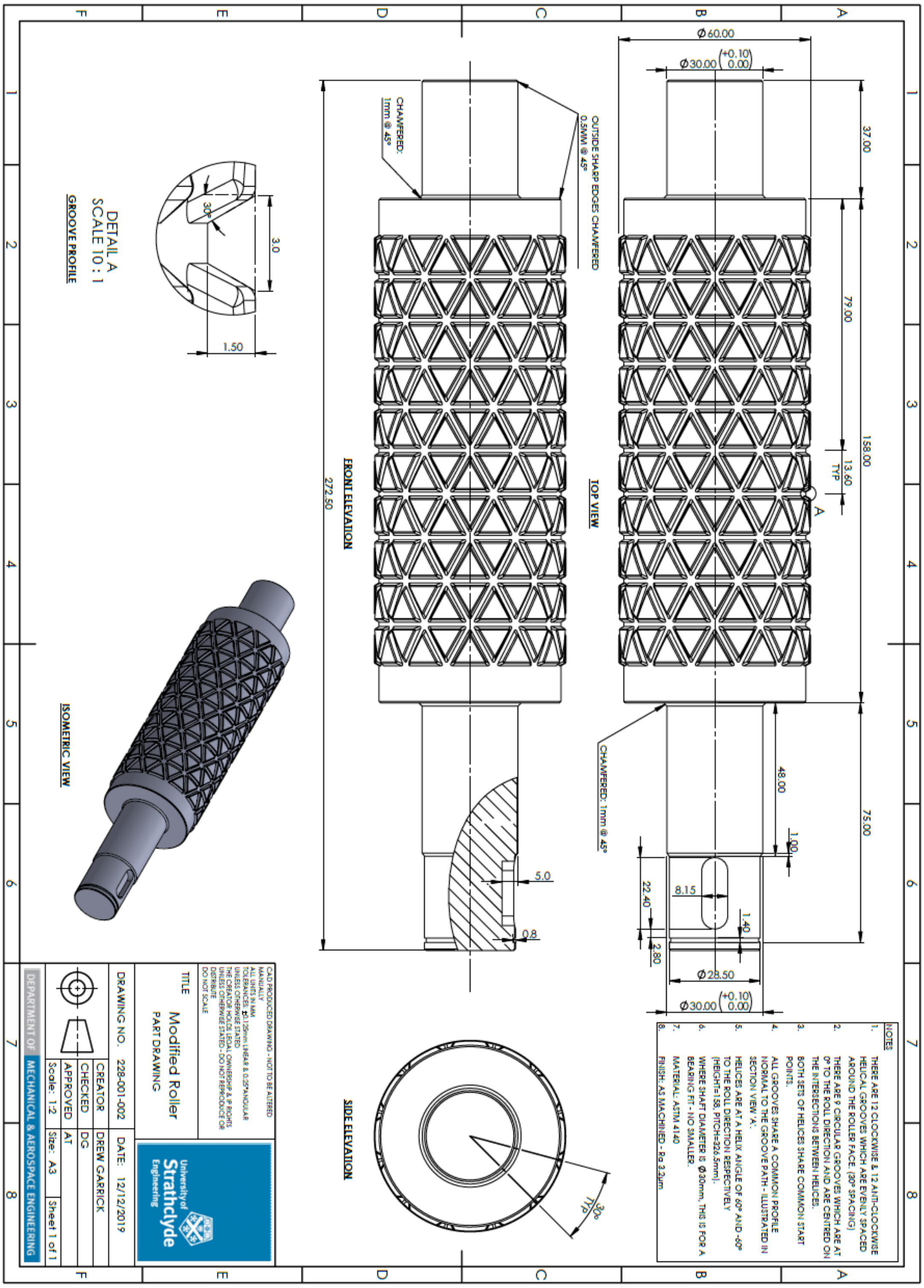

Figure 4.6 Custom roller manufacturing drawing

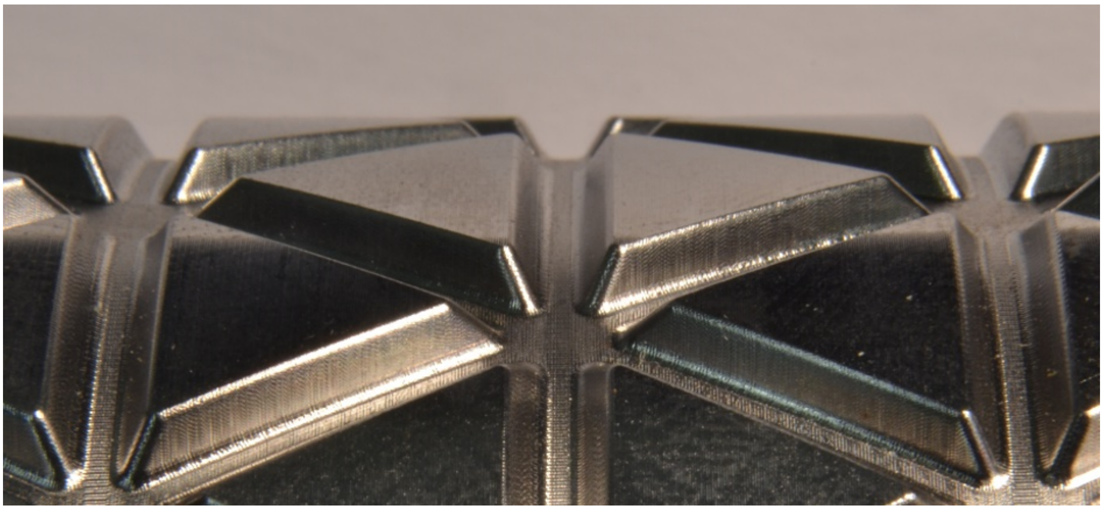

Figure 4.7 Close up of the roller showing the groove profile; the groove in the centre is in the 0°, or roll, direction

4.2 Isogrid rolling

Billets of AA1050 were sectioned from larger plates using either a guillotine or waterjet cutter. These billets were annealed prior to Isogrid rolling, to remove the cold work present from the H14 rolling to half hardness process. Annealing facilitated the introduction of greater deformation to the material without reaching the limit of its ductility and creating cracks. Billets of varying length, width and thickness were trialled; the maximum billet width and thickness compatible with the mill was 110mm and 4mm, respectively. No lubrication was added to the rollers.

Initial rolling was performed using 1mm thick billets of AA1050, but the resultant Isogrid was shallow as the material deforms in the rolling direction preferentially to filling the grooves perpendicular to the rolling direction [4.13]. Elongation prevented the billet from being rolled through the patterning process a second time as the rib lattice did not match on re-rolling. Subsequently, samples of Isogrid were successfully rolled from 3mm aluminium AA1050-O sheet as seen in Figure 4.8-4.10. The rolled sheets were initially 110 x 110 x 3mm. The roll gap was set to 0.75mm (25% of original thickness) using a feeler gauge which was accurate to ±0.05mm. During the rolling process, this gap expanded and settled at 1.3mm (43.33% of original thickness) [4.14].

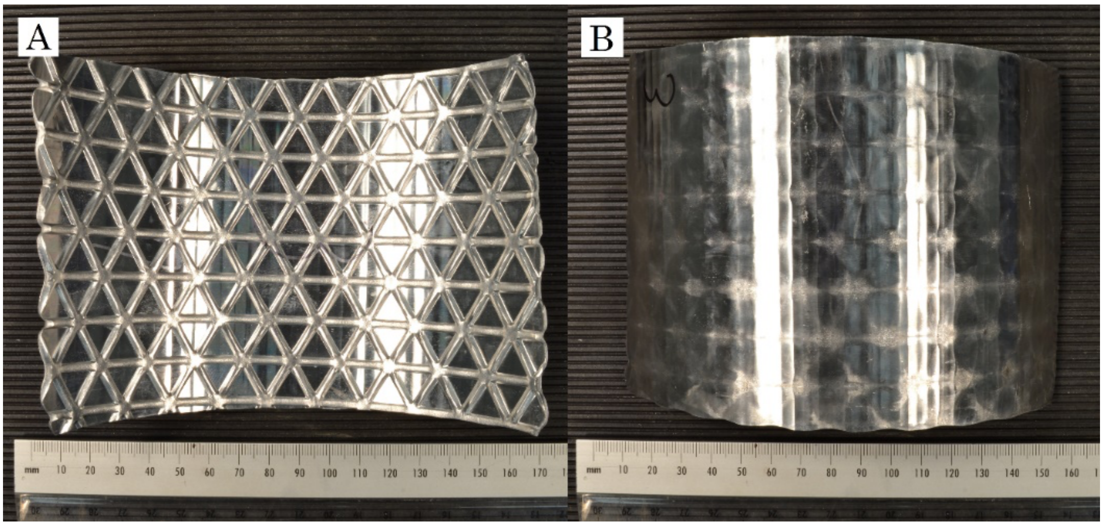

Figure 4.8 The ribbed (A) and reverse (B) side of the rolled Isogrid

Qualitative observations were made on the surface properties of the resultant Isogrid, as the sample plates were manufactured, which allowed further refinement of the technique. There was a tendency for the resultant structure to skew to one side if the billet entered at an angle. Curvature developed as the billet passed through the roll gap (Figure 4.8-4.9), as expected, due to the frictional and geometric asymmetry of the rollers which generates an imbalance in shear forces [4.15–4.17]. There are multiple potential methods to reduce this curling effect, such as using asymmetrically sized rollers; setting the rollers at different speeds during the process; implementing a post roll flattening stage; applying tension into the rolling process. Curling and flattening are intrinsic steps within industrial rolling processes, as sheet metal products are often coiled for transportation then flattened for usage [4.18].

The scope of this project focuses on developing the Isogrid rolling concept and leaves the development of a flattening method and other tolerancing issues to industry. The work required to implement one of the suggested solutions above is equivalent to that of establishing tolerances and control systems for the process, and while useful, is not of immediate scientific priority.

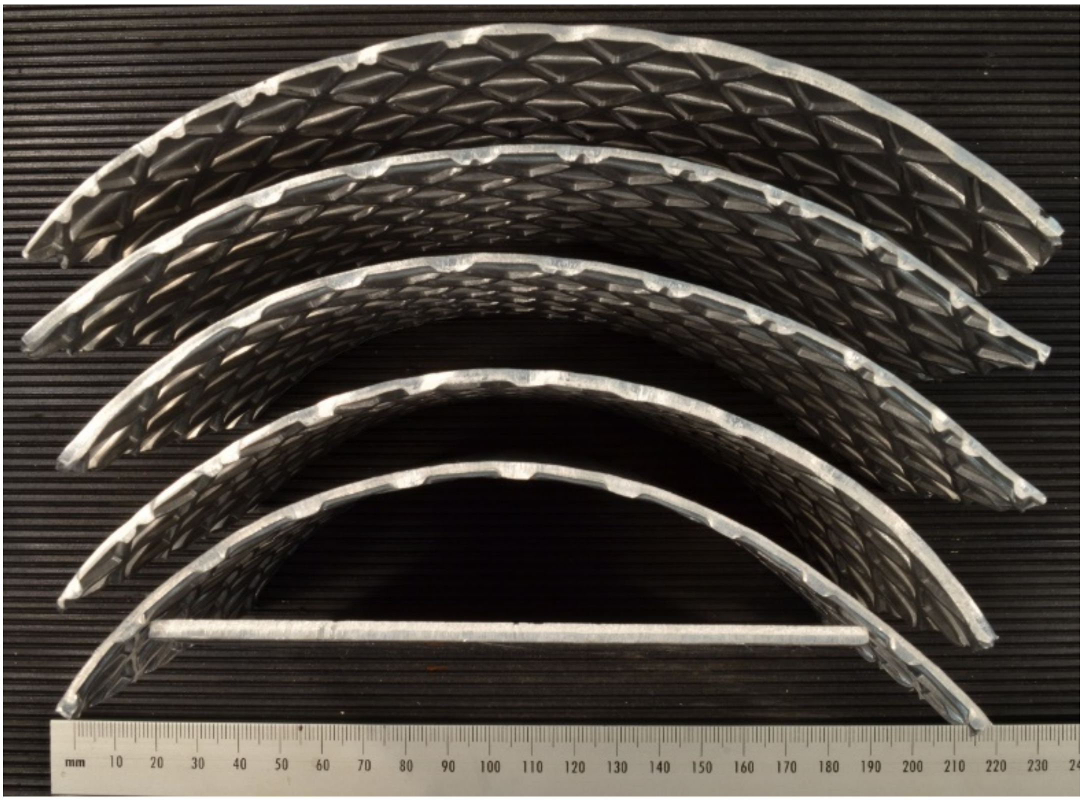

Figure 4.9 The rolled sample plates and an initial billet showing the curvature of the rolled Isogrid

As seen in Figure 4.10, the surface and morphology of the ribs varied depending on their direction. The 0° ribs (roll direction - Figure 4.10) were rounded and reduced in height in comparison to the ±60° ribs, which were taller and had flatter tops with sharper corners (Figure 4.10). A difference in formation between the rib directions can also be inferred by the texture of their surfaces; the ±60° ribs had filled more of the available volume in the groove resulting in a smooth top surface, whereas the 0° ribs were dimpled as they had not. This can be explained as the 0° ribs were following the roll direction, and thus could elongate preferentially over extruding into the roller's groove [4.13]. By contrast, the ±60° ribs were unable to extrude in the roll direction due to constriction by the groove geometry, which forced the material to fill the grooves. Microstructural evidence supporting these observations will be discussed further in section 5.5.

Rib formation defects were noted on the formed rib lattice, such as high points located approximately midway between nodes on the ±60° ribs (Figure 4.10-A), and rounded edges near the nodes on these same ribs (Figure 4.10-A). These issues are artefacts of material flow during the forming process and indicate that the groove geometry may need further optimisation to reduce inconsistencies. There was no evidence of cracking in the rolled Isogrid, despite the extensive deformation of the billet, and large strains imposed to reduce parts of the billet by 52% of the original thickness in one pass. On the reverse side of the plate, the position of the ribs can be seen by shallow recesses which formed along the rib directions (Figure 4.8 - B). These recesses are similar to "extrusion defects" as described by Sabroff et al. [4.13].

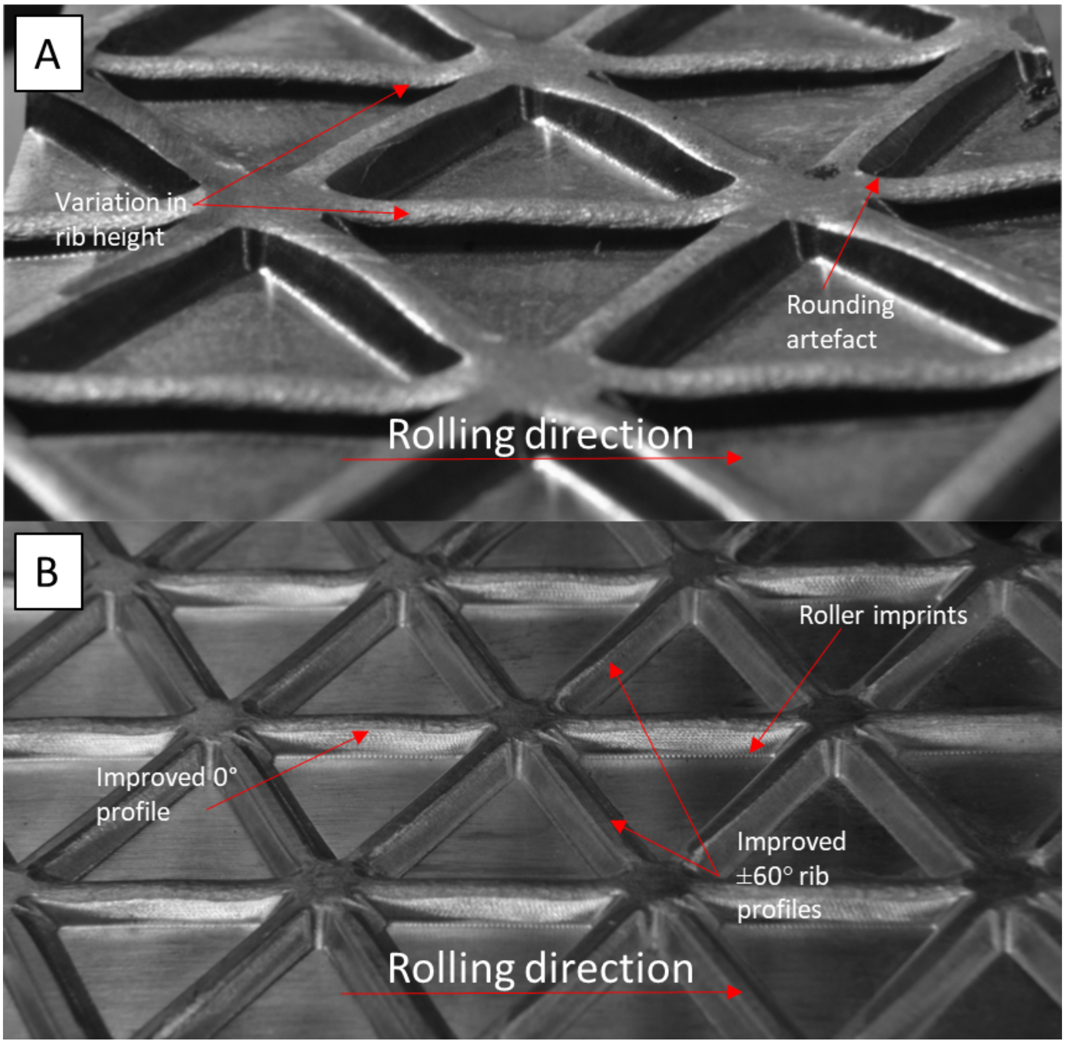

Figure 4.10 A perspective close up of the rolled Isogrid showing the variability in rolled ribs: A- 3mm billet, B- 4mm billet

The variation in rib geometry exhibited by the Isogrid rolled from 3mm billets created differences in cross sectional area across the final structure, which is a potential source of anisotropy. Improvements to these geometric variations in output (Figure 4.10 – A) were made by using a 4mm billet (Figure 4.10 – A). The consistency of rib height and profile were much improved for the 0° ribs (Figure 4.10 – B). The ±60° ribs (Figure 4.10 – B) had uniform height and flat top faces, indicating that they have fully filled the available groove volume. Some artefacts can be seen in Figure 4.10 – B, which are the imprints of the CNC machining process used to manufacture the Isogrid roller. Surface defects and artefacts from rolling processes are reported in the literature as sites of fatigue crack initiation [4.19].

The experimental implementation of the proposed process successfully produced Isogrid structures from annealed AA1050 billets. Iterative improvements were made to the process as billet thickness was altered, resulting in the production of more consistent rib lattices with minimal geometric inconsistencies. The microstructural properties and mechanical behaviour of these rolled Isogrid specimens will be examined in chapters 5 through 7, and compared to Isogrid manufactured through conventional CNC milling.

4.3 Reference List

[4.1] Meyer RR, Harwood OP, Harmon MB, Orlando JI. Isogrid design handbook. NASA 1973.

[4.2] Slysh P. Isogrid Structural Applications. Conference of the Society of Allied Weight Engineers 1976:27.

[4.3] Slysh P. Isogrid Structures Technology and Applications. San Diego: Society for Allied Weight Engineers; n.d.

[4.4] Slysh P, Dyer JE, Furman JH, Key JE. Isogrid Structures. AIAA/ASME/SAE 16th Structures, Structural Dynamics, and Materials Conference 1975. https://doi.org/10.2514/6.1975-816.

[4.5] Weritz J, Lampman S. Wrought Aluminum Processes and Products. Aluminum Science and Technology, ASM International; 2018, p. 255–78. https://doi.org/10.31399/asm.hb.v02a.a0006518.

[4.6] Witherall R. Specialisation leads AMAG to recovery. Aluminium Today 1999;11:43.

[4.7] Wang T, Gao XY, Zhang ZX, Ren ZK, Qi YY, Zhao JW. Interfacial bonding mechanism of Cu/Al composite plate produced by corrugated cold roll bonding. Rare Metals 2021;40:1284–93. https://doi.org/10.1007/s12598-020-01660-6.

[4.8] Wang T, Wang Y, Bian L, Huang Q. Microstructural evolution and mechanical behavior of Mg/Al laminated composite sheet by novel corrugated rolling and flat rolling. Materials Science and Engineering A 2019;765. https://doi.org/10.1016/j.msea.2019.138318.

[4.9] Li S, Luo C, Liu Z, Zhao J, Han J, Wang T. Interface characteristics and mechanical behavior of Cu/Al clad plate produced by the corrugated rolling technique. J Manuf Process 2020;60:75–85. https://doi.org/10.1016/j.jmapro.2020.10.015.

[4.10] Wang T, Li S, Ren Z, Han J, Huang Q. A novel approach for preparing Cu/Al laminated composite based on corrugated roll. Mater Lett 2019;234:79–82. https://doi.org/10.1016/j.matlet.2018.09.060.

[4.11] García-Gil G, Colás R. Calculation of thermal crowning in work rolls from their cooling curves. vol. 40. 2000.

[4.12] Colbourne J. The Geometry of Involute Gears. Edmonton: 1987.

[4.13] Sabroff AM, Boulger FW, Henning HJ, Spretnak JW. A manual on Fundamentals of forging practice. 1964.

[4.14] Garrick AJH, Toumpis AI, Galloway AM. Developing a novel manufacturing method to produce stiffened plate structures. International Journal of Advanced Manufacturing Technology 2021:2805–13. https://doi.org/10.1007/s00170-020-06525-x.

[4.15] Pośpiech J. A note on the influence of some factors affecting curvature in the flat rolling of strip. Journal of Mechanical Working Technology 1987;15:69–80. https://doi.org/10.1016/0378-3804(87)90007-6.

[4.16] Knight CW, Hardy SJ, Lees AW, Brown KJ. Influence of roll speed mismatch on strip curvature during the roughing stages of a hot rolling mill. J Mater Process Technol 2005;168:184–8. https://doi.org/10.1016/j.jmatprotec.2004.09.094.

[4.17] Knight CW, Hardy SJ, Lees AW, Brown KJ. Investigations into the influence of asymmetric factors and rolling parameters on strip curvature during hot rolling. J Mater Process Technol 2003;134:180–9. https://doi.org/10.1016/S0924-0136(02)00469-7.

[4.18] Chashchin V v. Controlled Cooling of Strip Coils on the Conveyer of a Hot-Rolling Mill. Steel in Translation 2018;48:388–92. https://doi.org/10.3103/S0967091218060025.

[4.19] Waqas Tofique M, Bergström J, Burman C. Very high cycle fatigue crack initiation mechanisms in different engineering alloys. Procedia Structural Integrity, vol. 2, Elsevier B.V.; 2016, p. 1181–90. https://doi.org/10.1016/j.prostr.2016.06.151.

5 Microstructural comparison of Rolled and CNC Isogrid

5.1 Microstructure and manufacturing

Commercially pure aluminium (AA1050) is a polycrystalline material, with a face centred cubic (FCC) crystalline structure [5.1]. As described in Chapter 3.1, AA1050 is a wrought alloy, so its hardness and strength can be enhanced by the introduction of cold work [5.2–5.4]. Cold work is the strengthening of a material due to dislocation entanglement caused by plastic deformation [5.1,5.5,5.6]. Plastic deformation is enabled on the atomic scale by the generation and movement of dislocations, which are defects in the crystal lattice [5.5,5.6]. As AA1050 is plastically deformed, these dislocations slide along slip planes until they either meet a grain boundary, become entangled with another dislocation, or are annihilated by a dislocation of the opposite polarity [5.1,5.6].

Dislocations are necessary to plastically deform a material, but the build-up of dislocations creates distortion in the crystal structure, inhibiting the formation and movement of further dislocations. This reduction in dislocation generation and mobility increases the hardness and strength of the material while reducing its ductility [5.7]. The microstructural effects of cold work can be alleviated by annealing, a process in which a metallic material is heated to allow new grains to nucleate, existing grains to grow and dislocation density to decrease via annihilation [5.1,5.8–5.10]. Annealing allows repeated plastic deformation in AA1050 which would otherwise be impossible due to the accumulation of dislocations [5.11,5.12]. The typical hardness value for AA1050 in its annealed state is 20Hv, rising to 34Hv after cold working [5.13].

Stacking fault energy (SFE) is a material property which quantifies the energy of faults within the material lattice and the number of slip systems a dislocation can activate [5.14–5.16]. Aluminium has a high SFE which enables dislocations to move in multiple planes and avoid obstacles in a process known as cross-slip [5.15,5.17,5.18]. The availability of cross slip as a mechanism of dislocation movement increases the mobility of dislocations within the aluminium lattice. This, in turn, allows aluminium to undergo extensive plastic deformation before cold work embrittles the material to the point of fracture. This ductility gives aluminium excellent formability which makes it well suited for forming processes [5.18]. Materials with a lower SFE are less ductile and tend to create partial dislocations such as deformation twins [5.19].

Rolling operations have a profound and distinct set of effects on metallic microstructures, which have been reported throughout the scientific literature [5.15,5.19–5.23]. The microstructural evolution of AA1050 during cold rolling is characterised solely by the development of cold work through plastic deformation [5.22,5.24]. Cold rolling imparts plastic deformation into the material through a 2D plane strain system of stresses [5.7,5.25–5.27]. Grain refinement and lattice rotation are enabled as dislocations glide and entangle to form dislocation cells [5.28,5.29]. Bay et al. [5.24] demonstrated in detail these grain refinement mechanisms, through which larger grains were subdivided into smaller volumes by the accumulation of dislocations according to the constraints of their slip mechanisms. The degree of rolling induced microstructural evolution varies through the thickness of the rolled sheet as a function of process parameters such as roller diameter, roller lubrication, billet dimensions and thickness reduction [5.19,5.30].

During rolling, grains are elongated in the rolling direction and compressed in the normal direction (through thickness), leading to a fibrous grain structure composed of high aspect ratio, acicular grains [5.15,5.22,5.23,5.31,5.32]. This elongation reorganises the grain structure such that specific crystallographic orientations emerge as dominant with respect to the rolling direction [5.15,5.19–5.22]. Dillamore et al. [5.15] explain that microstructures under uniaxial loading rotate so the ⟨111⟩ slip systems are parallel (tension) or orthogonal (compression) to the axis of loading; however, standard rolling is more complex as it is a biaxial stress system in which both tension (in the rolling direction) and compression (in the thickness direction) are present. Bay et al. [5.24] documented this reorientation of the grain structure relative to the rolling direction in detail using transmission electron microscopy.

The statistical analysis of grain orientation is known as texture analysis and the presentation of texture data via pole figures, inverse pole figures and orientation distribution functions (ODFs) is a well-established method for the analysis of metal forming processes [5.15,5.19,5.21,5.33]. The literature on the texture analysis of cold rolled AA1050 is well developed, with widespread scientific consensus on the deformation mechanisms and the resultant textures expected [5.15,5.19–5.23,5.34,5.35]. The forces and deformations of any material subjected to symmetrical plain rolling can be represented by a plane strain model [5.7,5.26,5.27,5.36–5.38]. Figure 5.1 shows an ODF space containing the typical textures found in rolled AA1050 resulting from plane strain deformation [5.21]. The α and β fibres in Figure 5.1 represent the progression of deformation textures which aluminium and other FCC metals experience as they are subjected to increasing degrees of thickness reduction via rolling. Notable textures along these fibres are Goss {110}⟨001⟩, brass {110}⟨112⟩, s {153}⟨112⟩, and copper {211}⟨111⟩ [5.39]. The initial Goss to brass textures are seen in lightly rolled samples. The brass and copper textures are named after the materials in which they were clearly identified after rolling. Brass has a lower SFE and thus reduced formability during rolling, whereas copper has a high SFE and exhibits excellent ductility. Consequently, the brass texture is present after small reductions via rolling, whereas the copper texture is seen after significant deformation. The ODF space is often represented using sections of constant ϕ2 values for simplification (Euler angle – see Figure 5.1) [5.33].

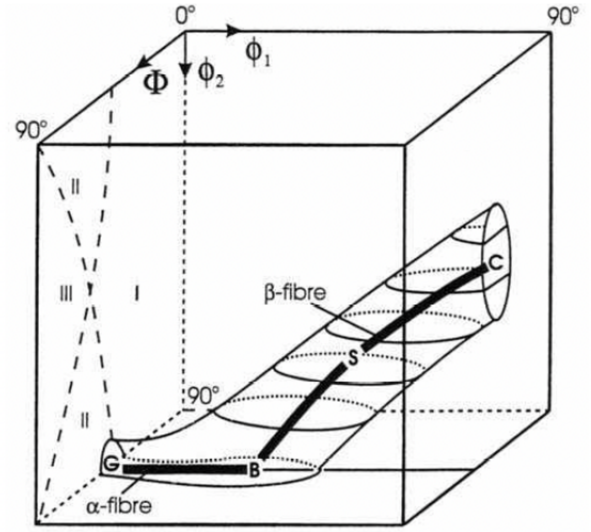

Figure 5.1 Standard named texture components found in rolled FCC. G – Goss, B – Brass, S – S, C – Copper. [5.22]

The recrystallisation mechanism of typical FCC rolled textures (such as brass {110}⟨112⟩ and copper {211}⟨111⟩ during annealing treatments is equally well represented in the literature [5.10,5.19,5.35,5.40]. Cube {001}⟨100⟩, rotated cube {001}⟨110⟩ and Goss {011}⟨100⟩ are recrystallisation textures which nucleate when annealing rolled AA1050 and continue to grow under annealing conditions to form a fully recrystallised texture [5.21,5.34,5.35,5.41,5.42]. Alvi et al. [5.34] found that cube recrystallisation textures grow more prolifically within S orientated grains, whereas brass and copper grains were slower to recrystallise. The work conducted by Helbert et al. [5.10] showed the results of partial recrystallisation on rolled AA1050, in which both recrystallisation textures and rolling deformation textures remain present in the sample. Figure 5.2 contains keys for use throughout this chapter to identify relevant rolling deformation textures and recrystallisation textures.

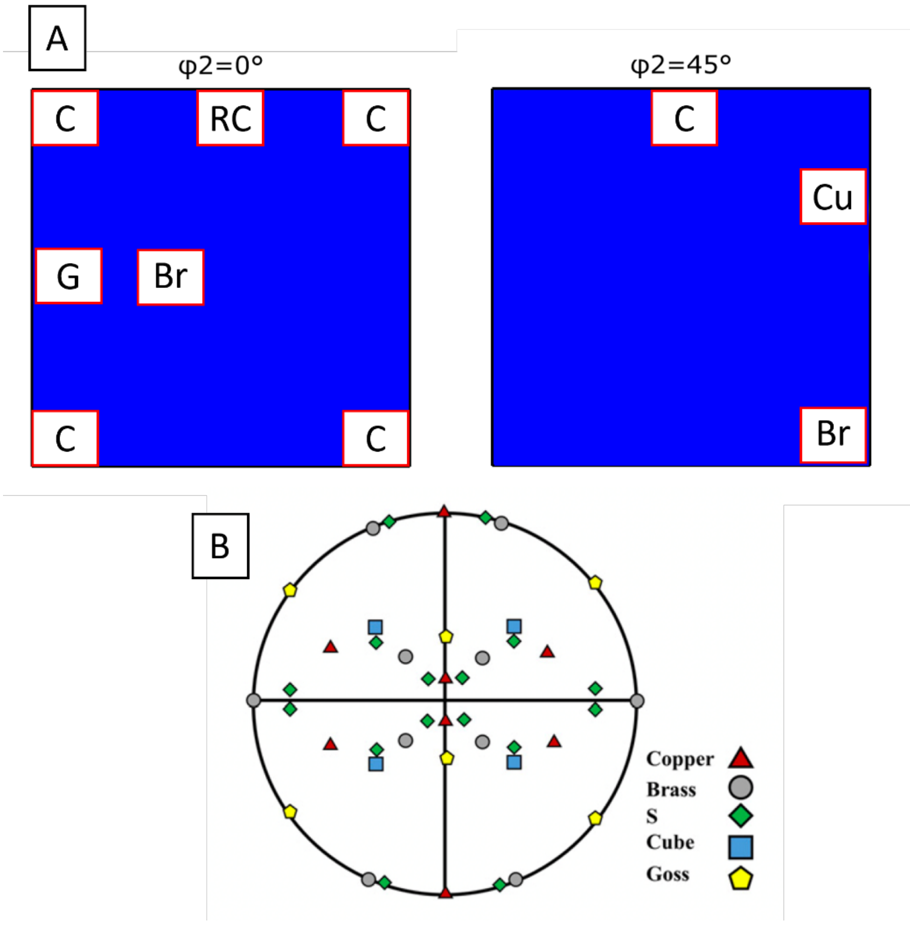

Figure 5.2 A – ODF key, C - cube, G - Goss, Br - Brass, Cu – Copper, RC- rotated cube, B – pole figure key [5.43]

Severe plastic deformation methods are in development to maximise the potential benefits of highly refined grain structures through cold work [5.3,5.28,5.44–5.46]. Asymmetric rolling has been shown by Jiang et al. [5.46] to effectively produce an ultrafine grain structure with enhanced mechanical properties compared to standard symmetrical rolling practices. Equal channel angular pressing has also been proven effective as a severe plastic deformation method which forces a billet through a channel containing an abrupt change in direction to refine the grain structure and increase strength [5.3,5.44,5.45]. Similarly, Hajizadeh et al. [5.28] developed a method of grain refinement via repeated corrugation and flattening which produced a 90% increase in yield strength and 70% increase in ultimate tensile strength via severe plastic deformation.

The use of cold work to improve mechanical properties is limited by a material's ductility, or percentage elongation, before fracture under certain loading conditions. This is presented in the literature using the forming limit diagram [5.47,5.48]. Work by Gotoh et al. [5.48] reveals that including out of plane loading within plane strain deformation mechanisms increases the workable range of plastic deformation, therefore expanding the forming limits of a material. Using this same principle, Allwood et al. [5.49,5.50] reports a novel variation on single point incremental forming which introduces shear forces to a workpiece by means of a rotating paddle. The paddle forming method has been shown to facilitate greater deformations than conventional single point forming methods, thus enabling greater degrees of microstructural evolution and property enhancement [5.51]. Similarly, in the Isogrid rolling process detailed in Chapter 4, the 3D nature of the rib geometries and asymmetry between the rollers are likely to induce shear forces into the billet and alter the forming limits of the aluminium.

In the present study, billet material, rolled Isogrid and CNC Isogrid were sectioned and analysed in both their as produced state and after an annealing treatment to compare their microstructural characteristics and develop an understanding of the processes by which they were created. The microstructure of each sample was analysed using a combination of optical microscopy, Electron backscatter diffraction (EBSD) analysis and hardness measurements. The results are presented by sample location and state for clarity due to the number and similarity of sample types. Relevant results for comparison are collated in Table 5.1 at the end of the results section.

5.2 Results

5.2.1 Stock material

Figure 5.3 shows a full thickness cross section of the 4mm AA1050 billet in its H14 state (Figure 5.3-A) and its fully annealed O state (Figure 5.3-B). The difference in grain morphologies between the states presented in Figure 5.3 is evident as the size, shape and homogeneity of these grain structures have all been transformed by the heat treatment. The H14 state represents material which has been "rolled to half hardness" by imparting cold work into the billet [5.52]. The microstructure in Figure 5.3-A contains evidence of this cold work via the presence of acicular grains which have been flattened during the rolling process. The size of grains in Figure 5.3-A is also variable, with smaller grains found near the surfaces of the cross-section, and larger grains throughout the midplane. Humphreys et al. [5.19] noted the existence of such variations in the cross section, attributing their formation to

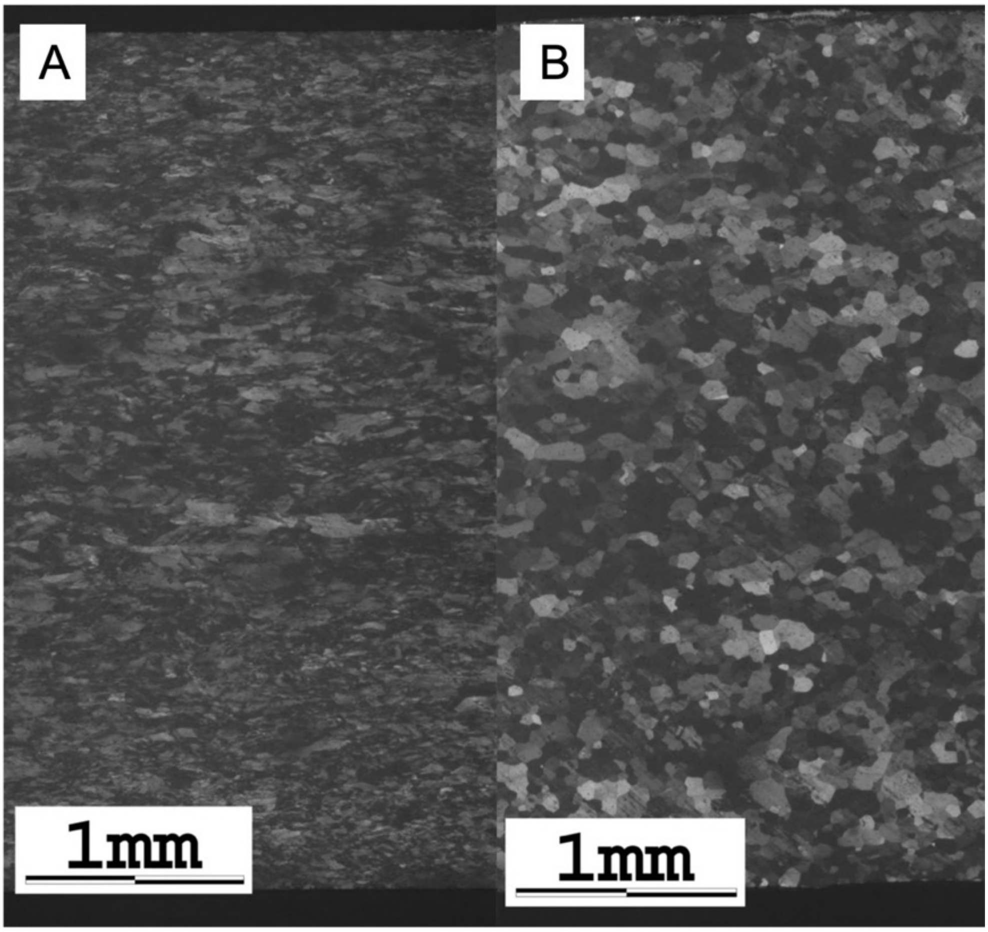

Figure 5.3 Etched cross section of AA1050 in the: A- rolled to half hardness state (-H14), B- annealed state (-O)

interactions with shear forces at the roller face. The grain structure of the annealed samples has been homogenised in comparison (Figure 5.3-B), containing equiaxed grains, which are of a consistent size and shape throughout the thickness of the cross-section. Hardness measurements conducted on the surface of the material in both states found the hardness of the initial billet in its H14 state was 42Hv, reducing to 21Hv after annealing to the O state, as described in section 3.1. These hardness values agree with those found in the literature [5.13,5.52].

5.2.2 CNC milled Isogrid

The Isogrid samples milled from the 3mm AA1050 stock provide an excellent baseline for the discussion of the other microstructures in this chapter. The etched cross section of milled Isogrid shown in Figure 5.4 displays a deformed microstructure with acicular grains. This appears different to the microstructure presented in Figure 5.3-A, as the cross section has been taken parallel to the rolling direction to emphasize the acicularity of the grains. Although Figure 5.3-A was sectioned normal to the rolling direction, the microstructures are the same. A gradient in grain size can be seen throughout both Figure 5.3 and Figure 5.4 as expected after an H14 rolling process with larger grains in the mid-section of the sheet and thinner grains closer to the surface [5.19,5.30]. Figure 5.4-A and Figure 5.4-B show the grain structure at an Isogrid node and skin section, respectively. The milling process has had no effect on the microstructure in these locations, as these micrographs present no differences from that seen through the rest of this cross section. There is a sharp transition between skin and rib section in Figure 5.4-C, which illustrates the interruption in grain structure where the milling process has removed material.

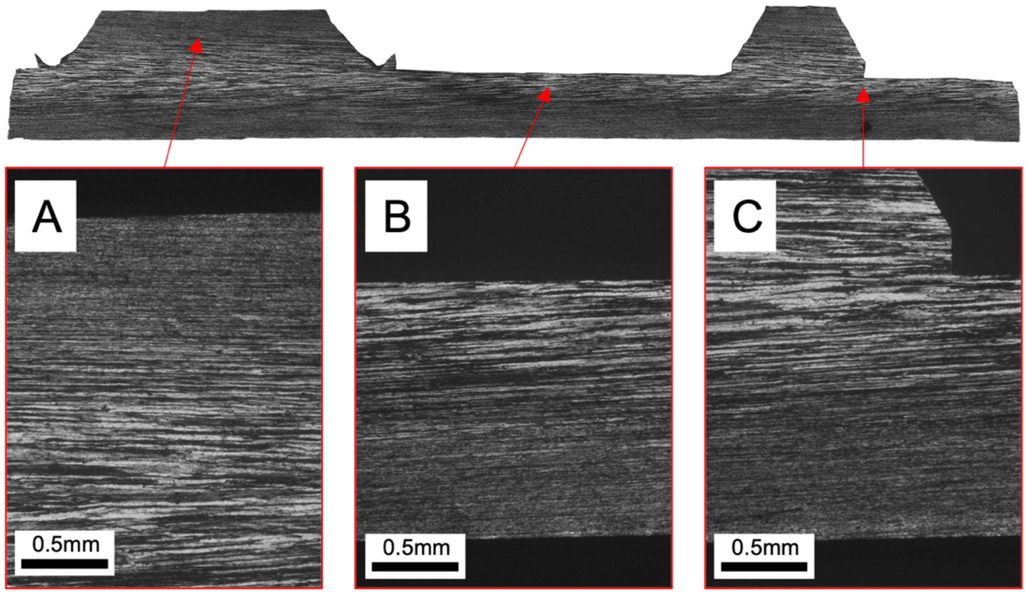

Figure 5.4 Etched micrographs of CNC milled Isogrid (as machined, x50 magnification): A- node section, B- skin section, C- rib-skin transition

An EBSD grain map of the CNC milled Isogrid taken in the node area of the cross section (Figure 5.4-A) is presented in Figure 5.5. The grains are highly acicular-shaped, with an average grain size of 9.8µm and an aspect ratio of 4.3 (see Table 5.1). The gradient in grain thickness is visibly prominent as the grains at the top of the figure are much thicker than those at the bottom (approaching the rolled surface). This is in line with the findings of Hallberg et al. [5.53] that the microstructural effect of rolling is more pronounced in proximity to the rollers during the cold rolling process.

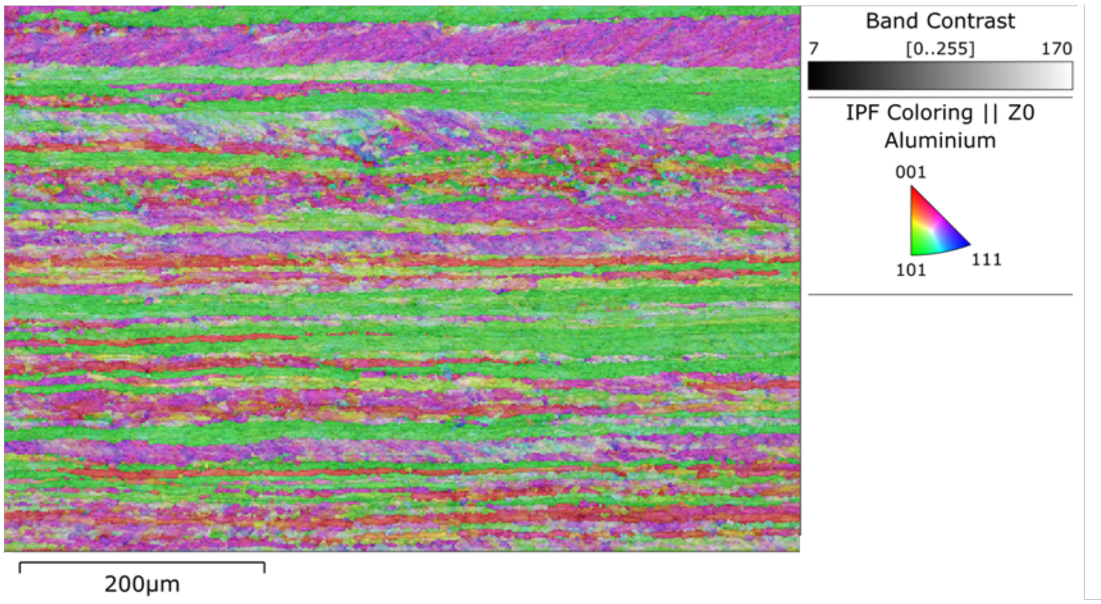

Figure 5.5 EBSD mapping of CNC milled Isogrid (as machined – node section)

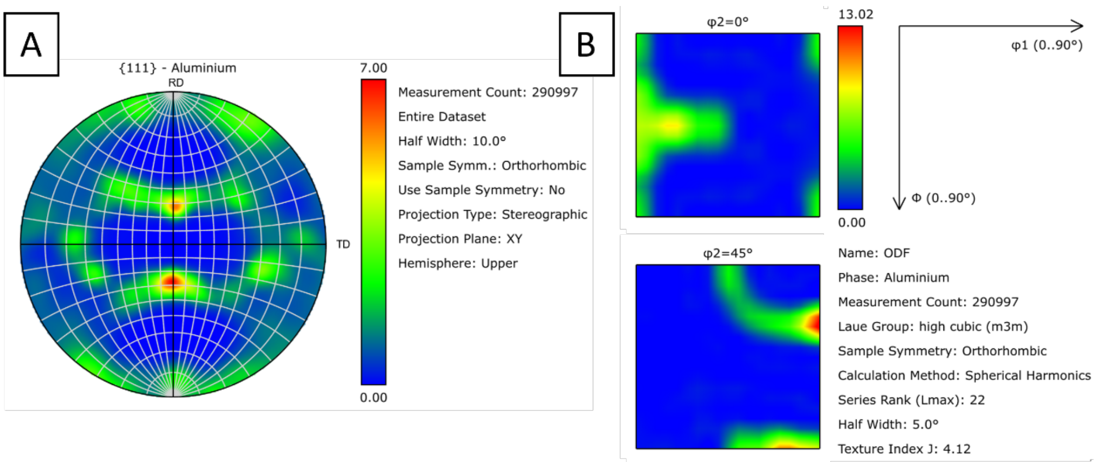

Figure 5.6 A – pole Figure, B – relevant ODF sections for CNC milled Isogrid (as machined – node section)

The texture of the CNC milled Isogrid is typical of a cold rolled AA1050 microstructure in both its {111} pole figure (Figure 5.6-A) and ODF (Figure 5.6-B) [5.15,5.19,5.21,5.22]. The pole figure shows a contour plot characteristic of a brass texture [5.22]. The ODF sections at 0° and 45° show a combination of cube, Goss, brass, and copper textures [5.22]. The work by Hirsch et al. [5.22] reports an identical pole figure and ODF as the resultant texture for cold rolled aluminium.

The EBSD mapping of the skin section of the CNC milled Isogrid (Figure 5.4-B) in Figure 5.7 contains a more intense texture than that of the node section. The homogeneous colouration is an indication that grains near the surface of the material have become aligned to the same crystallographic direction during the roll-hardening process. As the skin section lies closer to the rolled face of the billet material, this is evidence, in agreement with the literature, that the microstructural effects of rolling are greater in proximity to the roller [5.53]. The average grain size was calculated to be 13.7µm with an aspect ratio of 6.4 (see Table 5.1).

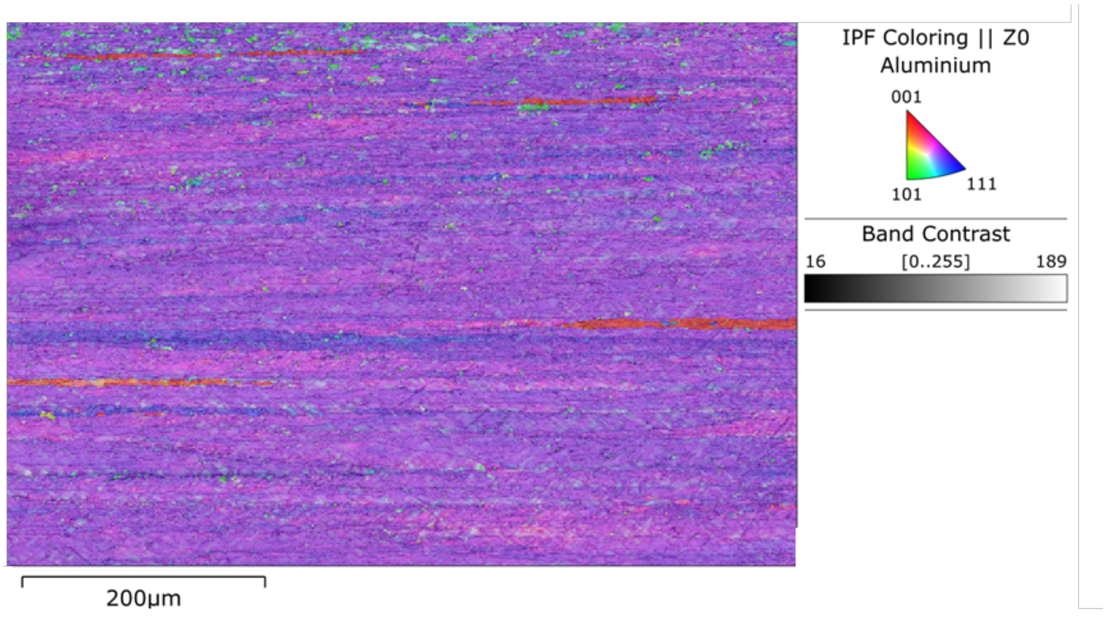

Figure 5.7 EBSD mapping of CNC milled Isogrid (as machined - skin section)

The {111} pole figure and ODF presented in Figure 5.8 provide further evidence for this finding, as both display a heavily rolled texture. The pole figure (Figure 5.8-A) contours are arranged in a brass formation [5.22,5.39] and the intensity of the ODF contour is 53.26 for the copper component of the 45° section (Figure 5.8-B) [5.22]. These texture intensities are 53 times more intense than a random distribution, indicating that these textures are strong, and a corresponding high degree of anisotropic mechanical behaviour may be present in this sample [5.21], as will be discussed in Chapter 6.

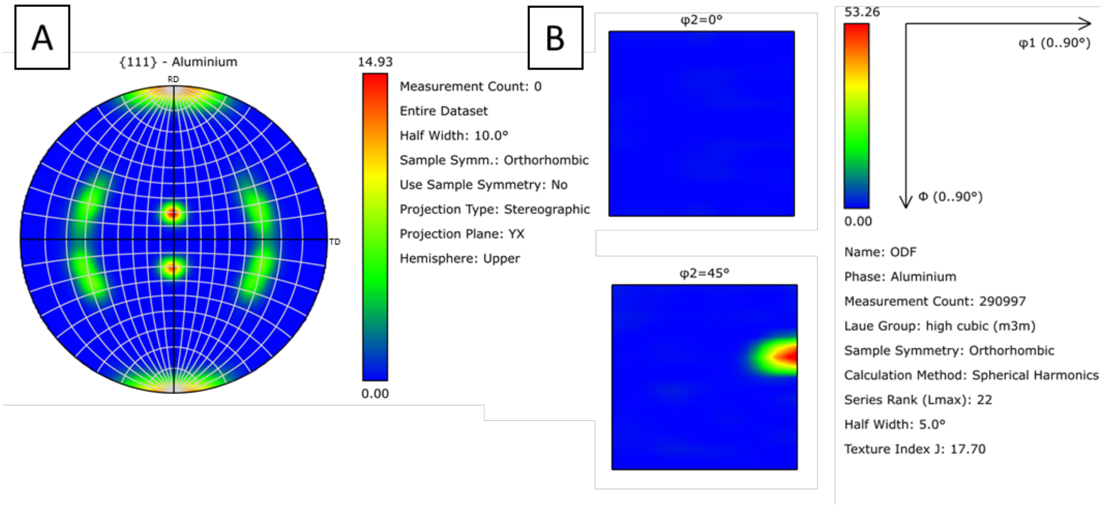

Figure 5.8 A – pole figure and B – relevant ODF sections for CNC milled Isogrid (as machined – skin section)

Microhardness measurements of the CNC milled Isogrid (Figure 5.9) revealed a homogenous hardness distribution throughout the cross section with values in the range of 40-55Hv. These values are close to the range stated by Bay et al. [5.13], for cold worked AA1050.

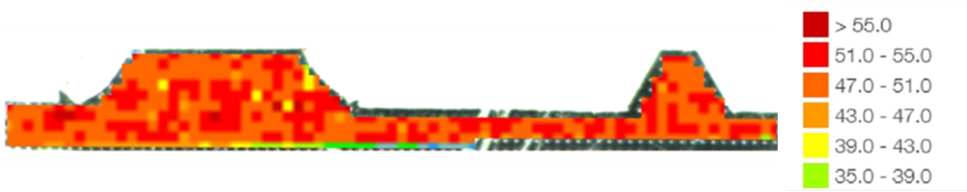

Figure 5.9 Microhardness map of CNC milled Isogrid (as machined)

5.2.3 CNC milled Isogrid post-annealing

The CNC milled Isogrid in the post-annealed condition displayed standard microstructural features for AA1050 which has been rolled then annealed (O condition). The grains in Figure 5.10 have coarsened compared to those in the H14 condition (Figure 5.4). Where the H14 grains were acicular, the annealed grains are equiaxed with a lower aspect ratio. The gradient in grain size is still present, as previous areas of grain refinement provide increased opportunity for nucleation during the recrystallisation process. Figure 5.10-A and 10-B show the node and skin section, respectively, which correspond with the EBSD analyses in Figure 5.11-12. Little evidence of the milling process can be seen in Figure 5.10-A and Figure 5.10-B; however, a thin layer of small grains can be seen on the milled diagonal surface in Figure

5.10-D. These grains have recrystallised from a minimal layer of surface strain imparted during the milling process, known as a Beilby layer [5.54–5.56].

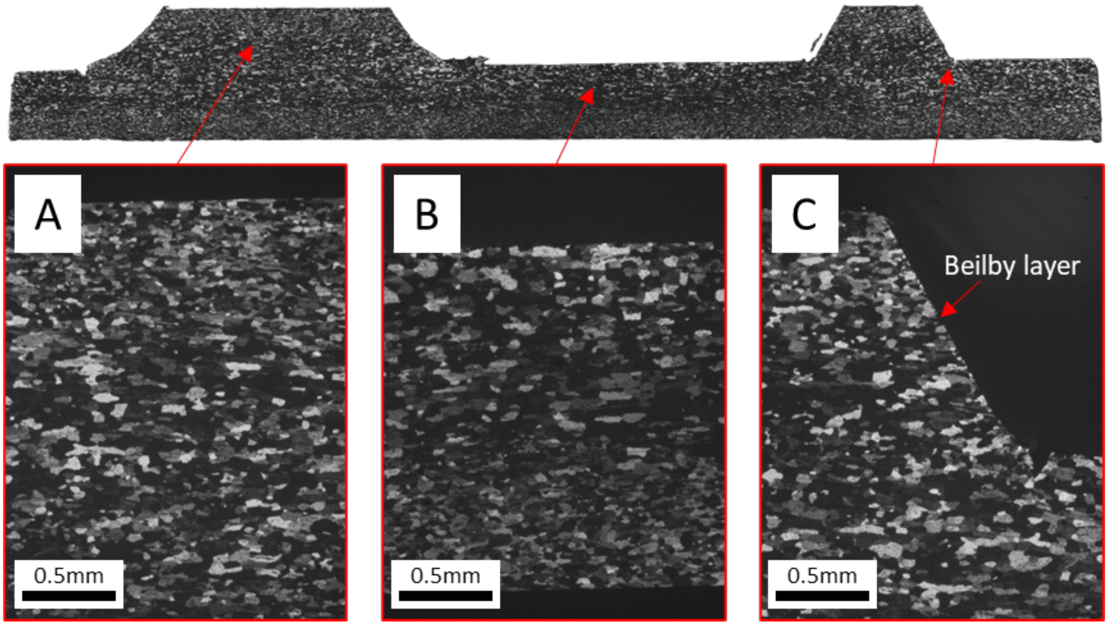

Figure 5.10 Etched micrographs of CNC milled Isogrid (annealed, x50 magnification): A – node section, B – skin section, C – rib-skin transition

Figure 5.11 presents an EBSD grain map of the annealed CNC milled Isogrid taken at the node area of the cross section (Figure 5.10-A). The coloured grain map in Figure 5.11 shows a combination of larger elongated grains and smaller equiaxed grains. The larger grains have experienced growth from the H14 condition during the annealing process, whereas the smaller equiaxed grains have recrystallised at nucleation sites in grain boundaries. The average grain size was calculated to be 35.8µm with an average aspect ratio of 2.4 (see Table 5.1).

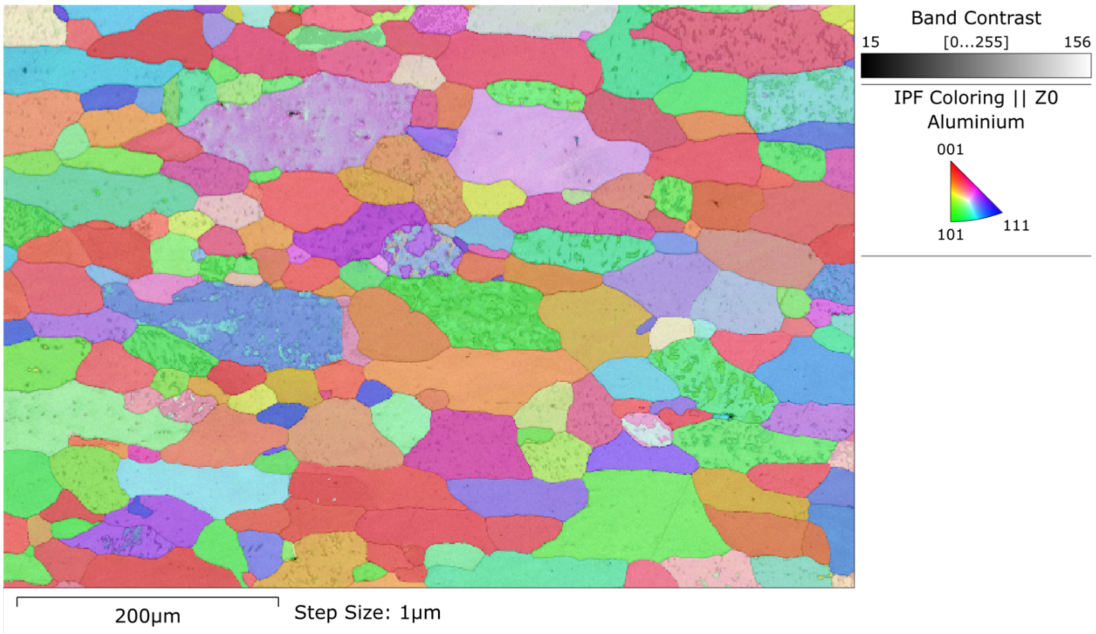

Figure 5.11 EBSD mapping of CNC milled Isogrid (annealed – node section)

The {111} pole figure in Figure 5.12-A shows clear Goss and cube textures which is typical of FCC recrystallisation after rolling [5.8,5.57]. The ODF (Figure 5.12-B) further supports this, as the 0° section has clear concentrations of intensity at the corners, indicating a cube texture, and a goss concentration on the centre of the left face. Further concentrations in the 0° and 45° sections indicate the presence of some brass texture remaining from the rolling process [5.19]. The intensities of these textures are high (11.3 on the ODF) and may indicate anisotropic mechanical behaviour [5.21].

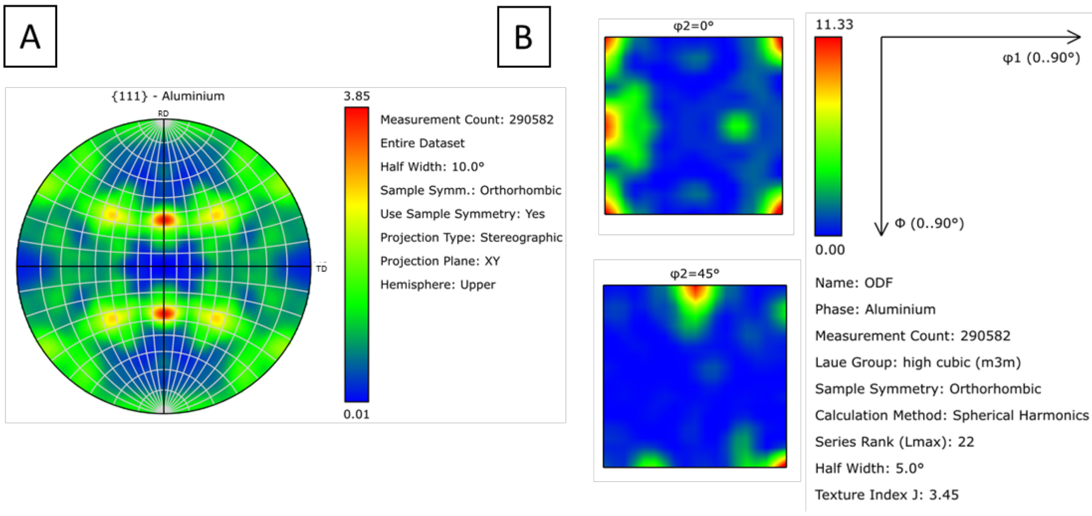

Figure 5.12 A – pole figure, B – relevant ODF sections for CNC milled Isogrid (annealed – node section)

Microhardness measurements of the annealed CNC milled Isogrid (Figure 5.13) revealed a homogenous hardness distribution throughout the cross section in the range of 15-27Hv. These values are consistent with the literature on annealed AA1050 [5.13].

Figure 5.13 Microhardness map of CNC milled Isogrid in post-annealed condition

5.2.4 Rolled Isogrid

The microstructure of rolled Isogrid, as seen in Figure 5.14, displays a wide variety of morphologies including deformed acicular grains and recrystallised equiaxed grains (Figure 5.14). Figure 5.14-A presents the microstructure of the skin section which underwent the most deformation to achieve the Isogrid geometry. The grains present in this section have a higher aspect ratio than those in the node (Figure 5.14-B), which infers greater plastic deformation imparted into this section. The extent of grain deformation and cold work seen in this micrograph is similar to the rolled grain structure seen in the stock material (Figure 5.3-A) and CNC Isogrid (Figure 5.4-A). The equiaxed grains at the node (Figure 5.14-B) and ribs remain mostly unaltered when compared to the stock material in its annealed state prior to rolling. Figure 5.14-C shows the transition from deformed grain structure in the skin section to equiaxed grains throughout the rib lattice. The deformed grains at the shoulder of the rib section have elongated and become acicular, following the formed contour of the cross section.

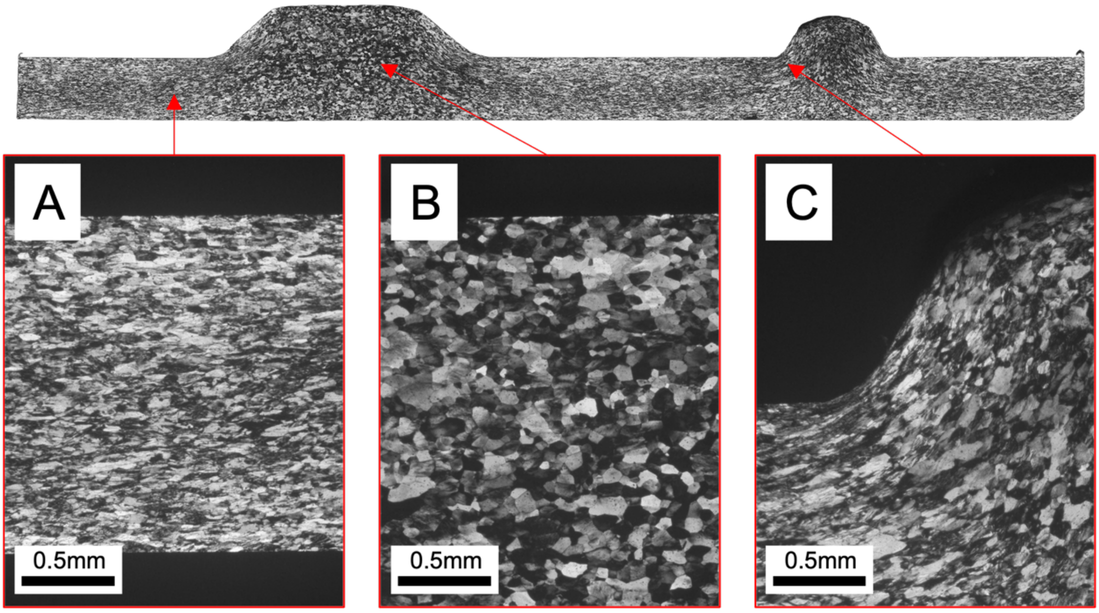

Figure 5.14 Etched micrographs of rolled Isogrid (as rolled, x50 magnification): A – skin section, B – node section, C – rib-skin transition

A mid plane section of the rolled Isogrid was etched, to generate a top down of the grain structure developed through the Isogrid rolling process (Figure 5.15). The figure is composed of 49 separate etched micrographs taken at x50 magnification, stitched together in a 7x7 matrix. There are three rib directions visible, with the figure centred on a rib in the rolling 0° direction, and two ±60° ribs converging in a node at the top centre of the figure. Similarities can be observed between Figure 5.14 and Figure 5.15, with equiaxed grains visible in the node/ribs and more deformed grains in the skin section. The transition zone between skin and ribs is deformed as seen in Figure 5.14-C, and this band of acicular grains highlights the edges of the rib lattice. The grains on the 0° rib display a higher level of deformation and greater aspect ratio than those in the ±60° ribs and node, having developed a degree of elongation in the rolling direction which is not present in other areas.

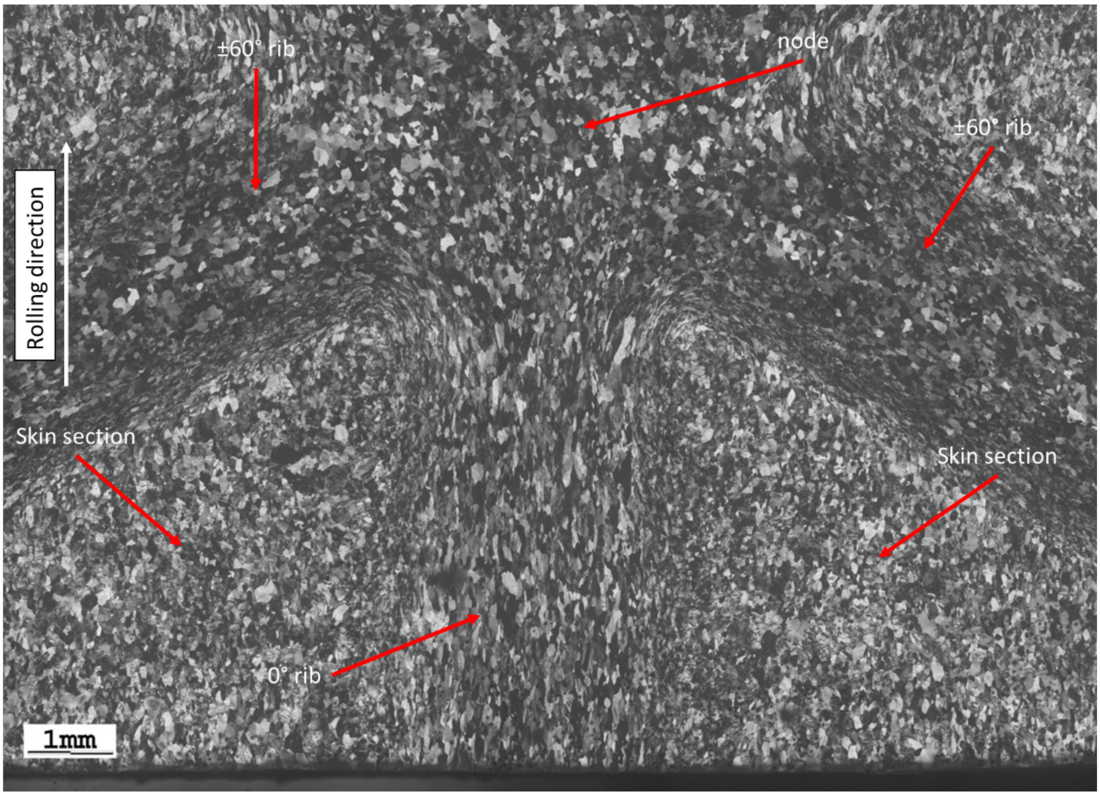

Figure 5.15 Etched micrograph of rolled Isogrid (as rolled – plan view)

The grains shown in the EBSD mapping of the skin section (Figure 5.16) are deformed, containing variation characteristic of cold work [5.58,5.59]. The average grain size is 13.4µm with an aspect ratio of 3.2 (see Table 5.1).

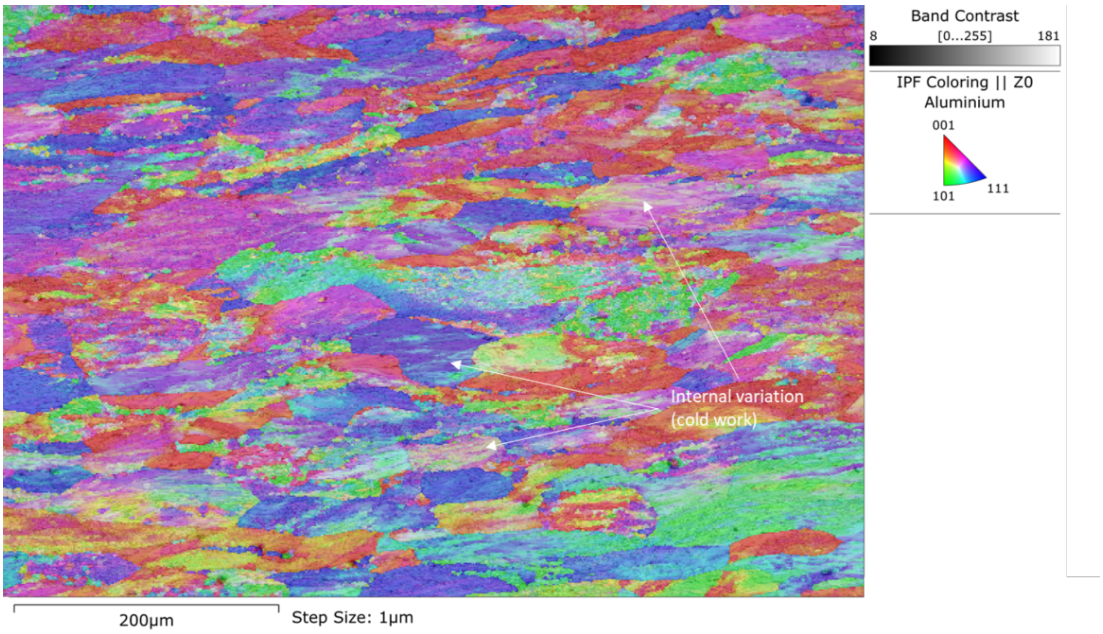

Figure 5.16 EBSD mapping of rolled Isogrid (as rolled - skin section)

Determining texture from Figure 5.16 alone would be difficult as it contains grains in all orientations like the annealed samples. However, the pole figure in Figure 5.17 shows a similar copper pattern to that seen in the skin of the CNC milled Isogrid (Figure 5.8-A). A nearly identical pole figure can be seen in Hjelen et al. [5.57] for cold rolled aluminium. The ODF (Figure 5.17) contains a distinct copper texture component in the 45° section. The 0° section presents a set of contours between the cube and rotated cube textures which indicate the presence of shear deformation mechanisms during rolling [5.60,5.61]. The intensity of the pole figure and ODFs is low, which, in parallel with multiple identified textures, indicates that the deformation texture in this condition is much weaker than that of the CNC samples. This indicates there will be more isotropic mechanical properties in the rolled Isogrid, which will be discussed in Chapter 6 [5.21].

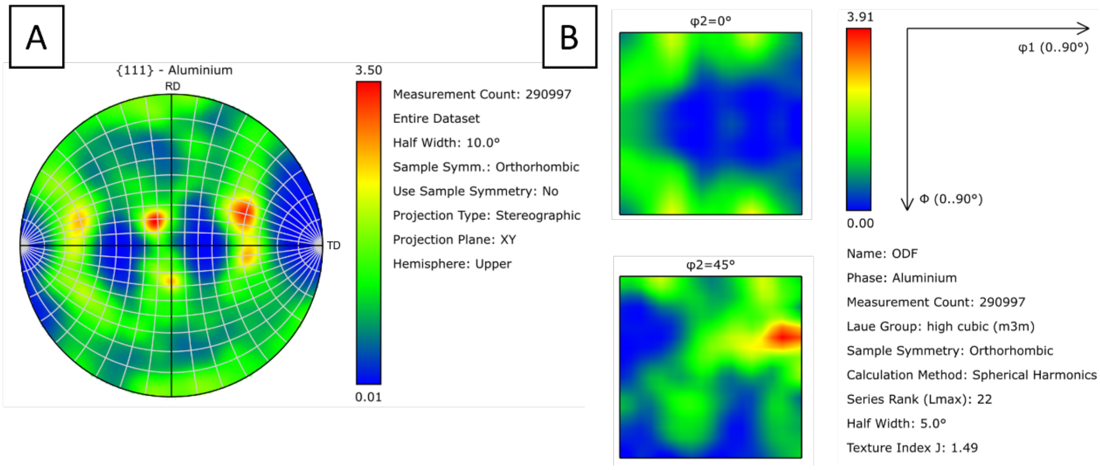

Figure 5.17 A - pole figure, B – relevant ODF sections for rolled Isogrid (as rolled – skin section)

The EBSD grain map of the rolled Isogrid node section (Figure 5.18) also appears similar to an annealed microstructure, containing large grains oriented in many directions; however, the grains have an increased aspect ratio in comparison to the equiaxed microstructure seen in Figure 5.11. Some of the grains contain internal variation which may be indicative of plastic deformation [5.58,5.59]. The average grain size in this area is 22.6µm with an aspect ratio of 2.4 (see Table 5.1).

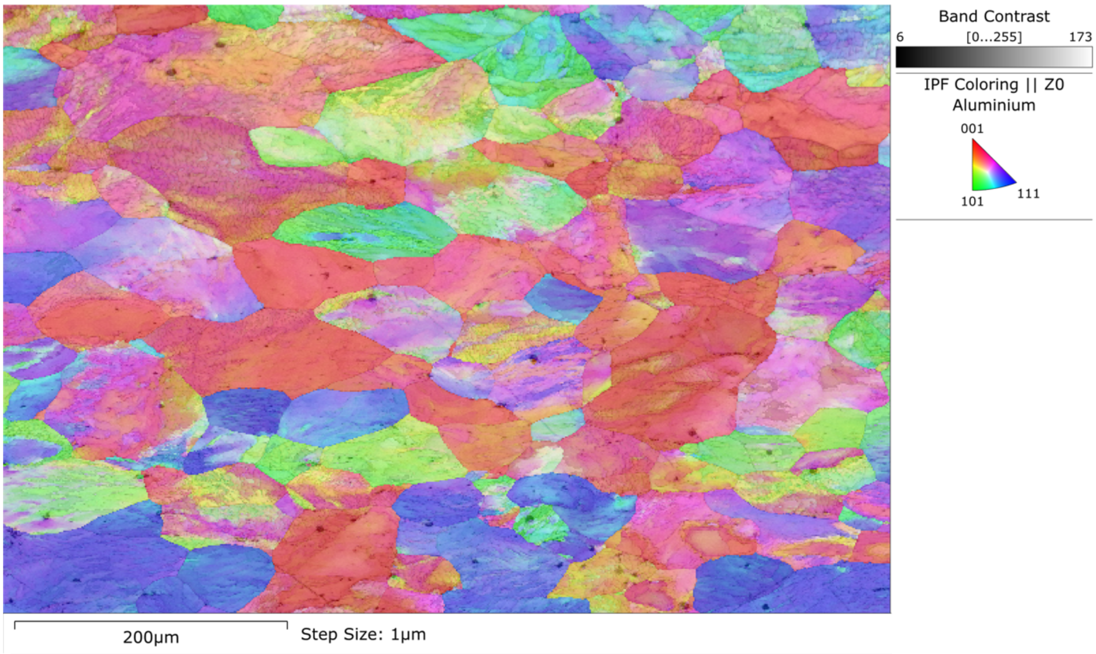

Figure 5.18 EBSD mapping of rolled Isogrid (as rolled - node section)

The grain orientations, pole figure and ODFs seen in Figure 5.18 and 19 confirm that the texture of the rolled Isogrid node samples is similar to the CNC annealed samples. The pole figure (Figure 5.19-A) and 0° ODF section (Figure 5.19-B) indicate the presence of the cube texture, which is standard in recrystallised rolled aluminium [5.57]. However, there is also a strong contour in the 0° ODF section (Figure 5.19-B) which represents a rotated cube texture. The presence of rotated cube texture and signs of deformation in the grain morphology indicate that this section has been subjected to shear modes of deformation [5.60,5.61].

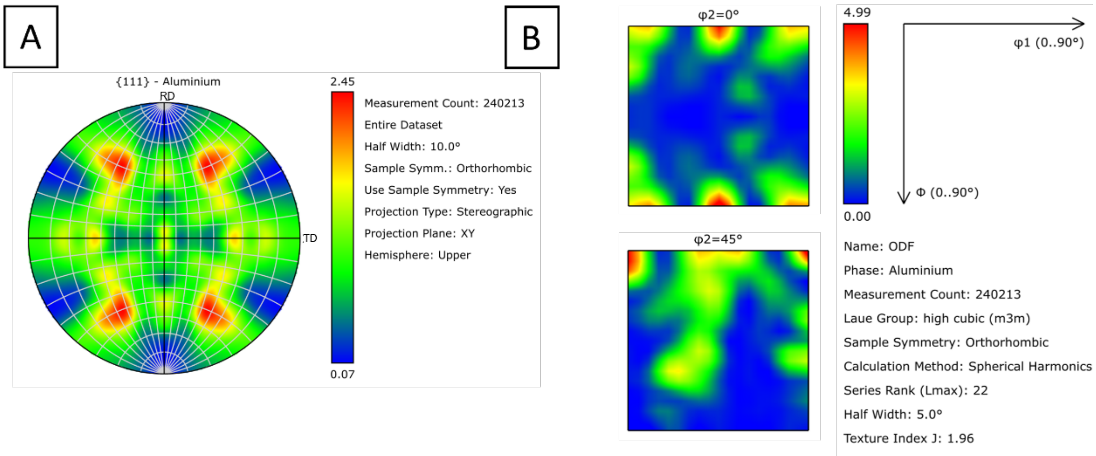

Figure 5.19 A – pole figure, B – relevant ODF sections for rolled Isogrid (node section)

Microhardness measurements of the rolled Isogrid (Figure 5.20) revealed variation in hardness throughout the cross-section. The highest hardness values were measure in the skin section (40-50Hv), followed by the rib (35-45Hv) and then the node section (31-43Hv). All areas of the cross section have been hardened when compared to the stock material, which had an initial hardness of 21Hv. These hardness values align very well with those reported by Bay et al. [5.13]. The skin section has undergone the most deformation and cold work, thereby hardening the most. The rib and node sections have therefore hardened less as they were subjected to varying lesser degrees of deformation. The acicular grains at the transition between skin and rib lattice as seen in Figure 5.14-C also exhibited higher hardness.

Figure 5.20 Microhardness map of rolled Isogrid

5.2.5 Rolled Isogrid post-annealing

Etched micrographs of rolled Isogrid after an annealing treatment are presented in Figure 5.21. These micrographs are similar to the annealed CNC samples, containing large grains with low aspect ratios. There are areas of coarser grains in the centre of the node and rib sections, whereas the skin sections have notably smaller grain structure. Figure 5.21-A shows the transition zone between node and skin sections. The microstructure is finer in this shoulder area where previously acicular grains had been created during the Isogrid rolling process. The level of grain refinement in this area after rolling created a zone with a greater density of nucleation sites during recrystallisation, leading to reduced grain size in the resultant recrystallised microstructure [5.62,5.63]. The node section as seen in Figure 5.21-B has much larger grains, as this area has been annealed once prior to rolling, lightly deformed, then annealed again, resulting in extensive grain growth. The skin section in Figure 5.21-C has a smaller grain structure in the same manner as the transition zone (Figure 5.21-A). In this micrograph there are also instances of larger grains bordered by smaller recrystallised grains in the same manner as the annealed CNC node in Figure 5.10, indicating areas of partial recrystallisation.

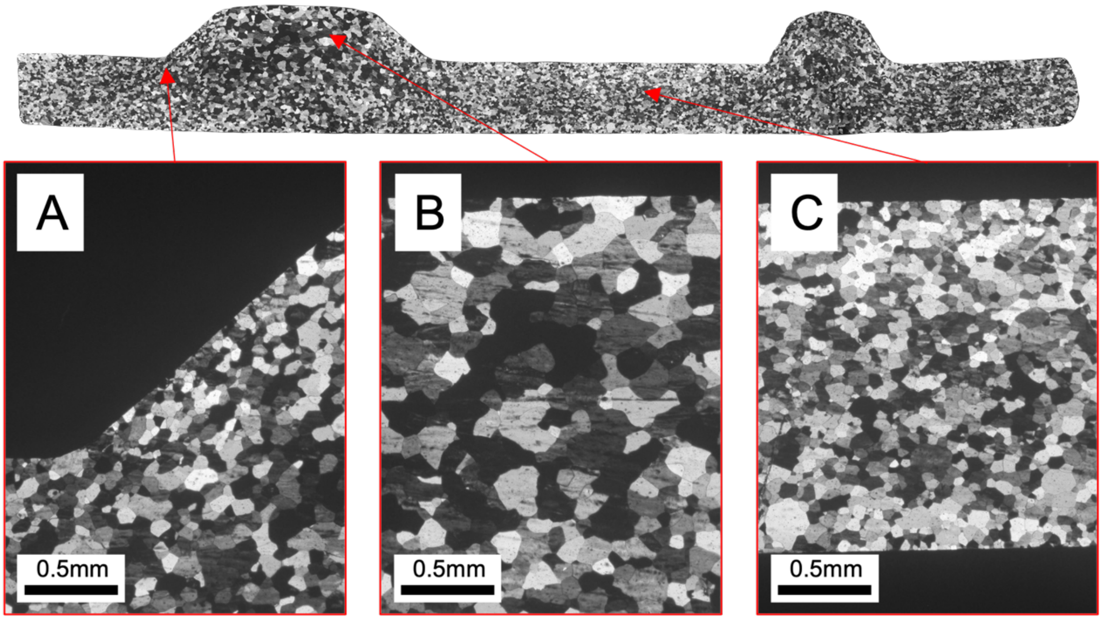

Figure 5.21 Etched micrographs of rolled Isogrid (annealed, x50 magnification): A – node-skin transition, B – node section, C – skin section

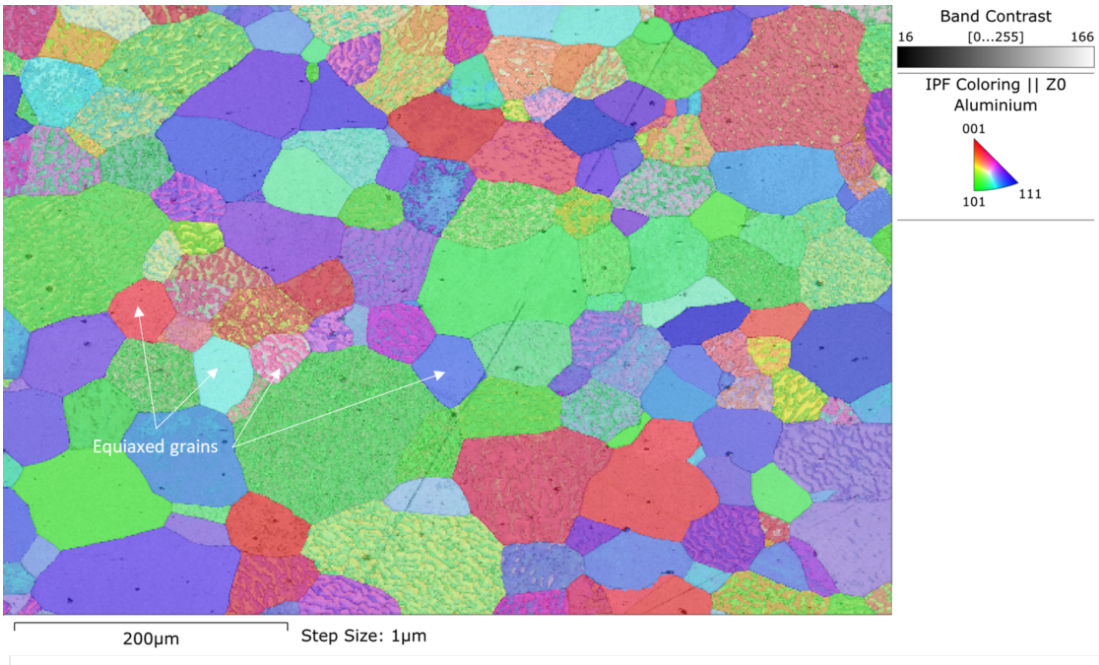

Figure 5.22 EBSD mapping of rolled Isogrid (annealed - skin section)

The EBSD grain map of the post-annealed rolled Isogrid skin section (Figure 5.22) is similar in appearance to Figure 5.11, as both microstructures have recrystallised through annealing. There is not a clearly dominant texture when reviewing the grain map alone. Equiaxed recrystallised grains can be seen forming at the boundaries between larger grains, further confirming partial recrystallisation [5.10,5.35]. The average grain size in this area is 20.0µm with an aspect ratio of 2.0 (see Table 5.1). The pole figure and 0° ODF section in Figure 5.23 show a Goss texture [5.43]. There are also faint intensity hotspots at the corners of the 0° ODF section which represent a cube texture[5.57]. These hotspots have moved off the true corners towards the centre of the slice, indicating a minor degree of rotation towards the rotated cube texture which is indicative of deformation via shear strain. The 45° ODF section has a contour in the bottom right corner which represents a brass texture [5.39]. These results are backed up by the literature, as a cube or Goss texture is expected after recrystallisation of AA1050 post-rolling [5.57].

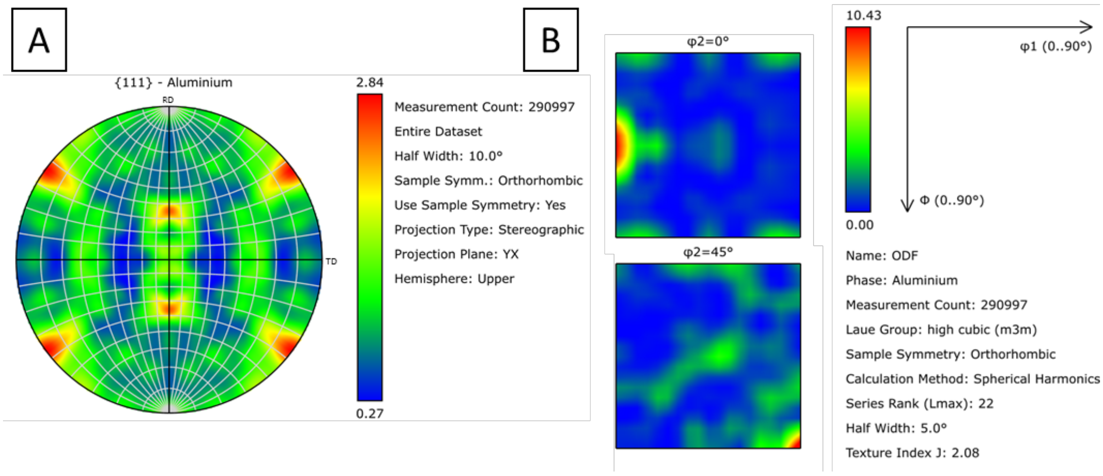

Figure 5.23 A – pole figure, B – relevant ODF sections for rolled Isogrid (annealed – skin section)

Microhardness measurements of the annealed rolled Isogrid (Figure 5.24) revealed a homogenous hardness distribution throughout the cross section between 15-23Hv. These were also consistent with the literature [5.13], although slightly lower than the annealed CNC samples.

Figure 5.24 Microhardness map of rolled Isogrid in post-annealed condition

Table 5.1 summarises the results reported throughout this chapter, to facilitate comparisons and discussion.

Table 5.1 Summary of microstructural findings

Sample		Grain size (µm)	Aspect ratio	Hardness (Hv)	Elements of texture
CNC	Skin	13.7	6.4	40-55	Copper dominant
	Node	9.8	4.3	40-55	Goss, brass, copper
	Annealed	35.8	2.4	15-27	Cube, Goss, brass
Rolled	Skin	13.4	3.2	40-50	Copper dominant Shear textures present (rotated cube)
	Node	22.6	2.4	31-43	Cube and rotated cube
	Annealed	20	2.0	15-23	Goss dominant Brass and cube present

5.3 Discussion

Initial investigation of the stock material provided the baseline microstructure for AA1050 in its rolled and annealed states. In its H14 condition, the microstructure is acicular throughout, exhibiting high aspect ratios after uni-axial elongation in the roll direction with individual grains displaying an inhomogeneously deformed appearance. This is in stark contrast to the recrystallised grains in the annealed condition which are equiaxed and appear homogeneous. These findings are well supported by the literature on the cold rolling of AA1050 [5.13,5.22–5.24,5.31,5.53].

The EBSD analysis of CNC milled Isogrid provided further information about the H14 rolling process, as the milling process generated no significant changes to the original H14 microstructure. These results therefore also apply to the microstructure in Figure 5.3-A and Figure 5.4. The aspect ratio of grains found within the skin section of the CNC milled Isogrid is 48% higher than those found in the node section, which is an indication of the increased deformation experienced by the material closer to the surfaces of the billet during the rolling process. Likewise, the intensity of the copper texture in the ODF of the skin section (Figure 5.8) is 409% greater than that of the textures at the node (Figure 5.6). These trends agree with the work of Hallberg et al. [5.53] which found increased cold work near the surfaces of cold-rolled AA1050.

Variation in microstructure through rolled Isogrid samples was observed as a consequence of the different levels of deformation required to achieve the target geometry in the Isogrid rolling process. The grains of the rolled Isogrid's skin section were 40% smaller than those of the node section and of a 33% higher aspect ratio. This is evidence that the skin section of the rolled Isogrid has undergone more cold work resulting in greater grain refinement than the node section. Such a result, paired with the microhardness map of rolled Isogrid (Figure 5.20), indicates that areas of increased hardness correlate with areas of greater deformation. Further, the grains of the 0° rib directions exhibited elongation in the roll direction, whereas the grains in the ±60° rib directions remained equiaxed. This is due to the topological differences between the annular and helical grooves on the Isogrid roller used to form the 0° rib and ±60° ribs, respectively. The annular grooves mimic a standard rolling process with a reduced diameter, allowing the 0° ribs to elongate and develop acicular grain morphology. The helical grooves do not allow the same degree of elongation in the roll direction, which accounts for the reduced cold work and microstructural evolution seen in the ±60° ribs. The variation in hardness throughout the rolled Isogrid cross-section and difference in grain structure between 0° and ±60° ribs was considered as a potential source of anisotropic behaviour in the rolled Isogrid for both in-plane and out of plane mechanical properties; however this was not found to be the case as seen in Chapter 6.

The copper, brass and Goss textures found throughout the CNC milled Isogrid are the standard microstructural textures expected from rolled AA1050 [5.15,5.21,5.22,5.39]. In addition to these standard deformation textures, the Isogrid rolling process produced a degree of shear deformation texture [5.60,5.61]. Standard rolling textures such as copper and brass are produced when FCC materials are subjected to plane strain deformation [5.15,5.22]. The rotated cube texture seen in the rolled Isogrid node section is unusual as a rolling texture; however, the pre-rolling annealing treatment of the billet material created a cube texture throughout the centre of the billet as seen in the annealed CNC Isogrid samples and throughout the literature [5.8,5.57]. This texture has been rotated during Isogrid rolling, which further supports the existence of shear forces in the roll gap. Similar evidence of shear forces required to support such a result can be found in the literature concerning asymmetrical rolling processes [5.23,5.36,5.38,5.64]. The Isogrid rolling process must also be considered asymmetrical, given the difference in geometry between the rollers and the evidence of asymmetrical shear textures. The inclusion of shear deformation textures within rolled Isogrid samples indicates that the Isogrid rolling process requires a more complex model of the forces present in the roll gap than the existing plane strain simplifications for flat rolling. The design of the Isogrid roller includes helical grooves with an axial directional component to create the ±60° ribs. Any deformation in the axial or transverse rolling direction due to these grooves disrupts the standard plane strain model of forces in the roll gap.

The microhardness values of the annealed samples approached the lower limit of hardness possible for AA1050, indicating successful elimination of prior cold work [5.13]. The post-annealing rolled Isogrid was slightly softer than the CNC annealed; however, the billets were annealed once in preparation for Isogrid rolling, then a second time after the Isogrid rolling process. This effectively increases the total time it experienced for recrystallisation and grain growth. The CNC milled Isogrid sample in the H14 state was harder than the Isogrid rolled sample by 10-20Hv and relatively homogeneous throughout due to the extensive grain refinement and cold work, as seen in Figure 5.4. The rolled Isogrid sample exhibited areas of higher and lower hardness corresponding to the level of deformation experienced in each.

EBSD analysis determined that the texture imparted into the grain structure of the rolled Isogrid was less pronounced than that of the AA1050 in its H14 condition. The rolled Isogrid pole figures show less intense deformation textures in both the skin and node locations. This result is aligned with the microhardness maps which show the CNC Isogrid to be harder throughout the cross section. The lower hardness and reduced deformation texture intensity seen in the rolled Isogrid samples implies that a greater level of deformation in Isogrid rolling may be feasible, facilitating the production of rolled geometries with higher rib to skin ratios, hence improved mechanical properties.

5.4 Conclusions

1. Isogrid rolling produced a cold-worked grain structure containing mostly standard rolling deformation textures indicative of plane strain with the inclusion of shear deformation textures. Due to these shear deformation textures, the Isogrid rolling process must be considered as an asymmetrical 3D technique and the standard simplified plane strain model of rolling is not suitable as a method of analysis.
2. The microstructure of rolled Isogrid is aligned parallel to the outer contour of its cross section, as opposed to CNC milled Isogrid which has an interrupted microstructure at the milled face. This improved the strength of the rolled Isogrid structure, as will be discussed in Chapter 6.
3. Rolled Isogrid developed variation in the cold work and directionality of its grain structure during the rolling process. The skin section displayed considerably more evidence of cold work than the rib lattice and a corresponding difference in hardness was observed. The ribs in the 0° rolling direction exhibited elongated grains unlike the equiaxed structure seen in the ±60° direction ribs.
4. The high intensity and homogeneity of the deformation textures seen in the CNC milled Isogrid contributes to a higher level of anisotropy in the resultant mechanical properties of the CNC milled Isogrid samples (as will be seen in Chapter 6).
5. The Isogrid rolling process has not deformed the AA1050 microstructure to the same degree as the H14 rolling to half hardness process, which was conducted on the CNC milling stock material.

The evaluation of mechanical properties of rolled and CNC Isogrid will further elucidate the differences between the two manufacturing methods and determine whether the microstructural conclusions drawn from this work influence the potential utility of the Isogrid rolling process.

5.5 *Reference List*

[5.1] Callister WD. Wiley: Materials Science and Engineering: An Introduction, 8th Edition - William D. Callister, David G. Rethwisch. 2010.

[5.2] Lopes AB, Barlat F, Gracio JJ, Ferreira Duarte JF, Rauch EF. Effect of texture and microstructure on strain hardening anisotropy for aluminum deformed in uniaxial tension and simple shear. Int J Plast 2003;19:1–22. https://doi.org/10.1016/S0749-6419(01)00016-X.

[5.3] Soliman MS, El-Danaf EA, Almajid AA. Enhancement of static and fatigue strength of 1050 Al processed by equal-channel angular pressing using two routes. Materials Science and Engineering A 2012;532:120–9. https://doi.org/10.1016/j.msea.2011.10.072.

[5.4] Abdulstaar MA, Mhaede M, Wollmann M, Wagner L. Fatigue behaviour of commercially pure aluminium processed by rotary swaging. J Mater Sci 2014;49:1138–43. https://doi.org/10.1007/s10853-013-7792-9.

[5.5] Yu Q, Mishra RK, Morris JW, Minor AM. The effect of size on dislocation cell formation and strain hardening in aluminium. Philosophical Magazine 2014;94:2062–71. https://doi.org/10.1080/14786435.2014.906755.

[5.6] Wei YL, Godfrey A, Liu W, Liu Q, Huang X, Hansen N, et al. Dislocations, boundaries and slip systems in cube grains of rolled aluminium. Scr Mater 2011;65:355–8. https://doi.org/10.1016/j.scriptamat.2011.05.005.

[5.7] Lenard JG. Primer on Flat Rolling. 2007. https://doi.org/10.1016/B978-0-08-045319-4.X5000-1.

[5.8] Ahlborn H, Hornbogen E, Köster U. Recrystallisation mechanism and annealing texture in aluminium-copper alloys. J Mater Sci 1969;4:944–50. https://doi.org/10.1007/BF00555308.

[5.9] Simões FJP, de Sousa RJA, Grácio JJA, Barlat F, Yoon JW. Mechanical behavior of an asymmetrically rolled and annealed 1050-O heet. Int J Mech Sci 2008;50:1372–80. https://doi.org/10.1016/j.ijmecsci.2008.07.009.

[5.10] Helbert AL, Wang W, Brisset F, Baudin T, Penelle R. In situ EBSD investigation of recrystallization in a partially annealed and cold-rolled aluminum alloy of commercial purity. Adv Eng Mater 2012;14:39–44. https://doi.org/10.1002/adem.201100165.

[5.11] Kim GH, Nam SK, Lee DN, Kim I. A process for increasing plastic strain ratio of AA1050 Al alloy sheet. International Journal of Materials and Product Technology 2017;54:202–11. https://doi.org/10.1504/IJMPT.2017.080559.

[5.12] Atifeh SM, Rouzbeh A, Hashemi R, Sedighi M. Effect of annealing on formability and mechanical properties of AA1050/Mg-AZ31B bilayer sheets fabricated by explosive welding method. International Journal of Advanced Manufacturing Technology 2022;118:775–84. https://doi.org/10.1007/s00170-021-07999-z.

[5.13] Bay N. Cold forming of aluminium-state of the art 2000;71:76–90.

[5.14] Dillamore IL, Butler E, Green D. Crystal Rotations under Conditions of Imposed Strain and the Influence of Twinning and Cross-Slip. Metal Science Journal 1968;2:161–7. https://doi.org/10.1179/030634568790443512.

[5.15] Dillamore IL, Roberts WT. Rolling textures in f.c.c. and b.c.c. metals. Acta Metallurgica 1964;12:281–93. https://doi.org/10.1016/0001-6160(64)90204-4.

[5.16] Dillamore IL, Smallman RE. The stacking-fault energy of F.C.C. metals. Philosophical Magazine 1965;12:191–3. https://doi.org/10.1080/14786436508224959.

[5.17] Schulthess TC, Turchi PEA, Gonis A. Systematic study of stacking fault energies of random Al-based alloys. Acta Mater 1998;46:2215–21. https://doi.org/10.1016/S1359-6454(97)00432-1.

[5.18] Muzyk M, Pakiela Z, Kurzydlowski KJ. Ab initio calculations of the generalized stacking fault energy in aluminium alloys. Scr Mater 2011;64:916–8. https://doi.org/10.1016/j.scriptamat.2011.01.034.

[5.19] Humphreys FJ, Hatherly M. Deformation Textures. Recrystallization and Related Annealing Phenomena 2004:67–89. https://doi.org/10.1016/b978-008044164-1/50007-4.

[5.20] Haldar A, Suwas S, Bhattacharjee D. Microstructure and Texture in Steels and other Materials. 2008.

[5.21] Hirsch J. Textures in industrial processes and products. Materials Science Forum 2012;702–703:18–25. https://doi.org/10.4028/www.scientific.net/MSF.702-703.18.

[5.22] Hirsch J. Texture evolution during rolling of aluminium alloys. TMS Light Metals 2008:1071–7.

[5.23] Lee JK, Lee DN. Texture control and grain refinement of AA1050 Al alloy sheets by asymmetric rolling. Int J Mech Sci 2008;50:869–87. https://doi.org/10.1016/j.ijmecsci.2007.09.008.

[5.24] Bay B, Hansen N, Kuhlmann-Wilsdorf D. Microstructural evolution in rolled aluminium. Materials Science and Engineering A 1992;158:139–46. https://doi.org/10.1016/0921-5093(92)90002-I.

[5.25] Lenard J. Flat Rolling - A General Discussion. Primer on Flat Rolling: Second Edition, Elsevier Inc.; 2014, p. 39–55. https://doi.org/10.1016/B978-0-08-099418-5.00004-4.

[5.26] Malinowski Z, Pietrzyk M, Lenard JG. Analysis of the flat-rolling process: one-dimensional and finite-element models. Journal of Materials Processing Tech 1993;39:373–87. https://doi.org/10.1016/0924-0136(93)90170-B.

[5.27] Barata Marques MJM, Martins PAF. A solution to plane strain rolling by the weighted residuals method. Int J Mech Sci 1990;32:817–27. https://doi.org/10.1016/0020-7403(90)90161-B.

[5.28] Hajizadeh K, Ejtemaei S, Eghbali B. Microstructure, hardness homogeneity, and tensile properties of 1050 aluminum processed by constrained groove pressing. Appl Phys A Mater Sci Process 2017;123:1–9. https://doi.org/10.1007/s00339-017-1123-y.

[5.29] Hughes DA, Hansen N, Bammann DJ. Geometrically necessary boundaries, incidental dislocation boundaries and geometrically necessary dislocations. Scr Mater 2003;48:147–53. https://doi.org/10.1016/S1359-6462(02)00358-5.

[5.30] Dillamore IL, Roberts WT. PREFERRED ORIENTATION IN WROUGHT AND ANNEALED METALS 1965;10.

[5.31] Wang R, Lu C. Dependence of microstructure evolution on rolling conditions in AA1050 aluminum alloy. J Phys Conf Ser 2021;2020. https://doi.org/10.1088/1742-6596/2020/1/012011.

[5.32] Zaidi MA, Sheppard T. Development of microstructure throughout roll gap during rolling of aluminium alloys. Metal Science 1982;16:229–38. https://doi.org/10.1179/030634582790427334.

[5.33] Bunge HJ. Texture Analysis in Materials Science. 1969. https://doi.org/10.1201/9781003068426-9.

[5.34] Alvi MH, Cheong SW, Suni JP, Weiland H, Rollett AD. Cube texture in hot-rolled aluminum alloy 1050 (AA1050)-nucleation and growth behavior. Acta Mater 2008;56:3098–108. https://doi.org/10.1016/j.actamat.2008.02.037.

[5.35] Wang W, Helbert AL, Baudin T, Brisset F, Penelle R. Reinforcement of the Cube texture during recrystallization of a 1050 aluminum alloy partially recrystallized and 10% cold-rolled. Mater Charact 2012;64:1–7. https://doi.org/10.1016/j.matchar.2011.11.008.

[5.36] Knight CW, Hardy SJ, Lees AW, Brown KJ. Investigations into the influence of asymmetric factors and rolling parameters on strip curvature during hot rolling. J Mater Process Technol 2003;134:180–9. https://doi.org/10.1016/S0924-0136(02)00469-7.

[5.37] Bedair OK, Troitsky MS. A study of the fundamental frequency characteristics of eccentrically and concentrically simply supported stiffened plates. Int J Mech Sci 1997;39:1257–72. https://doi.org/10.1016/s0020-7403(97)00016-7.

[5.38] Knight CW, Hardy SJ, Lees AW, Brown KJ. Influence of roll speed mismatch on strip curvature during the roughing stages of a hot rolling mill. J Mater Process Technol 2005;168:184–8. https://doi.org/10.1016/j.jmatprotec.2004.09.094.

[5.39] Leffers T, Ray RK. The brass-type texture and its deviation from the copper-type texture. Prog Mater Sci 2009;54:351–96. https://doi.org/10.1016/j.pmatsci.2008.09.002.

[5.40] Alvi MH, Cheong S, Weiland H, Rollett AD. Microstructural evolution during recrystallization in hot rolled aluminum alloy 1050. Metallurgical Modeling for Aluminum Alloys - Proceedings from Materials Solutions Conference 2003: 1st International Symposium on Metallurgical Modeling for Aluminum Alloys 2003:191–7.

[5.41] Tambunan AF, Angela I, Basori I, Sofyan BT. Effect of cold rolling and annealing temperature on the characteristics of Cu-28Zn-1.1Bi alloy produced by gravity casting. Materials Science Forum 2018;939:73–80. https://doi.org/10.4028/www.scientific.net/MSF.939.73.

[5.42] Tomé CN, Necker CT, Lebensohn RA. Mechanical anisotropy and grain interaction in recrystallized aluminum. Metall Mater Trans A Phys Metall Mater Sci 2002;33:2635–48. https://doi.org/10.1007/s11661-002-0385-x.

[5.43] Moghaddam M, Zarei-Hanzaki A, Pishbin MH, Shafieizad AH, Oliveira VB. Characterization of the microstructure, texture and mechanical properties of 7075 aluminum alloy in early stage of severe plastic deformation. Mater Charact 2016;119:137–47. https://doi.org/10.1016/j.matchar.2016.07.026.

[5.44] Lee JC, Seok HK, Suh JY. Microstructural evolutions of the Al strip prepared by cold rolling and continuous equal channel angular pressing. Acta Mater 2002;50:4005–19. https://doi.org/10.1016/S1359-6454(02)00200-8.

[5.45] El-Danaf EA. Mechanical properties, microstructure and texture of single pass equal channel angular pressed 1050, 5083, 6082 and 7010 aluminum alloys with different dies. Mater Des 2011;32:3838–53. https://doi.org/10.1016/j.matdes.2011.03.006.

[5.46] Jiang J, Ding Y, Zuo F, Shan A. Mechanical properties and microstructures of ultrafine-grained pure aluminum by asymmetric rolling. Scr Mater 2009;60:905–8. https://doi.org/10.1016/j.scriptamat.2009.02.016.

[5.47] Allwood JM, Shouler DR. Generalised forming limit diagrams showing increased forming limits with non-planar stress states. Int J Plast 2009;25:1207–30. https://doi.org/10.1016/j.ijplas.2008.11.001.

[5.48] Gotoh M, Taehoon C, Iwata N. Effect of Out-of-Plane Stress on the Forming Limit Strain of Sheet Metals. JSME International Journal 1995;38:123–32.

[5.49] Allwood JM, Shouler DR. Paddle forming: a novel class of sheet metal forming processes. CIRP Ann Manuf Technol 2007;56:257–60. https://doi.org/10.1016/j.cirp.2007.05.060.

[5.50] Allwood JM, Shouler DR, Tekkaya AE. The Increased Forming Limits of Incremental Sheet Forming Processes. Key Eng Mater 2007;344:621–8. https://doi.org/10.4028/www.scientific.net/kem.344.621.

[5.51] Besong LI, Buhl J, Bambach M. Investigations on hole-flanging by paddle forming and a comparison with single point incremental forming. Int J Mech Sci 2019;164:105143. https://doi.org/10.1016/j.ijmecsci.2019.105143.

[5.52] ASM Handbook Committee. ASM Handbook Volume 2: Properties and Selection: Nonferrous Alloys and Special-Purpose Materials. ASM International; 1990.

[5.53] Hallberg H. Influence of process parameters on grain refinement in AA1050 aluminum during cold rolling. Int J Mech Sci 2013;66:260–72. https://doi.org/10.1016/j.ijmecsci.2012.11.016.

[5.54] Fabiana Meijon Fadul. The Beilby Layer. Sci Prog 2019;31:609–25.

[5.55] Scamans GM, Frolish MF, Rainforth WM, Zhou Z, Liu Y, Zhouc X, et al. The ubiquitous beilby layer on aluminium surfaces. Surface and Interface Analysis 2010;42:175–9. https://doi.org/10.1002/sia.3204.

[5.56] Finch GI. The Beilby layer on non-metals [2]. Nature 1936;138:1010. https://doi.org/10.1038/1381010a0.

[5.57] Hjelen J, Orsund R, Nes E. OVERVIEW NO. 93 ON THE ORIGIN OF RECRYSTALLIZATION TEXTURES IN ALUMINIUM. Acta Metallurgica Et Materialia 1991;39:1377–404.

[5.58] Chakravarty P, Pál G, Sidor JJ. The dependency of work hardening on dislocation statistics in cold rolled 1050 aluminum alloy. Mater Charact 2022;191. https://doi.org/10.1016/j.matchar.2022.112166.

[5.59] Sidor JJ, Chakravarty P, Bátorfi JG, Nagy P, Xie Q, Gubicza J. Assessment of dislocation density by various techniques in cold rolled 1050 aluminum alloy. Metals (Basel) 2021;11:1–16. https://doi.org/10.3390/met11101571.

[5.60] Yousefi Mehr V, Toroghinejad MR, Rezaeian A, Asgari H, Szpunar JA. A texture study of nanostructured Al–Cu multi-layered composite manufactured via the accumulative roll bonding (ARB). Journal of Materials Research and Technology 2021;14:2909–19. https://doi.org/10.1016/j.jmrt.2021.08.054.

[5.61] Lee JK, Lee DN. Texture control and grain refinement of AA1050 Al alloy sheets by asymmetric rolling. Int J Mech Sci 2008;50:869–87. https://doi.org/10.1016/j.ijmecsci.2007.09.008.

[5.62] Jones AR, Ralph B, Hansen N. Subgrain coalescence and the nucleation of recrystallization at grain boundaries in aluminium. vol. 368. 1979. https://doi.org/https://doi.org/10.1098/rspa.1979.0134.

[5.63] Engler O. Nucleation and growth during recrystallisation of aluminium alloys investigated by local texture analysis. Materials Science and Technology 1996;12:859–72. https://doi.org/10.1179/mst.1996.12.10.859.

[5.64] ZUO F qing, JIANG J hua, SHAN A dang, FANG J min, ZHANG X yao. Shear deformation and grain refinement in pure Al by asymmetric rolling. Transactions of Nonferrous Metals Society of China (English Edition) 2008;18:774–7. https://doi.org/10.1016/S1003-6326(08)60133-8.

6 Mechanical characterisation of rolled and CNC milled Isogrid

6.1 Mechanical behaviour of Isogrid

Isogrid was developed to have very specific, mass optimal out-of-plane mechanical properties as a lightweight material structure for aerospace applications [6.1–6.4]. The structure mimics the in-plane properties of sheet metal, while offering superior resistance for out of plane loading regimes such as bending or torsion. These key features of Isogrid were described in Meyer et al. [6.1] as follows:

"*Characteristics:*

- *Isotropic (no directions of instability or weakness)*
- *Poisson's ratio 1/3*
- *Efficient in compression and bending*

Advantages:

- *Easily analysed*
- *Can be optimized for wide range of loading intensities*
- *Standard pattern for attachment (nodes accommodate equipment mounting without change)*
- *Readily reinforced for concentrated loads and cut-outs*
- *Redundant load paths*
- *Less structural depth*"

Isotropy is characterised by the even distribution of properties in all directions within a material [6.5]. Isogrid is generally regarded as isotropic because the equilateral triangular arrangement of ribs within the rib lattice creates a near uniform field of mechanical properties in all directions [6.1,6.6,6.7]. Therefore, the response of Isogrid to loading is independent of rib orientation and of the face on which the load is applied. However, this is a simplification and the mechanical isotropy of Isogrid is restricted to its elastic behaviour [6.6–6.9]. Isogrid cannot be called a true isotropic material as out-of-plane and failure modes of Isogrid have been shown to exhibit anisotropic behaviour. Thus, it is described in some sources as quasi-isotropic [6.6–6.8,6.10–6.12]. Intentional deviation from the aim of isotropic geometries resulted in the development of anisogrid structures which gained popularity for their increased strength and manufacturability in composite materials [6.9,6.13–6.21].

Isotropic properties are desirable, as the entire structure can be simplified for analysis and design [6.1–6.4,6.22,6.23]. Using the smeared stiffener method [6.1,6.24,6.25], the entire Isogrid structure can be represented by a uniform shell with the same properties, known as an equivalent thickness shell [6.1,6.24,6.25]. The equivalent thickness shell can then be used in place of Isogrid structures for finite element analyses and structural calculations. This ease of analysis was important enough to be listed as the primary advantage of Isogrid within the summary given in the Isogrid design handbook [6.1].

The handbook [6.1] reports an idealised value of Poisson's ratio calculated using the smeared stiffener method: $\nu=0.33$. This is close to the standard assumption of $\nu=0.3$ for an isotropic material during elastic or ductile deformation [6.26]. When applying a load to Isogrid, the lattice acts like a truss structure, distributing loads in tension and compression to the ribs according to their orientation [6.1,6.6,6.53]. The statically determinate nature of the equilateral triangular lattice greatly reduces internal lattice rotation, which was seen as a shortcoming of Isogrid's predecessor, Orthogrid [6.1]. Static indeterminacy and internal rotation of the lattice structure has a profound effect on the deformation modes of a structure, therefore on its isotropy/Poisson's ratio. Recent research on lattice structures has exploited this phenomenon and designed lattice structures with internal rotation to develop structures with customisable Poisson's ratios and auxetic behaviour (Poisson's ratio<0) [6.26,6.27].

Isogrid is designed to be mass efficient for out of plane loading regimes [6.1,6.4,6.22,6.23]. As such, an ideal Isogrid structure is typified by a low-density rib lattice with a tall section height, resulting in a high second moment of area to resist bending loads [6.1]. The location of the neutral axis in bending can be changed by altering the geometric parameters of the structure [6.1]. Isogrid is particularly efficient in bending when the neutral axis sits within the rib lattice at some distance away from its skin, as this minimises the unloaded area of the cross section [6.1,6.22]. The same principle led to the development of low-density core sandwich panels, which place the higher density load resisting elements of their structures at a distance from the neutral axis [6.10,6.28–6.34]. Within a case study of an optimised Isogrid geometry [6.1], the bending stiffness was found to increase by a factor of 192 while the extensional stiffness increased by only a factor of 4/3. For this reason, it would be fair to state that while Isogrid offers excellent improvement in bending stiffness via shape factor, the difference in extensional stiffness approaches unity for most geometries.

Isogrid is described throughout the literature as damage resistant or damage resilient, as loading from a failed part of the structure can be rerouted throughout the lattice [6.35–6.40]. This is particularly well described in the report by Pettit et al. [6.40], which describes how integrally stiffened structures, such as Isogrid, arrest and reorient cracks at the base of their stiffeners. The long term damage resistant nature of Isogrid is less important to its usage within launch vehicles as they have typically been required for a single launch throughout their history; however, containment of cracks and resistance to fatigue are a highly desirable property for other applications such as aerospace design [6.41–6.44].

6.2 Results

A combination of tensile and bending tests were performed as per section 3.5 to evaluate and compare the mechanical properties of rolled Isogrid, CNC milled Isogrid and rolling billet material. Full U bending tests were performed on rolled Isogrid and on the 3mm billets to measure the influence of shape factor on bending strength. These bending tests were performed on samples oriented with “ribs up” and “ribs down” within the bending test apparatus to explore the isotropy of rolled and CNC milled Isogrid in the thickness direction. To isolate the effects of shape, these tests were performed on all samples in their cold worked condition as well as in their annealed condition. Tensile tests and full U bending tests were performed on the next iteration of rolled Isogrid from the 4mm stock and compared with CNC milled Isogrid. These experiments were performed at 0° and 90° to the primary rib direction of each sample type to assess the in-plane isotropy of the rolled Isogrid and CNC milled Isogrid. As before, these tests were conducted in both the cold worked condition and the annealed condition. The geometric markers on the lines throughout the presented graphs provide differentiation in grey scale, and do not represent data points.

6.3 *Tensile behaviour of Rolled and CNC milled Isogrid*

The data from the tensile tests of rolled and CNC milled Isogrid is presented in Figure 6.1. The rolled Isogrid experienced an increase in tensile strength of 13.7% (Figure 6.1-A) when compared to the CNC milled Isogrid. This reduced to an 8.8% increase (Figure 6.1-B) when both sets of samples were annealed. The rolled Isogrid exhibited higher ductility than the CNC milled Isogrid in tension when both samples were tested in their as produced state, as demonstrated by the higher strains achieved before failure in Figure 6.1.

Figure 6.2 shows the tensile behaviour of rolled and CNC milled Isogrid in the 0° and 90° orientations, for sample groups which were not annealed. Both rolled and CNC milled Isogrid exhibited an isotropic response during the elastic portion of the test, as both orientations within the sample groups performed identically. The rolled Isogrid showed a 3.5% (Figure 6.2-A) increase in tensile strength in the 90° direction (the applied force was perpendicular to the roll direction). The CNC milled Isogrid showed the same trend by 11.1% (Figure 6.2-B) under the same conditions. While the samples tested in the 90° direction showed higher tensile strength, they also displayed lower ductility and approached failure at lower strain values. The performance gap between the orientations of rolled Isogrid diverged early in the elastic region (Figure 6.2-C). The CNC milled Isogrid exhibited a greater difference in tensile strength between the 0° and 90° orientations, but the stress strain curves of the two sample directions remained identical for more of the elastic region (Figure 6.2-D).

The SEM micrographs of the tensile fracture surfaces in Figure 6.3 show all variations of the Isogrid samples with a dimpled texture on the resultant fracture surface. The dimpled surface morphology of each micrograph is evidence that all the sample groups fractured in a ductile manner.

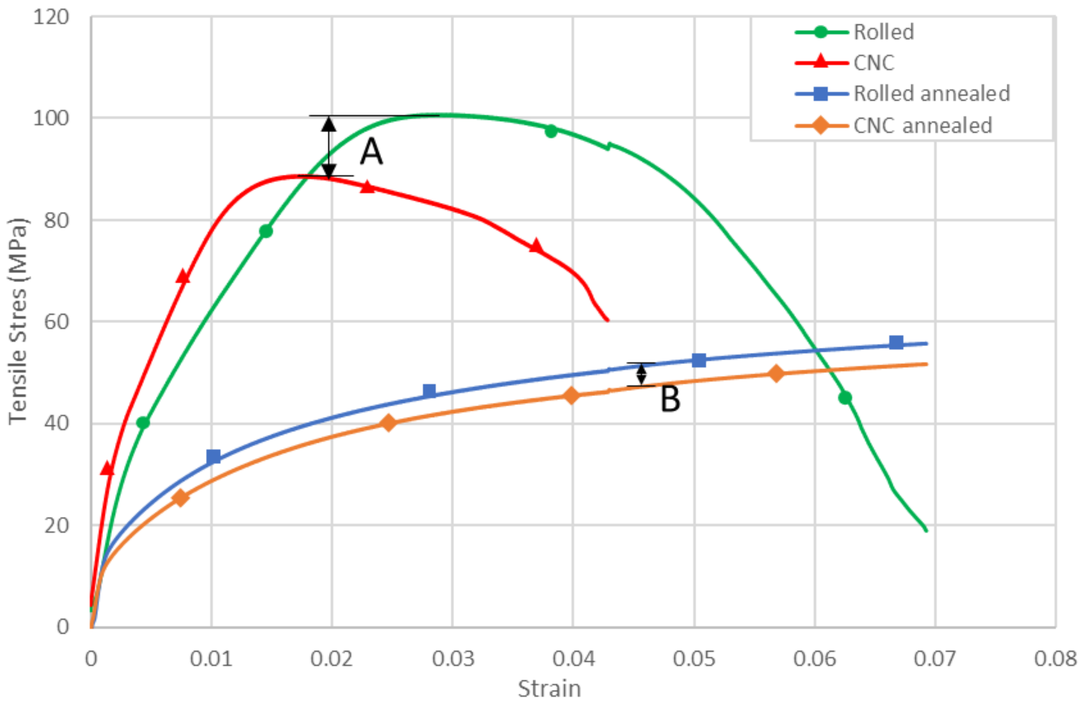

Figure 6.1 Comparison of rolled Isogrid vs CNC milled Isogrid's tensile behaviour

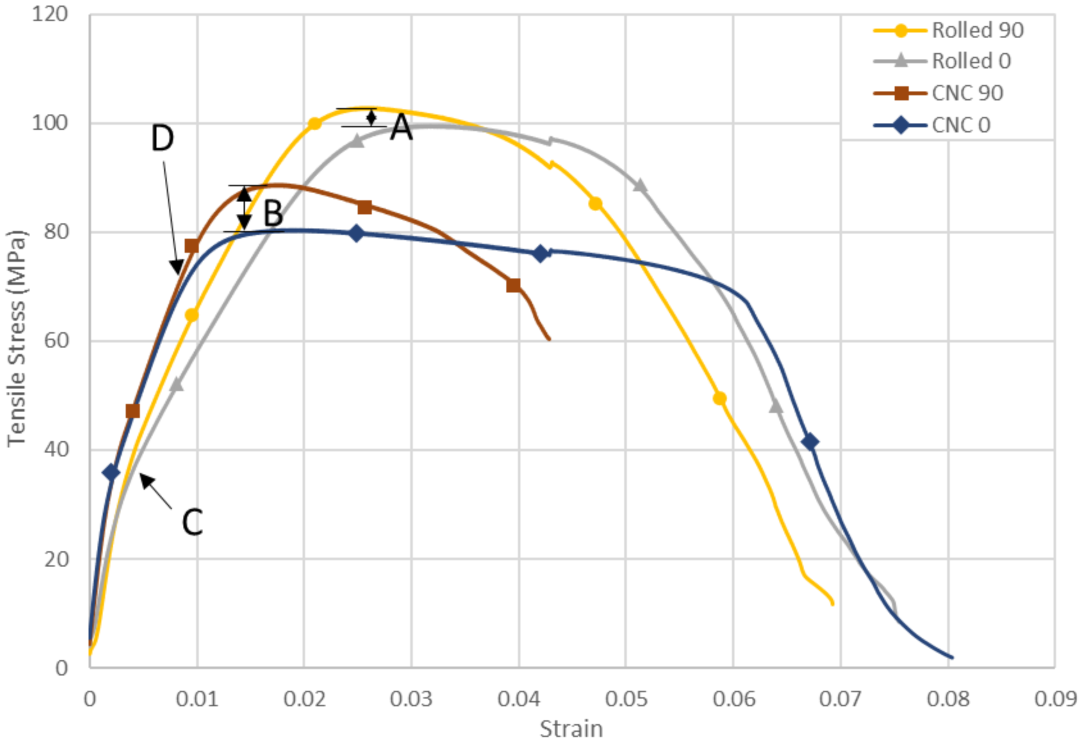

Figure 6.2 Comparison of Tensile behaviour between 0° and 90° samples of rolled Isogrid and CNC milled Isogrid

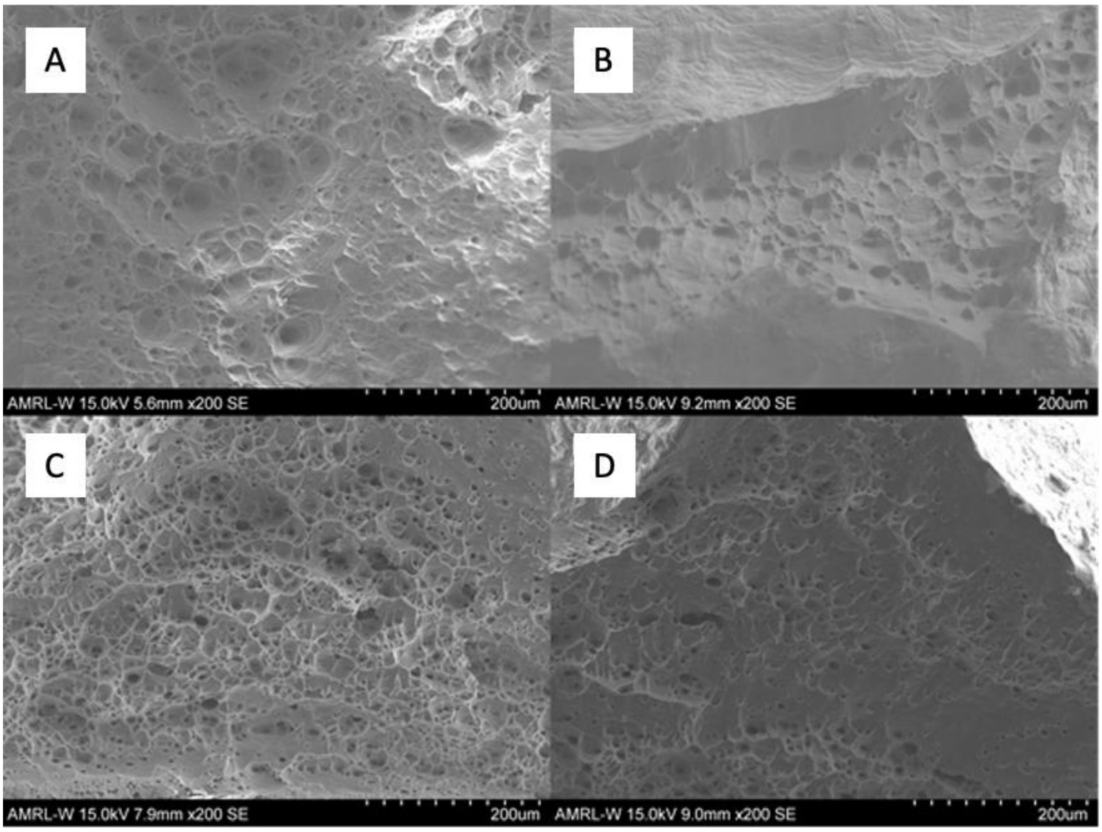

Figure 6.3 SEM micrographs of tensile fracture surfaces. x200X magnification (A-rolled, B-rolled & annealed, C-CNC milled, D-CNC milled & annealed)

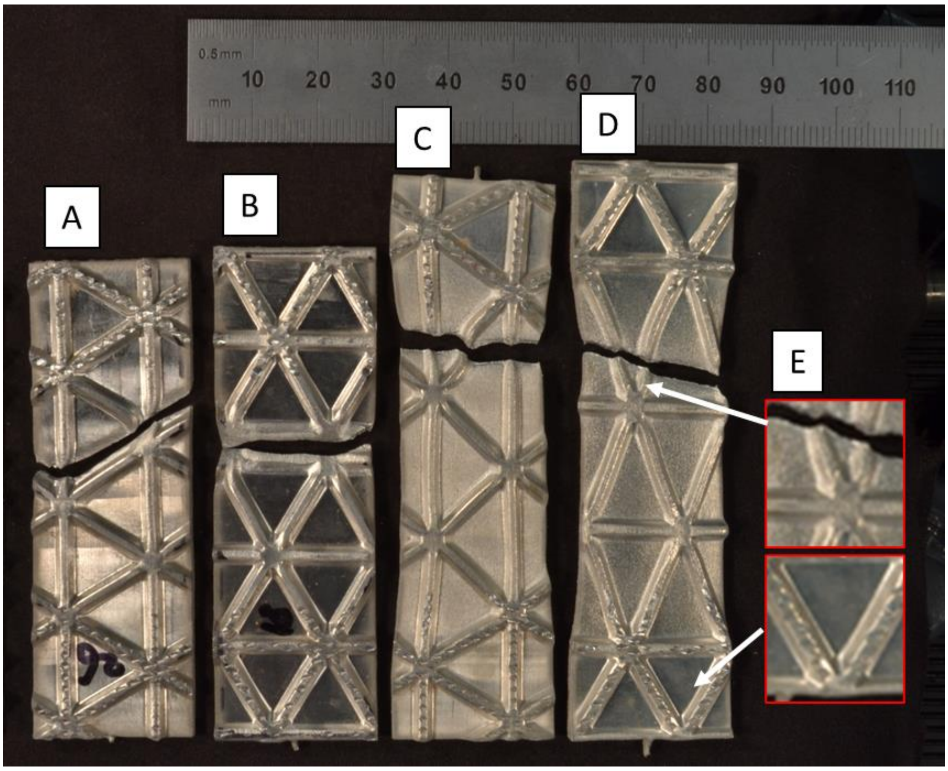

Figure 6.4 Rolled specimens after tensile testing, A- 0° rolled, B- 90° rolled, C- 0° rolled annealed, D- 90° rolled annealed, E- detail views of D, showing the changed angle within the rib lattice

The tensile samples underwent different fracture modes of according to their orientation and temper condition. Rolled samples oriented at 0° to the load direction (Figure 6.4-B) experienced fracture along the base of a rib, failing at the interface between the skin and rib sections of the geometry. Samples oriented at 90° (Figure 6.4-C) necked in the middle of a rib, failing within the rib itself. Both of these failure modes occurred in close proximity to ribs and nodes. By contrast, the annealed samples (Figure 6.4-D, E) failed in a random manner with the necking location crossing ribs rather than propagating along rib directions. The rib lattice in annealed samples deformed significantly (Figure 6.4-F), hinging at the nodes and reorientating to resist the applied load. Rolled Isogrid samples in the cold worked state did not experience the same level of deformation in the lattice. The lateral deformation of 90° samples (Figure 6.4-E) exhibited a periodic behaviour, as ribs orientated at 90° to the loading direction resisted reduction in width.

6.3.1 Rolled Isogrid compared to billet material

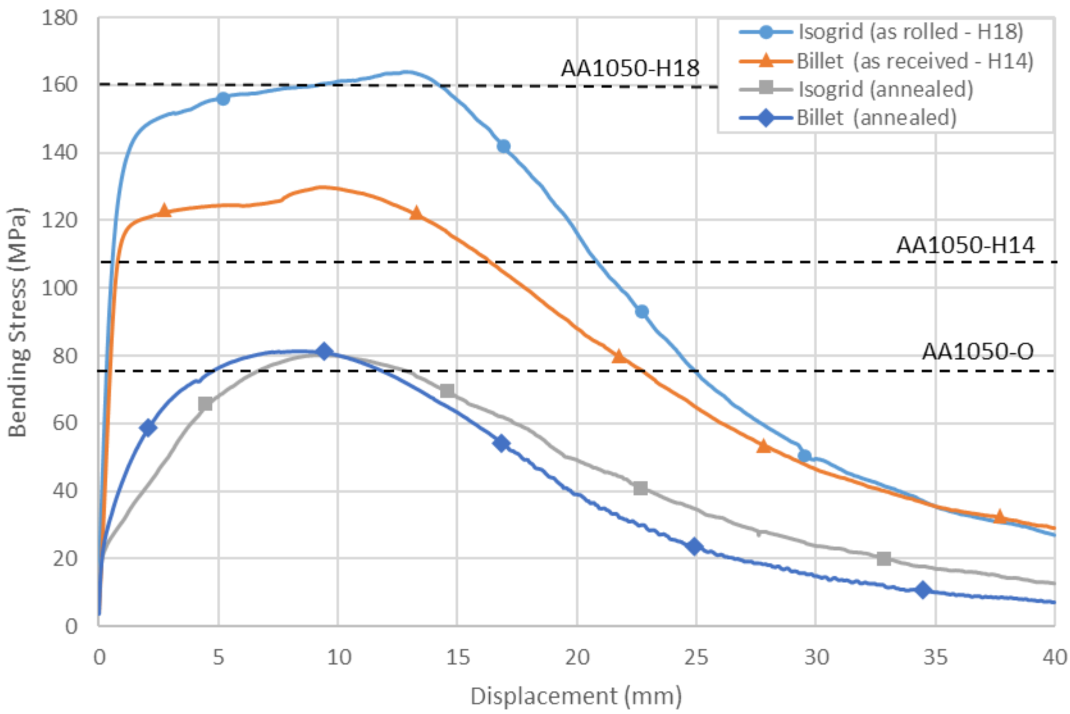

Figure 6.5 Combined bending stress against displacement curves during 3-point, full U bending test, showing approximate temper conditions of the sample groups

Figure 6.5 shows the bending stress curves alongside the nominal ultimate tensile strengths for each relevant temper state of AA1050 [6.45]. The two lower curves in Figure 6.5 show that the annealing treatment successfully transformed the samples to the fully annealed -O condition. The topmost curve indicates that the geometry imparted by the Isogrid rolling process strengthened the Isogrid into a state equivalent to the H18 condition or “fully roll-hardened”.

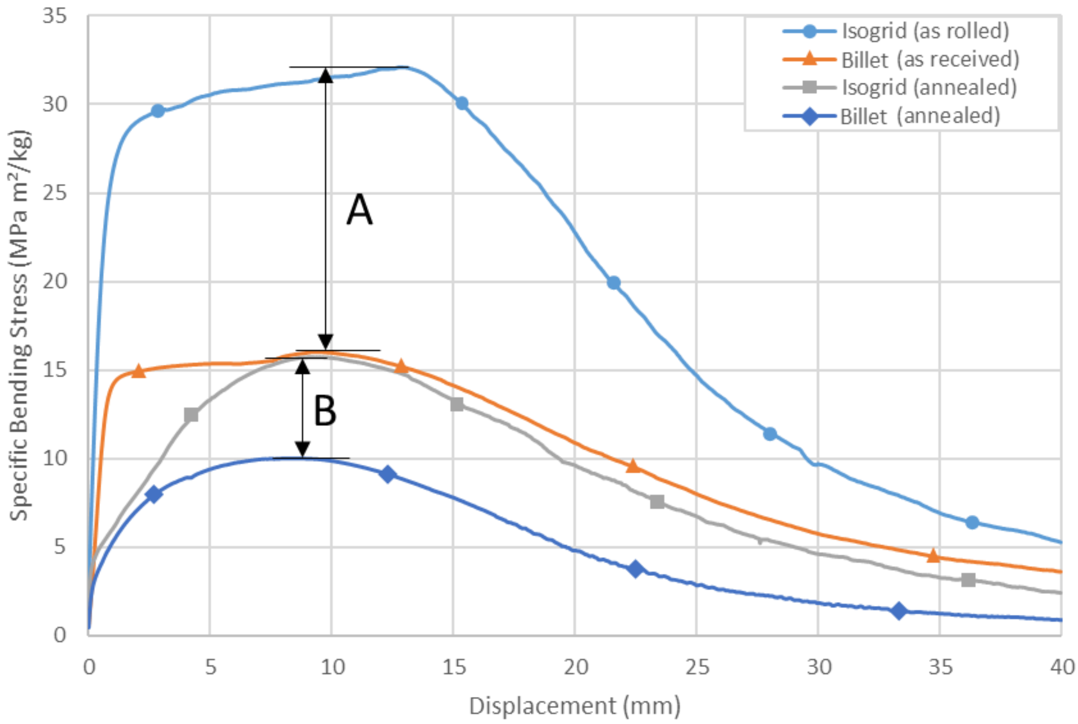

Figure 6.6 Specific bending stress against displacement during 3-point, full U bending test

Division of mechanical properties by density yields specific mechanical properties which can be used to compare materials by their mass efficiency [6.31–6.33,6.46]. Figure 6.6 shows the specific bending stress as a function of displacement over the course of the bend test for samples with and without an annealing treatment. The specific stress increment, denoted as A in Figure 6.6, demonstrates that the as rolled Isogrid is stronger in bending than the as received billet by 100%. Stress increment B (Figure 6.6) shows that the annealed Isogrid is stronger in bending than the annealed billet by 60%. Annealing the samples removed the contribution of cold work to bending strength, revealing only the improvement in strength due to shape factor. Therefore, A denotes the substantial increase in bending strength as a function of the combination of cold work and rib formation in the as rolled Isogrid. Separately, B represents the increase of strength in bending of the produced samples solely attained through the formation of ribs.

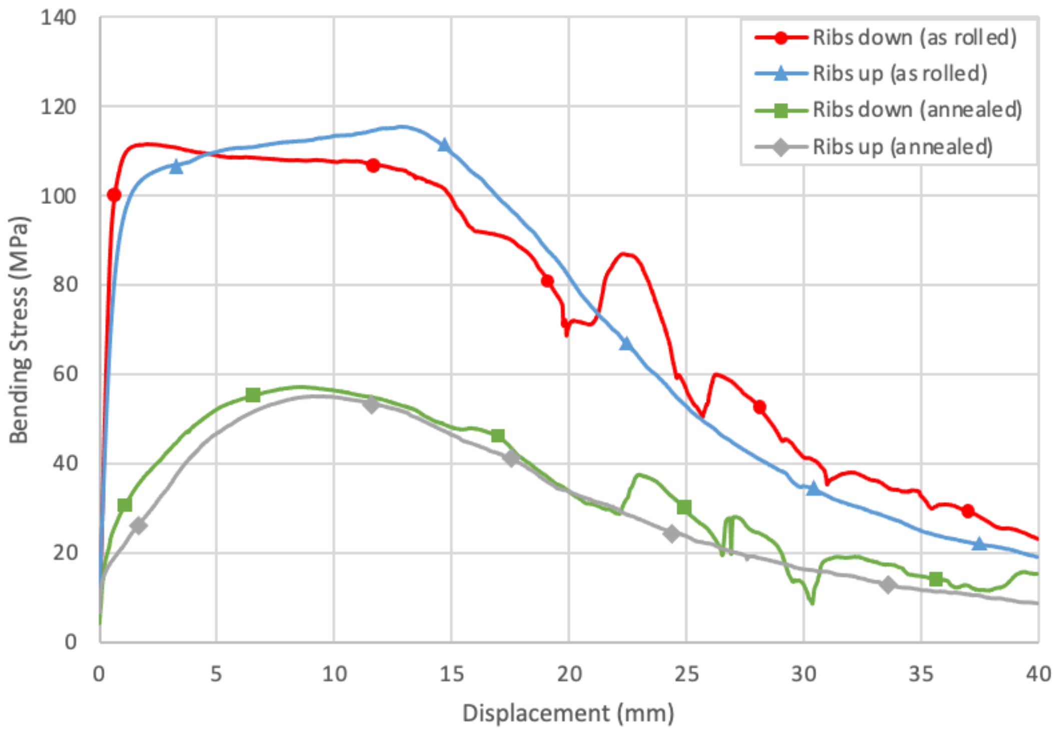

Figure 6.7 Bending stress against displacement during 3-point full U bending test

Figure 6.7 shows the results from testing the rolled Isogrid samples in the ribs up and ribs down configurations. The jagged profile in the graph following 20mm displacement is where the ribs of the ribs down specimens began interfering with the cylindrical supports. However, the general trends of both data sets are very similar, which provides an indication that the rolled Isogrid is quasi-isotropic and that bending strength is symmetrical around its neutral axis despite the asymmetrical geometry of the Isogrid itself.

6.4 *Bending behaviour of rolled and CNC milled Isogrid*

Rolled Isogrid and CNC milled Isogrid were tested in 3-point bending, as outlined in Chapter 3 to compare their relative bending performances. Tests were conducted on both sample types in the 0° and 90° orientations to assess the isotropy of this mechanical property. Figure 6.8 shows the rolled Isogrid had an increased bending strength of 20% in comparison to the CNC milled Isogrid (Figure 6.8-A). Both types of annealed sample groups exhibited the same strength in bending, indicating that the CNC milled and rolled Isogrid sample geometries are comparable.

Figure 6.9 shows that the rolled Isogrid subjected to bending at 90° to the roll direction exhibited a 20% increase in ultimate bending strength (Figure 6.9-A) and 10% increase in bending yield strength (Figure 6.9-B) when compared to the 0° samples. The CNC milled samples followed the same trend by 10% for bending yield strength (Figure 6.9-C) but there was no difference in ultimate bending strength.

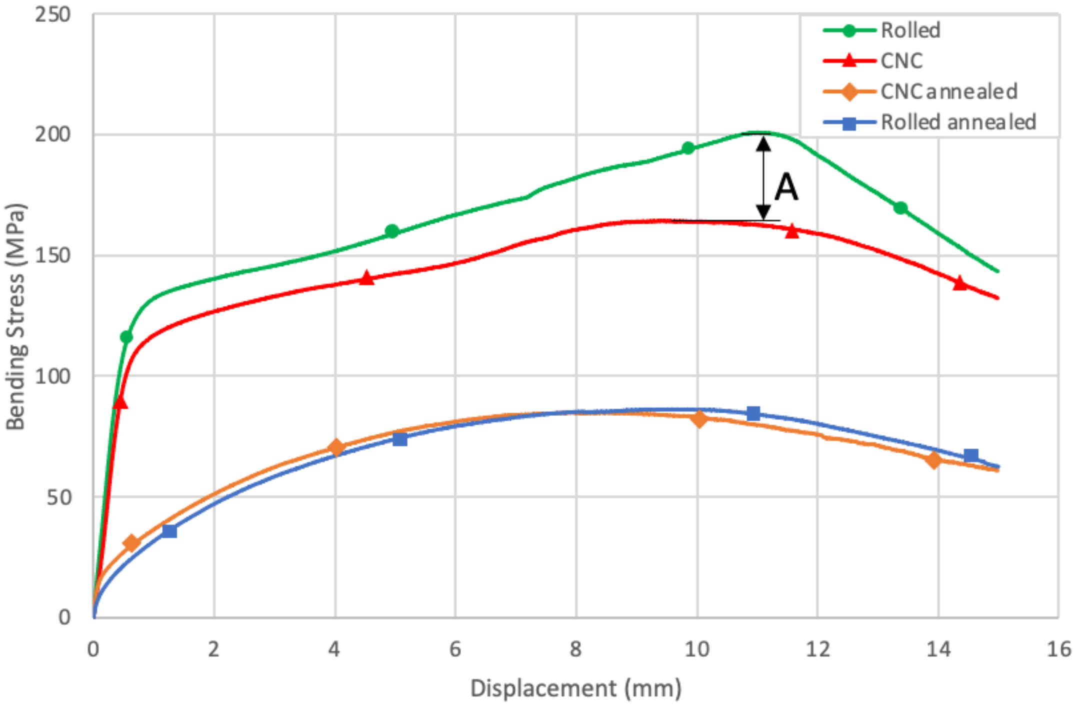

Figure 6.8 Comparison of Rolled Isogrid and CNC milled Isogrid in bending

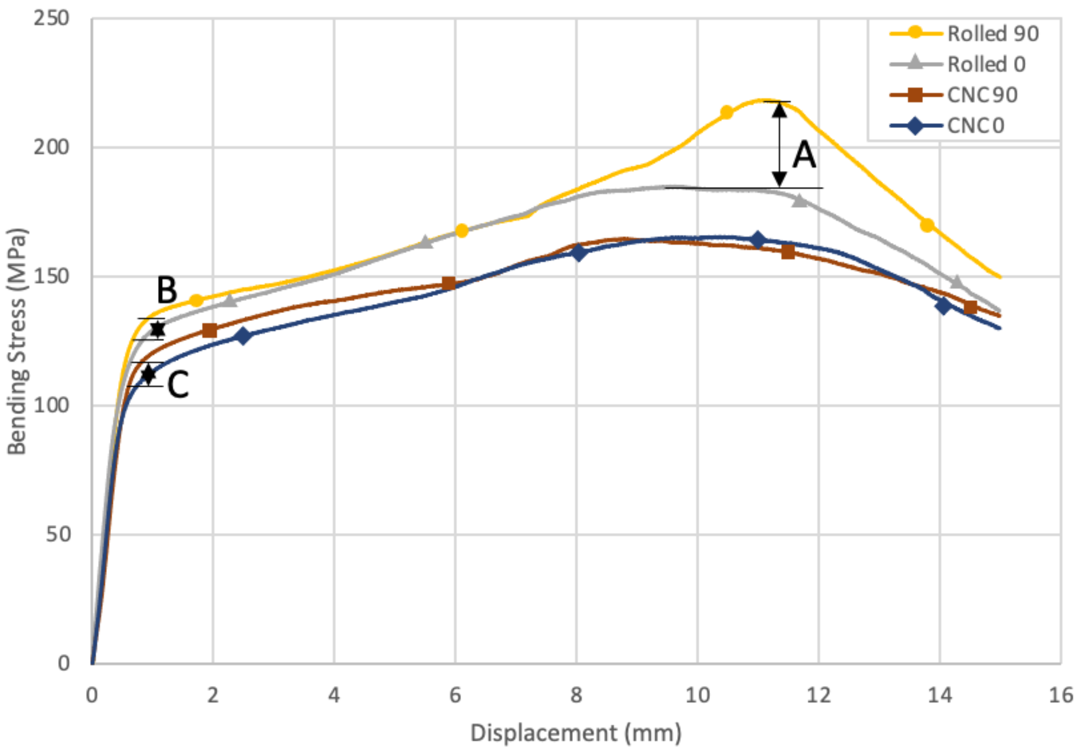

Figure 6.9 Comparison of Bending behaviour between 0° and 90° samples of Rolled Isogrid and CNC milled Isogrid

6.5 Discussion

The data presented in this chapter demonstrates that rolled Isogrid performed favourably when compared to both the billet material, from which it was manufactured, and the CNC milled Isogrid, which represents the conventional method of Isogrid production. The rolled samples outperformed their billet material in the as received condition in terms of bending strength; this remained the case after removing the contribution of cold work via annealing. This indicates that the improvement in strength is in part due to the new geometry and not due to work hardening alone. Rolled Isogrid was found to be 100% stronger in bending than its stock material (Figure 6.6-A), where 60% of this improvement in strength was attributable to shape factor (Figure 6.6-B). The difference between these values, 40%, is attributed to cold work and improvement in microstructure which corresponds with the refined grain structure as discussed in section 5.8. The corresponding shape factor for the rolled Isogrid is the ratio of the maximum bending strengths without considering cold work, which is therefore 1.6 for the annealed samples [6.47]. The cold work imparted during the rolling process increased the bending strength of the rolled Isogrid samples to approximately -H18, or fully roll hardened.

The rolled Isogrid was found to be 20% stronger than CNC milled Isogrid in bending and 10% stronger in tension, which is also a direct result of the cold work and microstructural change imparted by rolling. There is evidence that the rolled and CNC milled Isogrid samples were comparable, as they behaved identically in the post-annealed condition, although some minor variation in tensile strength was present between annealed sample groups (Figure 6.1-B). This cannot be due to shape, as the annealed samples displayed identical behaviour in bending (Figure 6.8). Therefore, the cold work and microstructural refinement, as seen in Chapter 5, accounts for 4.9% of rolled Isogrid's increase in tensile strength over CNC milled Isogrid and the total 22.4% increase in bending strength [6.48]. The enhanced mechanical behaviour of the rolled Isogrid samples indicates that, for the same target geometry, there is an advantage to using the Isogrid rolling method. The Isogrid rolling method as developed in this body of work is limited to the production of one rib lattice geometry, whereas, CNC milling is capable of producing more optimised geometries. Further development of the Isogrid rolling method may explore the geometrical limits of the process; however, as a forming method, the rib-skin ratio or δ (section 3.5) will be limited by material properties and process parameters in a way that CNC milling is not [6.49].

The fracture path of the rolled Isogrid (Figure 6.4-B/C) samples in tension is an indication of the ability of grid-stiffened structures to arrest and redirect cracks. Fractures did not cross ribs within the rolled Isogrid in its cold worked condition, instead they preferentially propagated along the skin/rib intersections. In larger structures, this mechanism allows Isogrid to slow or arrest cracks [6.1,6.40]. After annealing (Figure 6.4-D/E) this behaviour was reduced, and the tensile fracture surface intersected various ribs. These results concur with the hardness maps of rolled Isogrid in its as rolled and annealed states, as reported throughout Chapter 5. The fracture locations in tension correspond with the interface of hard and soft regions for the as rolled Isogrid. The degree of cold work and hardness in the CNC milled and rolled Isogrid samples did not reduce their ductility; all samples failed in a ductile manner as seen in both the tensile curves and fracture surfaces. Annealed samples loaded in both orientations underwent a hinging effect at the nodes which allowed the structural lattice to realign itself with the direction of loading (Figure 6.4-F). This redistribution of loads within the rib lattice also fits with early descriptions of Isogrid as a damage limiting material [6.1,6.54].

The isotropic nature of both rolled and CNC milled Isogrid was restricted to the elastic portion of all tests, with any anisotropic behaviour developing during plastic deformation. The 90° direction was shown to be stronger than the 0° direction in tension and bending. This trend occurred in rolled and CNC milled samples and was therefore present independent of manufacturing process. The 0° direction was shown to be more ductile in tension; however, this behaviour was not found during bending loads. The rolled Isogrid displayed anisotropic behaviour when subjected to plastic deformation in tension. The 0° rib (parallel to rolling direction) contained variation in its cross section, which may explain the reduced performance in this direction. The CNC milled Isogrid exhibited greater anisotropy between the 90° and 0° directions than rolled Isogrid in tension and bending. The microstructural texture of the CNC milled Isogrid reported in Chapter 5, had a higher intensity than that of the rolled Isogrid, due to the “rolling to half hardness” process (H14 condition). This is consistent with the increased anisotropy displayed by the CNC milled Isogrid in both loading regimes, as highly textured microstructures display more anisotropy [6.50–6.52]. These results fit with the consensus in the literature that Isogrid is quasi-isotropic or anisotropic in its failure mechanisms [6.6–6.8,6.58].

The tensile samples loaded at 90° to a principal rib exhibited higher overall tensile strength, and high degrees of hinging at the nodes between principal ribs. These principal ribs at 90° to the load form stiff barriers in the reinforcing lattice which resist lateral compression, locally reducing Poisson’s ratio for the structure. This can be seen in Figure 6.4-E where the reduction in width along the sample is not uniform, as would be expected during a tensile test.

6.6 Conclusions

The rolled Isogrid samples outperformed both the stock material and CNC milled Isogrid in tension and bending in the non-annealed condition:

1. Rolled Isogrid was found to be 100% stronger in bending than its stock material, where 60% of this improvement in strength was attributable to shape factor and 40% to improvement in microstructure.
2. Rolled Isogrid was 22.4% stronger than CNC milled Isogrid in bending and 13.7% stronger in tension, which is a direct result of the cold work imparted by rolling.

These comparisons were further confirmed, as the annealing process verified the comparability between the sample groups by eliminating the differences in mechanical behaviour due to microstructure.

The isotropic characteristics of Isogrid were mostly maintained despite the directionality of the rolling process:

3. The rolled Isogrid exhibited isotropic behaviour in bending but showed minimal anisotropy when subjected to tensile loading.
4. The 90° direction was shown to be stronger than the 0° direction in both tension and bending. The 0° direction was shown to be more ductile in tension; however, this behaviour was not seen under bending loads. This occurred in rolled and CNC milled samples and is therefore present independent of manufacturing process.
5. The CNC milled Isogrid exhibited greater difference between the 90° and 0° directions than rolled Isogrid by 217% in tensile strength and 18% in bending strength, due to the more intense microstructural texture present in the CNC milled samples.
6. The degree of cold work in the CNC milled and rolled Isogrid samples did not reduce their ductility; all samples failed in a ductile manner.
7. The variation in hardness throughout rolled Isogrid samples which was reported in chapter 5 influenced the fracture locations of rolled Isogrid samples during tensile testing.

Rolled Isogrid does not represent a disadvantage when compared to CNC milling for the same target geometry, but rather an advantage when considering the same target geometry.

6.7 Reference List

[6.1] Meyer RR, Harwood OP, Harmon MB, Orlando JI. Isogrid design handbook. NASA 1973.

[6.2] Slysh P, Dyer JE, Furman JH, Key JE. Isogrid Structures. AIAA/ASME/SAE 16th Structures, Structural Dynamics, and Materials Conference 1975. https://doi.org/10.2514/6.1975-816.

[6.3] Slysh P, Ringwald RS, Dyer JE, Browing DL. 1063. Isogrid Weight Optimum Structures. 34th Annual Conference, Seattle, Washington, May 5-7 1975.

[6.4] Slysh P. Isogrid Structures Technology and Applications. San Diego: Society for Allied Weight Engineers; n.d.

[6.5] Ericksen JL, Rivlin RS. Stress-Deformation Relations for Isotropic Materials. Journal of Rational Mechanics and Analysis 1955;4:911–1013.

[6.6] Huybrechts S, Tsai SW. Analysis and behavior of grid structures. Compos Sci Technol 1996;56:1001–15. https://doi.org/10.1016/0266-3538(96)00063-2.

[6.7] Huybrechts S, Meink TE. Advanced grid stiffened structures for the next generation of launch vehicles. IEEE Aerospace Applications Conference Proceedings, vol. 1, 1997, p. 263–9. https://doi.org/10.1109/aero.1997.574417.

[6.8] Fan HL, Fang DN. Anisotropic mechanical properties of lattice grid composites. J Compos Mater 2008;42:2445–60. https://doi.org/10.1177/0021998308095888.

[6.9] Vasiliev V v., Barynin VA, Rasin AF. Anisogrid lattice structures - Survey of development and application. Compos Struct 2001. https://doi.org/10.1016/S0263-8223(01)00111-8.

[6.10] Li G, Chakka VS. Isogrid stiffened syntactic foam cored sandwich structure under low velocity impact. Compos Part A Appl Sci Manuf 2010;41:177–84. https://doi.org/10.1016/j.compositesa.2009.10.007.

[6.11] Li M, Fan H. Multi-failure analysis of composite Isogrid stiffened cylinders. Compos Part A Appl Sci Manuf 2018;107:248–59. https://doi.org/10.1016/j.compositesa.2018.01.010.

[6.12] Delgado XM, Merrett CG. Examination of isotropy assumption in isogrid structures through analysis and experimentation on four isogrid variations. Acta Astronaut 2023;202:422–32. https://doi.org/10.1016/j.actaastro.2022.10.040.

[6.13] Vasiliev V v., Razin AF. Anisogrid composite lattice structures for spacecraft and aircraft applications. Compos Struct 2006;76:182–9. https://doi.org/10.1016/j.compstruct.2006.06.025.

[6.14] Totaro G. Optimal design concepts for flat isogrid and anisogrid lattice panels longitudinally compressed. Compos Struct 2015. https://doi.org/10.1016/j.compstruct.2015.03.067.

[6.15] Totaro G, de Nicola F, Caramuta P. Local buckling modelling of anisogrid lattice structures with hexagonal cells: An experimental verification. Compos Struct 2013;106:734–41. https://doi.org/10.1016/j.compstruct.2013.07.031.

[6.16] Totaro G. Local buckling modelling of isogrid and anisogrid lattice cylindrical shells with triangular cells. Compos Struct 2012;94:446–52. https://doi.org/10.1016/j.compstruct.2011.08.002.

[6.17] Totaro G, de Nicola F. Recent advance on design and manufacturing of composite anisogrid structures for space launchers. Acta Astronaut 2012;81:570–7. https://doi.org/10.1016/j.actaastro.2012.07.012.

[6.18] Lopatin A v., Morozov E v., Shatov A v. Buckling of the composite anisogrid lattice plate with clamped edges under shear load. Compos Struct 2017. https://doi.org/10.1016/j.compstruct.2016.09.025.

[6.19] Totaro G. Local buckling modelling of isogrid and anisogrid lattice cylindrical shells with hexagonal cells. Compos Struct 2013. https://doi.org/10.1016/j.compstruct.2012.07.011.

[6.20] Totaro G. Flexural, torsional, and axial global stiffness properties of anisogrid lattice conical shells in composite material. Compos Struct 2016;153:738–45. https://doi.org/10.1016/j.compstruct.2016.06.072.

[6.21] Totaro G, Spena P, Giusto G, de Nicola F, Kiryenko S, Das S. Highly efficient CFRP anisogrid lattice structures for central tubes of medium-class satellites: Design, manufacturing, and performance. Compos Struct 2021;258:113368. https://doi.org/10.1016/j.compstruct.2020.113368.

[6.22] Slysh P. Isogrid Structural Applications. Conference of the Society of Allied Weight Engineers 1976:27.

[6.23] Slysh P. Picking the best high-strength, lightweight structures. Machine Design 1990;62:85–9.

[6.24] Jaunky N, Knight NF, Ambur DR. Formulation of an improved smeared stiffener theory for buckling analysis of grid-stiffened composite panels. Compos B Eng 1996;27:519–26. https://doi.org/10.1016/1359-8368(96)00032-7.

[6.25] Wang B, Tian K, Hao P, Zheng Y, Ma Y, Wang J. Numerical-based smeared stiffener method for global buckling analysis of grid-stiffened composite cylindrical shells. Compos Struct 2016;152:807–15. https://doi.org/10.1016/j.compstruct.2016.05.096.

[6.26] Greaves GN, Greer AL, Lakes RS, Rouxel T. Poisson's ratio and modern materials. Nat Mater 2011;10:823–37. https://doi.org/10.1038/nmat3134.

[6.27] Wang F. Systematic design of 3D auxetic lattice materials with programmable Poisson's ratio for finite strains. J Mech Phys Solids 2018;114:303–18. https://doi.org/10.1016/j.jmps.2018.01.013.

[6.28] Banhart J, Seeliger HW. Aluminium foam sandwich panels: Manufacture, metallurgy and applications. Adv Eng Mater 2008;10:793–802. https://doi.org/10.1002/adem.200800091.

[6.29] Jiang S, Sun F, Fan H, Fang D. Fabrication and testing of composite orthogrid sandwich cylinder. Compos Sci Technol 2017. https://doi.org/10.1016/j.compscitech.2017.02.009.

[6.30] Birman V, Kardomateas GA. Review of current trends in research and applications of sandwich structures. Compos B Eng 2018. https://doi.org/10.1016/j.compositesb.2018.01.027.

[6.31] Vieira LMG, dos Santos JC, Panzera TH, Rubio JCC, Scarpa F. Novel fibre metal laminate sandwich composite structure with sisal woven core. Ind Crops Prod 2017;99:189–95. https://doi.org/10.1016/j.indcrop.2017.02.008.

[6.32] Zu GY, Lu RH, Li XB, Zhong ZY, Ma XJ, Han MB, et al. Three-point bending behavior of aluminum foam sandwich with steel panel. Transactions of Nonferrous Metals Society of China (English Edition) 2013;23:2491–5. https://doi.org/10.1016/S1003-6326(13)62759-4.

[6.33] Zhang J, Supernak P, Mueller-Alander S, Wang CH. Improving the bending strength and energy absorption of corrugated sandwich composite structure. Mater Des 2013;52:767–73. https://doi.org/10.1016/j.matdes.2013.05.018.

[6.34] Chen L, Fan H, Sun F, Zhao L, Fang D. Improved manufacturing method and mechanical performances of carbon fiber reinforced lattice-core sandwich cylinder. Thin-Walled Structures 2013. https://doi.org/10.1016/j.tws.2013.03.002.

[6.35] Rahimi GH, Zandi M, Rasouli SF. Analysis of the effect of stiffener profile on buckling strength in composite isogrid stiffened shell under axial loading. Aerosp Sci Technol 2013;24:198–203. https://doi.org/10.1016/j.ast.2011.11.007.

[6.36] Jadhav P, Raju Mantena P, Gibson RF. Energy absorption and damage evaluation of grid stiffened composite panels under transverse loading. Compos B Eng 2005. https://doi.org/10.1016/j.compositesb.2005.05.017.

[6.37] Kim TD. Fabrication and testing of thin composite isogrid stiffened panel. Compos Struct 2000. https://doi.org/10.1016/S0263-8223(99)00122-1.

[6.38] Huybrechts SM, Hahn SE, Meink TE. Grid Stiffened Structures: A Survey of Fabrication Analysis and Design Methods. International Conference on Composite Materials 1999.

[6.39] Kim TD. Fabrication and testing of composite isogrid stiffened cylinder. Compos Struct 1999;45:1–6. https://doi.org/10.1016/S0263-8223(98)00124-X.

[6.40] Pettit RG, Wang JJ, Toh C, Metschan S. Validated Feasibility Study of Integrally Stiffened Metallic Fuselage Panels for Reducing Manufacturing Costs Cost Assessment of Manufacturing / Design Concepts. Technical Report: NASA/CR-2000-209342 2000.

[6.41] Heinz A, Haszler A, Keidel C, Moldenhauer S, Benedictus R, Miller WS. Recent development in aluminium alloys for aerospace applications. vol. 280. 2000.

[6.42] Hannum NP, Kasper HJ, Pavli AJ. Experimental and theoretical investigation of fatigue life in reusable rocket thrust chambers. AAIA/SAE 12th Propulsion Conference, 1976. https://doi.org/doi:10.2514/6.1976-685.

[6.43] Elamin M, Li B, Tan KT. Impact damage of composite sandwich structures in arctic condition. Compos Struct 2018;192:422–33. https://doi.org/10.1016/j.compstruct.2018.03.015.

[6.44] Hoffman ME, Hoffman PC. Corrosion and fatigue research-structural issues and relevance to naval aviation. vol. 23. 2001.

[6.45] ASM International. Properties of Wrought Aluminum and Aluminum Alloys. Properties and Selection: Nonferrous Alloys and Special-Purpose Materials, vol. 2. 10th ed., ASM International; 1990, p. 62–122. https://doi.org/10.31399/asm.hb.v02.a0001060.

[6.46] I'Anson SJ, Sampson WW. Competing Weibull and stress-transfer influences on the specific tensile strength of a bonded fibrous network. Compos Sci Technol 2007;67:1650–8. https://doi.org/10.1016/j.compscitech.2006.07.002.

[6.47] Ashby MF. Overview No. 92: Materials and shape. Acta Metallurgica Et Materialia 1991;39:1025–39. https://doi.org/10.1016/0956-7151(91)90189-8.

[6.48] Garrick AJH, Toumpis AI, Galloway AM. Developing a novel manufacturing method to produce stiffened plate structures. International Journal of Advanced Manufacturing Technology 2021:2805–13. https://doi.org/10.1007/s00170-020-06525-x.

[6.49] Sabroff AM, Boulger FW, Henning HJ, Spretnak JW. A manual on Fundamentals of forging practice. 1964.

[6.50] Hirsch J. Texture evolution during rolling of aluminium alloys. TMS Light Metals 2008:1071–7.

[6.51] Duan X, Jiang H, Mi Z, Cheng L, Wang J. Reduce the planar anisotropy of AA6016 aluminum sheets by texture and microstructure control. Crystals (Basel) 2020;10:1–15. https://doi.org/10.3390/cryst10111027.

[6.52] Lopes AB, Barlat F, Gracio JJ, Ferreira Duarte JF, Rauch EF. Effect of texture and microstructure on strain hardening anisotropy for aluminum deformed in uniaxial tension and simple shear. Int J Plast 2003;19:1–22. https://doi.org/10.1016/S0749-6419(01)00016-X.

[6.53] Meyer RR, March V. Isogrid - A Simple, Efficient, Stiffening Concept. NASA 1973. https://doi.org/10.2514/6.1973-365.

[6.54] Slysh P. 1096. Isogrid Structural Applications. 35th Annual Conference, Philadelphia, Pennsylvania, May 24-26 1976:27.

[6.55] Michelis P, Spitas V. Numerical and experimental analysis of a triangular auxetic core made of CFR-PEEK using the Directionally Reinforced Integrated Single-yarn (DIRIS) architecture. Compos Sci Technol 2010. https://doi.org/10.1016/j.compscitech.2010.01.013.

[6.56] Li T, Chen Y, Hu X, Li Y, Wang L. Exploiting negative Poisson's ratio to design 3D-printed composites with enhanced mechanical properties. Mater Des 2018. https://doi.org/10.1016/j.matdes.2018.01.034.

[6.57] Spadoni A, Ruzzene M. Elasto-static micropolar behavior of a chiral auxetic lattice. J Mech Phys Solids 2012;60:156–71. https://doi.org/10.1016/j.jmps.2011.09.012.

[6.58] Vasiliev V V., Barynin VA, Rasin AF. Anisogrid lattice structures - Survey of development and application. Compos Struct 2001. https://doi.org/10.1016/S0263-8223(01)00111-8.

7 Fatigue behaviour of rolled Isogrid

7.1 Review of relevant fatigue theory

This thesis has so far reported the microstructural and mechanical properties of rolled and CNC milled Isogrid. This chapter will build on those results by examining the fatigue behaviour of Rolled and CNC milled Isogrid. Fatigue is a common failure mechanism, and Sangid [7.1] states that at least 50% of metallic failures in industry are due to fatigue. As such, the characterisation of fatigue behaviour in novel structures such as rolled Isogrid is a task of primary importance.

Fatigue failure is intrinsically linked to the loading history of a component, as repeated stress cycles impart cumulative damage to a component, resulting in the initiation of a crack from either a pre-existing defect or from microstructural effects [7.1–7.6]. Miller [7.7] distinguishes these two initiation mechanisms as the defining difference between fracture mechanics-based fatigue behaviour and microstructural based fatigue behaviour. Both fatigue mechanisms are stochastic, and the propagation stage is rapid, meaning that the majority of a component's fatigue life occurs before a crack is formed [7.7]. Eventually, the structure fails when the crack has weakened an area to the point that another failure mode can occur, such as tensile failure [7.8,7.9].

Stress raising features are a primary source of crack initiation, and greatly reduce fatigue performance [7.3,7.4,7.8,7.10–7.12]. Defects, notched geometries and abrupt changes in cross section amplify stresses in their vicinity, leading to high degrees of localised plasticity and the formation of a crack [7.6–7.9,7.13]. The transition between the rib lattice and skin section of advanced grid stiffened structure, such as Isogrid, is one such change in cross section. Once the crack has initiated, propagation must first overcome microstructural obstacles such as grain boundaries, in a stage governed by elastic-plastic fracture mechanics [7.7]. Miller [7.7] emphasised the importance of this microstructural resistance in slowing crack propagation for defects which are not aligned perpendicularly with the axis of loading (such as shear cracks). Once the crack attains sufficient size in comparison to the surrounding grain structure, it propagates perpendicular to the axis of principal stress in a linear elastic manner [7.7,7.14,7.15].

Microstructural related crack initiation occurs as irreversible plastic deformation is induced during stress cycling [7.1,7.16]. Alternating states of loading promote dislocation motion along slip planes in areas of high stress concentration [7.1]. Dislocations which experience cross slip, annihilation or entanglement cannot reverse this movement and return to their previous state, resulting in the accumulation of plastic deformation over time [7.1]. This leads to the formation of persistent slip bands where dislocations begin to pile up [7.1,7.16,7.17]. In a polycrystalline material such as AA1050, extrusions form from persistent slip bands and impinge on grain boundaries, increasing the stress concentration at this interface and providing a likely site for crack initiation [7.1,7.16].

Turnbull et al. [7.18] showed that increased grain size has a negative impact on the fatigue resistance of commercially pure aluminium. This finding was confirmed by Höppel et al. [7.19] in fatigue tests reaching the very high cycle range. The microstructural discussion by Sangid [7.1] provides the theoretical context for this result; large grains develop slip bands more readily than smaller grains. The resulting prevalence of slip band/ grain boundary interactions promotes crack initiation and consequent propagation to failure. Grain size effects have been studied in detail by researchers of severe plastic deformation (SPD) based strengthening methods [7.20–7.22]. Fatigue life has been shown to improve due to SPD generated ultrafine grain structures in a manner commensurate with the overall increase in strength [7.20,7.21]. However, Eivani et al. [7.23,7.24] found that twist extrusion and shear extrusion grain refinement techniques negatively impacted fatigue life due to the increased incidence of cyclic softening [7.25]. Verlinden [7.26] reported results which may offer some reconciliation of these opposing positions; SPD microstructures have better fatigue performance in high cycle fatigue loading regimes, but a poorer response to low cycle fatigue. SPD refines grain structure throughout the bulk of a material; however, localised refinements in microstructure have been found to increase stress concentration and promote fatigue crack initiation [7.27].

The fatigue performance of Isogrid has not been widely studied throughout its usage in rockets and launch vehicles, as single use launch vehicles were only required to withstand a short duration of high intensity loading. Rocket reusability has recently become the subject of increased attention [7.28,7.29], increasing the relevant of fatigue failure for Isogrid applications. The Isogrid design handbook [7.30] includes design considerations on manufacturing techniques intended to alleviate the likelihood of fatigue failure. Isogrid will exhibit some degree of fatigue resistance as stiffened plate structures have been found to be intrinsically fatigue resistant as discussed in Chapter 6 [7.31–7.37]. Integral stiffeners are reported to delay and deflect crack propagation along stiffener orientations when subjected to cyclic loading, which has led to the adoption of stiffened fuselage structures throughout the aviation industry for increased safety [7.36,7.38]. As stiffening rib directions may not be oriented perpendicular to the loading axis, this behaviour enforces a greater duration of elastic plastic crack propagation through the mechanisms discussed by Miller [7.7]. However, changes in cross section are known to be stress concentrators [7.6,7.13], and the increased stress levels at the rib / skin transition regions increases the likelihood of fatigue initiation and accelerate the growth of cracks in their vicinity [7.6,7.13,7.39,7.40].

The fatigue performance of rolled Isogrid and CNC milled Isogrid has been examined and compared. The fatigue performance of Isogrid is poorly represented in the scientific literature, as such, the methodology detailed in Chapter 3, dataset and findings reported in this chapter are of significant novelty.

7.2 Results

The data in Figure 7.1 indicate that the rolled Isogrid performed poorly in comparison to the CNC milled Isogrid. The rolled Isogrid failed at a mean value of 87,500 cycles for 80% of yield, whereas the CNC milled Isogrid failed at 249,000 cycles, representing a 2.85x difference in fatigue resistance. This trend further diverged to an 8.4x difference at 70% of yield. At 60% of yield, the CNC milled Isogrid reached the run-out value of 3E+6, 9.5x greater than the mean value of the rolled Isogrid (317000 cycles).

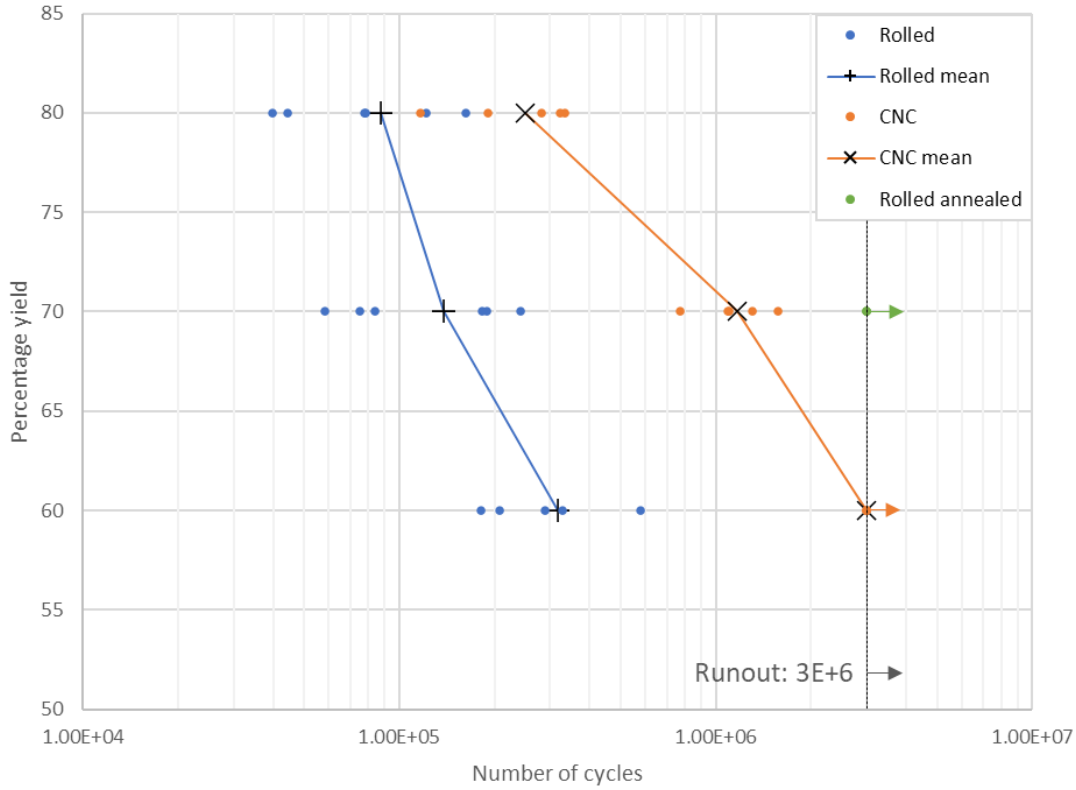

Figure 7.1 S-N curve of the rolled and CNC milled Isogrid samples tested under fatigue conditions (normalised to yield stress)

It was hypothesised that the relatively poor fatigue performance of the rolled Isogrid may be due to microstructural inhomogeneity; therefore, an extra set of fatigue tests was performed on rolled Isogrid samples after an annealing treatment. The annealed samples were tested at 70% of their measured yield stress and each sample reached run-out at 3E+6 cycles. Figure 7.1 presents all 3 sample conditions normalised against their respective yield strengths; whereas, Figure 7.2 shows the absolute values of stress experienced by each condition.

The rolled Isogrid samples primarily experienced crack initiation in the vicinity of the 0° ribs, which were aligned with the axis of loading. These initiation sites occurred either at the side of the sample (Figure 7.3) or in the central rib (Figure 7.4). Among the tested samples, failure occurred in both locations and at varying points throughout the gauge section, giving satisfactory assurance that sample preparation did not influence the results.

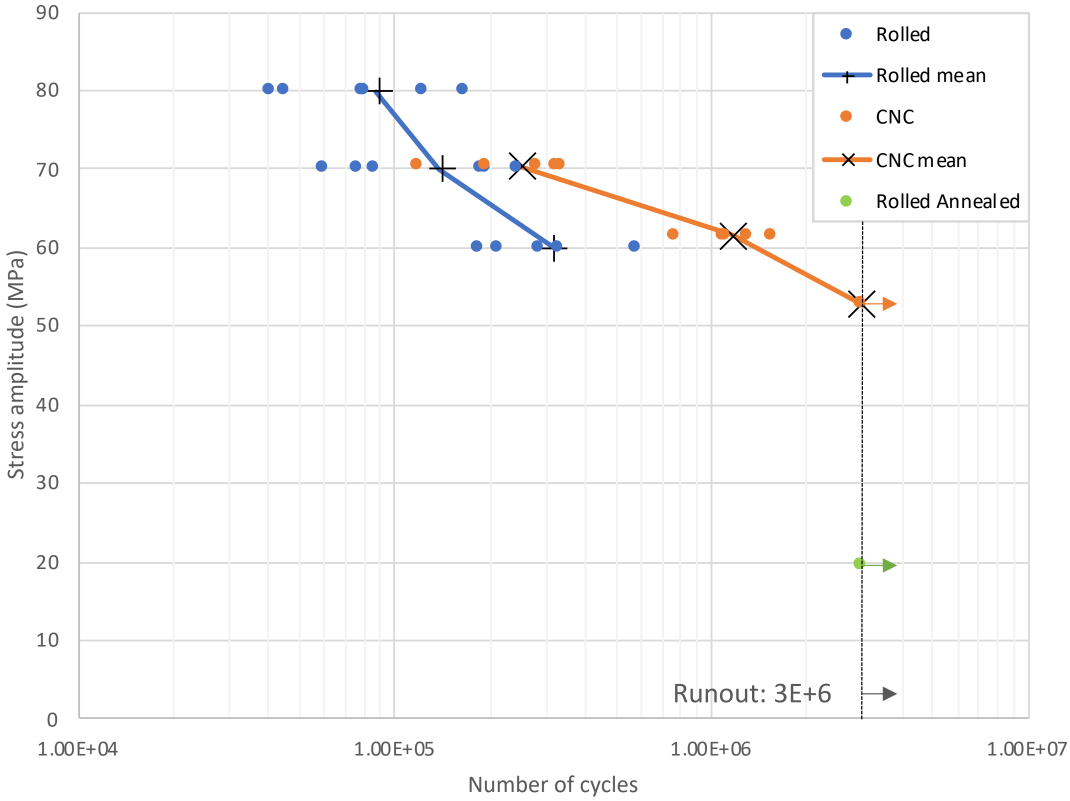

Figure 7.2 S-N curve of the rolled and CNC milled Isogrid samples tested under fatigue conditions (absolute stress)

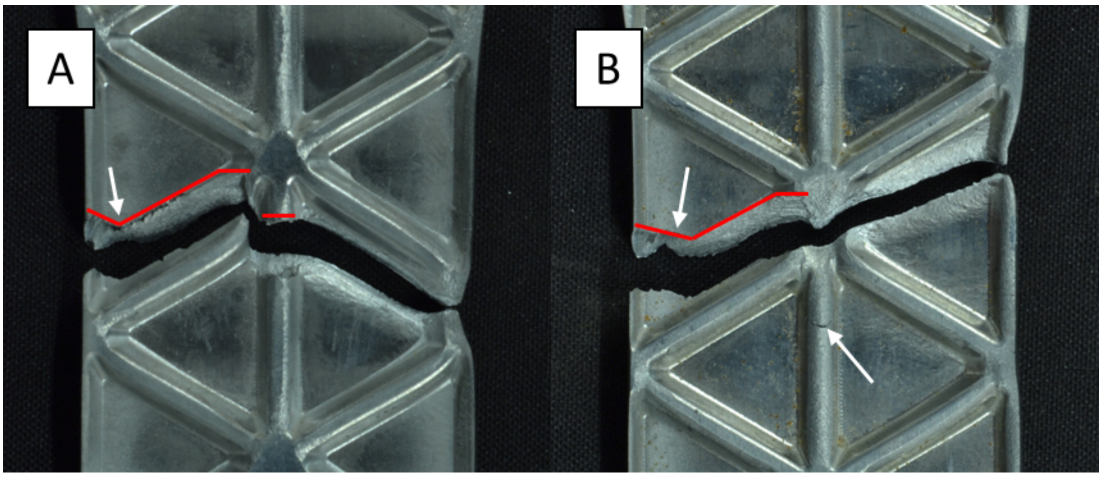

Figure 7.3 Rolled Isogrid fatigue fractures of 2 samples (fatigue propagation paths coloured red, initiation sites marked by white arrow)

The macro photographs in Figure 7.3 show typical fatigue fractures found in the rolled Isogrid samples. In both samples shown in Figure 7.3, the crack has initiated at a 0° rib on the sample edge, in a manner perpendicular to the principal stress. These cracks were then deflected by the ribs and continued propagating at 60° to the applied load direction (or 30° to the preferred propagation path). The fatigue cracks have propagated parallel to the geometry of the rib lattice, at an angle to the applied load. In Figure 7.3-A, the crack was deflected at the rib node, changing direction during the propagation phase. In Figure 7.3-B, the crack appears to have intersected the rib node, continuing along its original path.

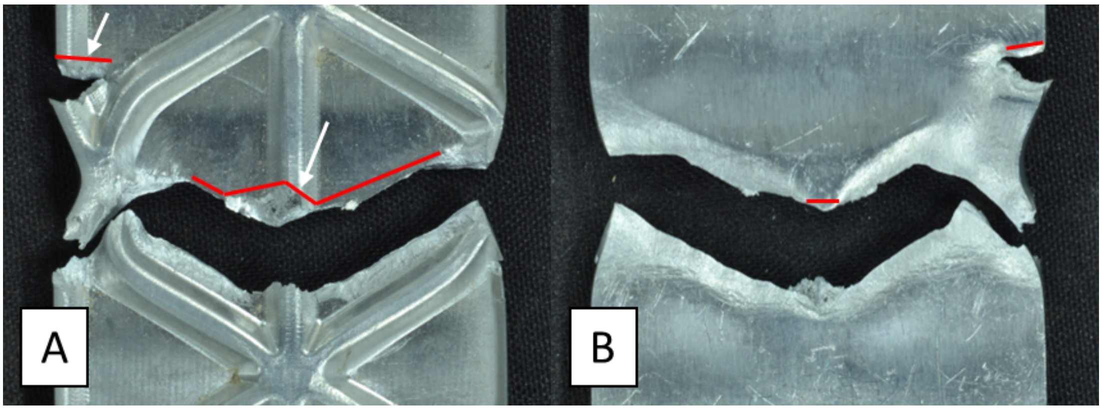

Figure 7.4 Rolled Isogrid fatigue fracture A- rib side, B- skin side (fatigue propagation paths coloured red - initiation sites marked by white arrow)

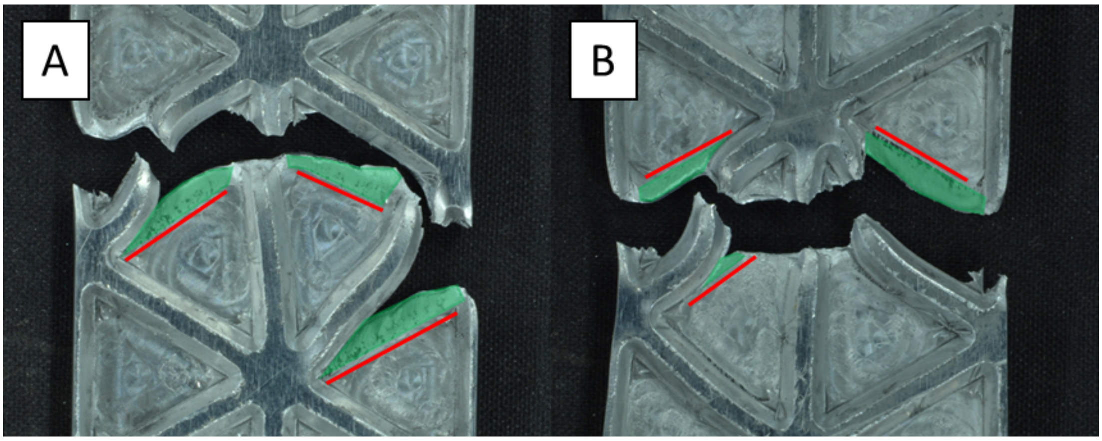

Figure 7.5 CNC milled Isogrid fatigue fractures of 2 samples (fatigue propagation paths coloured red, areas of significant rib undercut coloured green)

Figure 7.4 shows a rolled Isogrid sample in which the crack initiated in its centre. The secondary initiation site seen in Figure 7.4-A occurred on a 0° rib at the edge of the sample. The edges of the main fracture in Figure 7.4-A are sharp, whereas the central rib in Figure 7.4-B is the only portion of the fracture surface without evidence of necking. This suggests that the fatigue crack has propagated along the ribbed face of the rolled Isogrid, rather than through the thickness of the specimen. Cracking along the rib / skin interface is consistent with the literature, which suggests stress concentrations are amplified near changes in cross section [7.6,7.13,7.39].

Figure 7.5 shows the typical fracture behaviour of the CNC milled Isogrid samples during cyclic loading. These fatigue cracks have propagated much more closely along the rib / skin transitions, which is likely due to the sharp corners between these areas left by the CNC milling process. Fatigue cracks in the CNC milled samples propagated across ribs rather than cross nodes. In Figure 7.5-A, 2 separate fatigue cracks have developed simultaneously. The areas coloured green indicate where fatigue cracks have propagated at a downward angle to the rib. These cracks extended through the full thickness of the samples, in contrast to the rolled Isogrid where cracks preferentially remained on the patterned face.

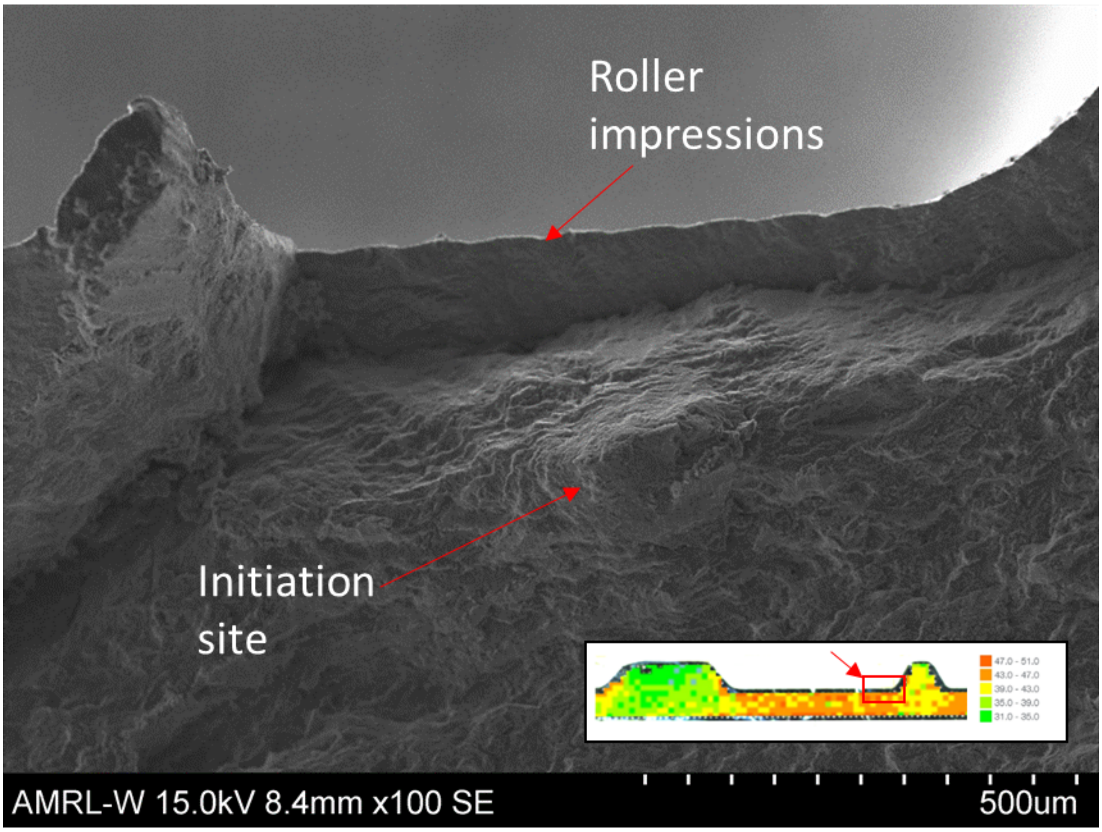

Figure 7.6 Striations in proximity to rib transition area on rolled Isogrid sample, A- Initiation site, B- impressions from rolling process

The SEM micrograph in Figure 7.6 shows evidence of fatigue striations and crack propagation in proximity to the rib / skin transition zone in a rolled Isogrid sample. There is a potential crack initiation site at Figure 7.6 from which the striations are radially expanding. This area corresponds to the interface between the hard and soft regions, as seen in the hardness results for rolled Isogrid in section 5.5. The impressions left by the roller can be seen in the form of shallow arcs (Figure 7.6).

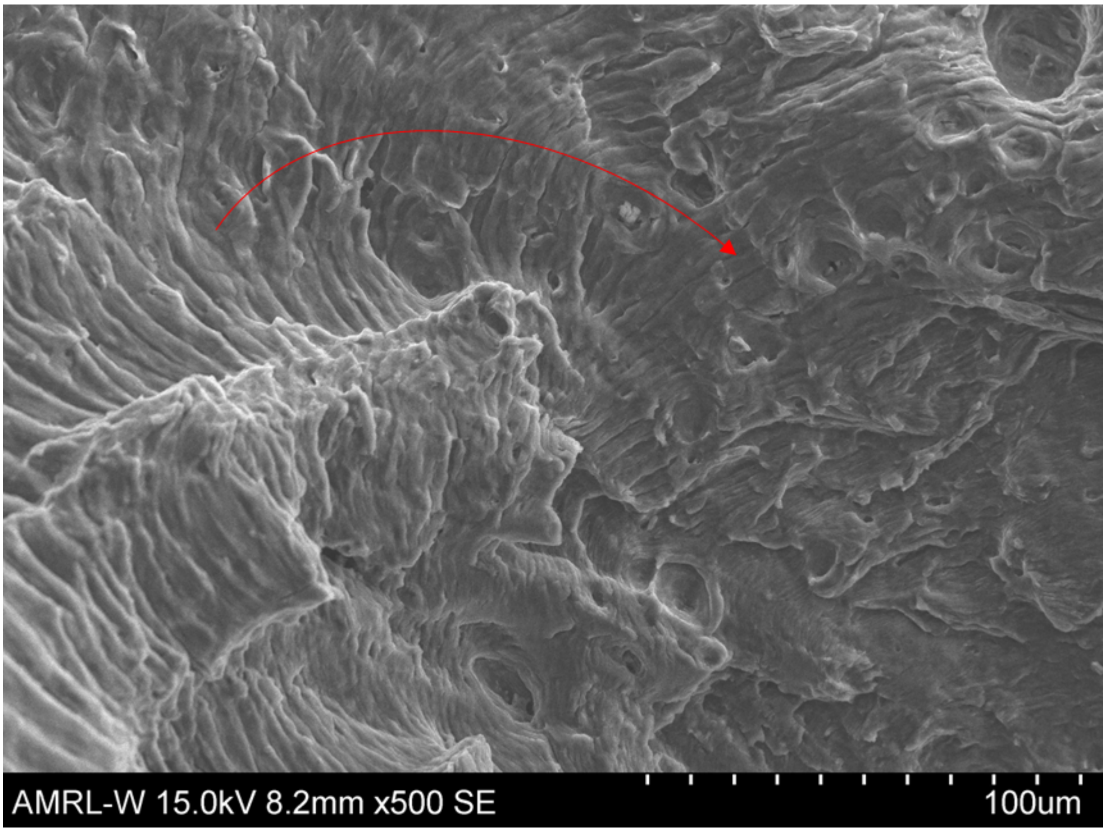

Figure 7.7 Striations changing direction near the rib in a rolled Isogrid sample

Figure 7.7 shows a set of striations in which the direction of crack propagation has clearly rotated in the presence of the rib geometry. Fatigue cracks typically follow planar paths perpendicular to the applied load [7.14,7.15], making directional reorientation an unusual finding. However, this finding supports the body of research on the fatigue of grid stiffened structures and the fracture behaviour noted in Figure 7.3-4, which has evidenced the tendency of fatigue crack trajectories to adjust and follow the rib / skin transition region.

7.3 Discussion

The CNC milled Isogrid outperformed the rolled Isogrid in under cyclic loading at every stress level tested, with some data points showing approximately an order of magnitude of difference. However, after an annealing treatment, the rolled Isogrid reached the run-out cycle threshold at a stress level where CNC milled Isogrid experienced fatigue failure. This is a result of microstructural homogenisation, as the sample geometry and preparation remained identical. The stress range tested (70%) was also identical in relation to the measured yield stress of the rolled and annealed Isogrid. This disparity in performance decreases in Figure 7.2 which is expressed in absolute stress amplitude.

A consistent source of increased crack propagation at the rib skin boundary in both sample types is the change in cross sectional area, which has been reported throughout the literature as a source of increased stress and fatigue cracking [7.6,7.7,7.13]. Crack propagation in this location was noted in both rolled (Figure 7.3-3) and CNC milled (Figure 7.5) Isogrid samples. The CNC milled samples did not contain the same degree of microstructural variation, as seen in the rolled samples, and contained sharper rib / skin transitions. This indicates that change in cross section is likely the sole reason for crack propagation in the rib skin transition region for the CNC samples. This corroborates the findings of Pettit et al. [7.36], which showed integrally stiffened structures deflect cracking at areas of increased cross section such as ribs. The microstructure of the CNC samples, as seen in Chapter 5, is highly plastically deformed to attain the H14 rolled to half hardness state and improve mechanical characteristics. The marked improvement in high cycle fatigue life exhibited by CNC samples is therefore consistent with the response of SPD materials to fatigue loading, as found by Verlinden [7.26].

All rolled Isogrid samples experienced fatigue cracking near to the 0° ribs, with initiation sites either interior to the ribs or at the interface between soft (rib) and hard (skin) regions of the structure (Figure 7.6). The strength of these regions varies proportionately to cold work and hardness; therefore, uniform strains of the entire sample impart varying levels of stresses into the skin and node sections. Similar to a compatibility style structural analysis problem, this creates additional shear stresses between the node and skin sections which may explain increased crack initiation and propagation in these regions. Combining microstructural variation and additional shear stresses with the change in cross section explains the prolific crack propagation at the rib/node interface within rolled samples. Slight variations in the 0° rib, as seen in Chapter 4, are also responsible for increased fatigue initiation in this region, as the cross section was variable along the rib.

While both rolled and CNC milled Isogrid experienced crack propagation along rib orientations, different behaviours were exhibited by each when cracks approached node sections. Fatigue cracks in rolled Isogrid intersected the node geometry as seen in Figure 7.3-B. By contrast, the nodes of CNC milled samples did not fail in this way throughout any of the stress ranges tested. The rib lattice and node geometry of rolled Isogrid represents the softer, lesser deformed areas, as seen in the hardness map in Chapter 5, Figure 5.20. Similar tensile failure of the rib geometry can be seen in Chapter 6, Figure 6.6-C, where a rib in the 90° direction has necked and failed. This reduction in strength of the rib lattice relative to the skin section has diminished its effectiveness as a barrier to fatigue propagation.

The annealed rolled Isogrid samples reached runout, which indicates that the initiation mechanisms previously affecting the rolled samples had been eliminated. This suggests that they are in the microstructural crack initiation regime, where the other samples have initiated cracking from manufacturing related stress raisers (cold work, CNC milling artefacts, changes in cross section). The deflection of fatigue cracks in Isogrid samples at 30° to the preferred direction of propagation may have improved the overall fatigue life of all the specimens [7.7]. The improved fatigue performance of samples tested in the annealed condition indicates that the microstructural changes imparted during production of Isogrid reduced the fatigue life of the Isogrid structure. Testing Isogrid samples in this condition has led to a clear scientific result; however, the annealed condition is not proposed as a material for use in industrial design as the reduction in absolute stress amplitude experienced for 70% of their yield strength is considerable (Figure 7.2).

7.4 Conclusions

1. Rolled Isogrid performed significantly worse than CNC milled Isogrid in the cold worked state. This is due to accelerated crack initiation in proximity to microstructural transitions and shear stresses between areas of differential stiffness in the rolled Isogrid.
2. Annealing treatments of the rolled Isogrid improved its fatigue resistance such that the samples did not fail before runout. The recrystallised microstructure no longer contained features promoting crack initiation.

3. Fatigue fractures in the rolled Isogrid samples were deflected by the rib geometry in both sample groups, in a manner consistent with findings on rib stiffened structures in the literature. However, the rolled Isogrid experienced preferential crack propagation on the rib lattice side of the structure.

These results have a profound impact on the direction of future work on this field, as it has clearly identified a challenge which must be addressed as the technology is further developed. Fatigue performance is a very important aspect of a materials suitability for industrial applications, and the poor performance of rolled Isogrid due to its microstructural inhomogeneity is an aspect for which mitigation strategies such as heat treatments may be explored.

7.5 Reference List

[7.1] Sangid MD. The physics of fatigue crack initiation. Int J Fatigue 2013;57:58–72. https://doi.org/10.1016/j.ijfatigue.2012.10.009.

[7.2] Forman RG. Study of fatigue crack initiation from flaws using fracture mechanics theory. Eng Fract Mech 1972;4:333–45. https://doi.org/10.1016/0013-7944(72)90048-3.

[7.3] Polak J. On the Role of Point Defects in Fatigue Crack Initiation. vol. 92. 1987.

[7.4] Zhang SY, Spiryagin M, Ding HH, Wu Q, Guo J, Liu QY, et al. Rail rolling contact fatigue formation and evolution with surface defects. Int J Fatigue 2022;158. https://doi.org/10.1016/j.ijfatigue.2022.106762.

[7.5] Heywood RB. The Relationship Between Fatigue and Stress Concentration. Aircraft Engineering and Aerospace Technology 1947. https://doi.org/https://doi.org/10.1108/eb031482.

[7.6] Peterson RE. Stress-Concentration Phenomena in Fatigue of Metals. J Appl Mech 1933;1:157–67. https://doi.org/10.1115/1.4012221.

[7.7] Miller KJ. The two thresholds of fatigue behaviour. Fatigue Fract Eng Mater Struct 1993;16:931–9. https://doi.org/10.1111/j.1460-2695.1993.tb00129.x.

[7.8] Thompson N, Wadsworth NJ. Metal fatigue. Adv Phys 1958;7:72–169. https://doi.org/10.1080/00018735800101177.

[7.9] Pineau A, McDowell DL, Busso EP, Antolovich SD. Failure of metals II: Fatigue. Acta Mater 2016;107:484–507. https://doi.org/10.1016/j.actamat.2015.05.050.

[7.10] Lombard H, Hattingh DG, Steuwer A, James MN. Optimising FSW process parameters to minimise defects and maximise fatigue life in 5083-H321 aluminium alloy. Eng Fract Mech 2008;75:341–54. https://doi.org/10.1016/j.engfracmech.2007.01.026.

[7.11] Fischer C, Schweizer C. Experimental investigation of the damage characteristics of two cast aluminium alloys: Part III – Influence of the local microstructure and initial defect size on the fatigue properties. Int J Fatigue 2021;152. https://doi.org/10.1016/j.ijfatigue.2021.106388.

[7.12] Thompson N, Wadsworth N, Louat N. XI. The origin of fatigue fracture in copper. Philosophical Magazine 1956;1:113–26. https://doi.org/10.1080/14786435608238086.

[7.13] Heywood RB. The Relationship Between Fatigue and Stress Concentration. Aircraft Engineering and Aerospace Technology 1947;19:81–4. https://doi.org/10.1108/eb031482.

[7.14] Billaudeau T, Nadot Y, Bezine G. Multiaxial fatigue limit for defective materials: Mechanisms and experiments. Acta Mater 2004;52:3911–20. https://doi.org/10.1016/j.actamat.2004.05.006.

[7.15] Galatolo R, Lanciotti A. Fatigue crack propagation in residual stress fields of welded plates. Int J Fatigue 1997;19:43–9.

[7.16] Smith GC, Friedel J, Cina B. The Initial Fatigue Crack [and Discussion]. Source: Proceedings of the Royal Society of London Series A, Mathematical and Physical Sciences 1957;242:189–97.

[7.17] Friedel J, Feltham P. The Mechanism of Work-Hardening and Slip-Band Formation [and Discussion]. Proceedings of the Royal Society of London Series A 1957;242:147–59.

[7.18] Turnbull A, de Los Rios ER. the Effect of Grain Size on the Fatigue of Commercially Pure Aluminium. Fatigue Fract Eng Mater Struct 1995;18:1455–67. https://doi.org/10.1111/j.1460-2695.1995.tb00868.x.

[7.19] Höppel HW, Prell M, May L, Göken M. Influence of grain size and precipitates on the fatigue lives and deformation mechanisms in the VHCF-regime. Procedia Eng, vol. 2, 2010, p. 1025–34. https://doi.org/10.1016/j.proeng.2010.03.111.

[7.20] Soliman MS, El-Danaf EA, Almajid AA. Enhancement of static and fatigue strength of 1050 Al processed by equal-channel angular pressing using two routes. Materials Science and Engineering A 2012;532:120–9. https://doi.org/10.1016/j.msea.2011.10.072.

[7.21] Puertas I, Luis Pérez CJ, Salcedo D, León J, Fuertes JP, Luri R. Design and mechanical property analysis of AA1050 turbine blades manufactured by equal channel angular extrusion and isothermal forging. Mater Des 2013;52:774–84. https://doi.org/10.1016/j.matdes.2013.05.089.

[7.22] Shukla S, Komarasamy M, Mishra RS. Grain size dependence of fatigue properties of friction stir processed ultrafine-grained Al-5024 alloy. Int J Fatigue 2018;109:1–9. https://doi.org/10.1016/j.ijfatigue.2017.12.007.

[7.23] Naeimi M, Eivani AR, Jafarian HR, Boutorabi SMA, Shams H. Correlation between microstructure, tensile properties and fatigue life of AA1050 aluminum alloy processed by pure shear extrusion. Materials Science and Engineering A 2017;679:292–8. https://doi.org/10.1016/j.msea.2016.09.113.

[7.24] Eivani AR, Hosseini M, Jafarian HR, Mousavi Anijdan SH, Park N. Microstructural evolution and fatigue properties of severely deformed AA1050 aluminum alloy. Mater Charact 2017;130:204–10. https://doi.org/10.1016/j.matchar.2017.06.016.

[7.25] Kwan CCF, Wang Z. The cyclic deformation behavior of severe plastic deformation (SPD) metals and the influential factors. Metals (Basel) 2012;2:41–55. https://doi.org/10.3390/met2010041.

[7.26] Verlinden B. Severe plastic deformation of metals. Metalurgija - Journal of Metallurgy 2005.

[7.27] Chen Y, He C, Liu F, Wang C, Xie Q, Wang Q, et al. Effect of microstructure inhomogeneity and crack initiation environment on the very high cycle fatigue behavior of a magnesium alloy. Int J Fatigue 2020;131. https://doi.org/10.1016/j.ijfatigue.2019.105376.

[7.28] Bushnell DM, Moses RW. Commercial Space In The Age Of "New Space", Reusable Rockets and The Ongoing Tech Revolutions. 2018.

[7.29] Baiocco P. Overview of reusable space systems with a look to technology aspects. Acta Astronaut 2021;189:10–25. https://doi.org/10.1016/j.actaastro.2021.07.039.

[7.30] Meyer RR, Harwood OP, Harmon MB, Orlando JI. Isogrid design handbook. NASA 1973.

[7.31] Rahimi GH, Zandi M, Rasouli SF. Analysis of the effect of stiffener profile on buckling strength in composite isogrid stiffened shell under axial loading. Aerosp Sci Technol 2013;24:198–203. https://doi.org/10.1016/j.ast.2011.11.007.

[7.32] Jadhav P, Raju Mantena P, Gibson RF. Energy absorption and damage evaluation of grid stiffened composite panels under transverse loading. Compos B Eng 2005. https://doi.org/10.1016/j.compositesb.2005.05.017.

[7.33] Kim TD. Fabrication and testing of thin composite isogrid stiffened panel. Compos Struct 2000. https://doi.org/10.1016/S0263-8223(99)00122-1.

[7.34] Huybrechts SM, Hahn SE, Meink TE. Grid Stiffened Structures: A Survey of Fabrication Analysis and Design Methods. International Conference on Composite Materials 1999.

[7.35] Kim TD. Fabrication and testing of composite isogrid stiffened cylinder. Compos Struct 1999;45:1–6. https://doi.org/10.1016/S0263-8223(98)00124-X.

[7.36] Pettit RG, Wang JJ, Toh C, Metschan S. Validated Feasibility Study of Integrally Stiffened Metallic Fuselage Panels for Reducing Manufacturing Costs Cost Assessment of Manufacturing / Design Concepts. Technical Report: NASA/CR-2000-209342 2000.

[7.37] Haslinger SG, Craster R v., Movchan AB, Movchan N v., Jones IS. Dynamic interfacial trapping of flexural waves in structured plates. Proceedings of the Royal Society A: Mathematical, Physical and Engineering Sciences 2016;472. https://doi.org/10.1098/rspa.2015.0658.

[7.38] Maclin JR. N92-30109 Performance of fuselage pressure structure. 1992.

[7.39] Susmel L, Taylor D. Fatigue design in the presence of stress concentrations. Journal of Strain Analysis for Engineering Design 2003;38:443–52. https://doi.org/10.1243/03093240360713496.

[7.40] Peterson RE, Wahl AM. Two-and Three-Dimensional Cases of Stress Concentration, and Comparison With Fatigue Tests 1936;5.

8 Concluding remarks and future work

This thesis has detailed an investigation of the Isogrid rolling process through experimental implementation. Characterisation of microstructural and mechanical aspects of Isogrid, manufactured via rolling and conventional machining techniques, was undertaken to evaluate and compare both methods.

This chapter discusses the conclusions found throughout the thesis, summarises the key outcomes, and proposes some directions for future work in this field.

8.1 Concluding remarks

The concept of manufacturing grid stiffened structures through the use of a modified rolling process was implemented as detailed in Chapter 4. This proof of concept provided experimental results which demonstrated the feasibility of Isogrid rolling as a manufacturing technique.

- The Isogrid geometry was produced using the modified rolling mill. Initial trials of rolling Isogrid with 3mm thick billets included geometric defects in the rib lattice. The introduction of 4mm billets reduced these effects.
- The tendency for curling was noted in the rolled Isogrid, which is indicative of shear forces acting on the midplane of the structure. The effects of those same shear forces were corroborated within Chapter 5, by the discovery of rotated cube deformation textures in the orientation distribution functions.

In chapter 5, the microstructure of rolled Isogrid was evaluated using advanced optical microscopy, electron backscatter diffraction and microhardness measurement techniques. The comparison between rolling and CNC milling operations to produce Isogrid was greatly enriched through the detailed investigation of the microstructural effects of each manufacturing technique.

- The microstructure of rolled Isogrid was cold worked and the grains had been oriented parallel to the outer contour of its cross section during the rolling process. The CNC milling process did not affect the bulk microstructure. The microstructural refinement introduced by Isogrid rolling was shown in Chapter 6 to improve the strength of the rolled Isogrid structure.
- Rolled Isogrid had less intense deformation textures than those found in the CNC milled Isogrid, which reduced the degree of anisotropy present in the rolled samples. This result was confirmed in Chapter 6, as the rolled Isogrid was more isotropic in tension and bending than the CNC milled Isogrid.
- A variation in the microhardness was observed between the rib and skin sections of rolled Isogrid. Areas of high hardness corresponded with areas of greater cold work and vice versa. The transition regions from high to low hardness were noted in Chapter 7 to be initiation sites of fatigue cracking, which reduced the overall fatigue performance of the rolled Isogrid structure.
- An annealing treatment recrystallised the microstructure of the rolled and CNC milled Isogrid samples. No microstructural variation was seen in the post-annealed rolled Isogrid, indicating the heat treatment had a homogenising effect and removed cold work.

The mechanical behaviour of rolled Isogrid and CNC milled Isogrid was explored through the regimen of tensile and bending tests reported in Chapter 6. Samples were tested in the cold worked and post-annealed conditions to examine the tensile and bending strength, the isotropy of in-plane and out-of-plane mechanical behaviour, and the contribution of cold work to the overall mechanical performance of each sample group.

- Producing Isogrid via rolling increased its capacity to resist static loads when compared to CNC milling for the same geometry. Rolled Isogrid outperformed CNC milled Isogrid in tensile and bending loading regimes, at both 0° and 90° to a primary rib direction.

- The sample groups performed identically in the post-annealing state, indicating that the cold work and microstructural refinement imparted into the rolled Isogrid is responsible for the increase in mechanical properties.
- Rolled Isogrid was shown to be more isotropic than CNC milled Isogrid for in-plane and out-of-plane mechanical properties. The 90° direction was consistently shown to be stronger than the 0° direction in tension and bending for both sample groups. However, the 0° direction was more ductile in tension.

The behaviour of rolled Isogrid under cyclic loading was measured and compared against that of CNC milled Isogrid in Chapter 7. The microstructural variation imparted by the Isogrid rolling process was shown to accelerate crack initiation, hence reducing rolled Isogrid's fatigue performance. However, the use of an annealing heat treatment to homogenise the microstructure was shown to eliminate this effect.

- Rolled Isogrid in its cold worked condition was more susceptible to fatigue failure than CNC milled Isogrid. The fatigue life of rolled Isogrid was three times shorter for low cycle fatigue, diverging to ten times shorter in the higher cycle regime.
- The poor performance of rolled Isogrid was due to increased crack initiation found near rib / skin transitions, where changes in microhardness levels were reported in Chapter 5.
- Implementation of a post-roll annealing heat treatment improved the fatigue performance of rolled Isogrid by an order of magnitude. The same heat treatment was shown in Chapter 5 to recrystallise the microstructure, removing the effects of cold work to create a homogenous microstructure.

The findings presented throughout this thesis have addressed the objectives identified in Chapter 1 to provide a balanced initial assessment of the viability of the Isogrid rolling process for industrial adoption. The concept has been proved to work through experimental implementation, resulting in the successful creation of rolled samples with AA1050. Further, a novel dataset has been generated, characterising the microstructural, mechanical and fatigue properties of rolled Isogrid, with an accompanying identical dataset for CNC milled Isogrid. Static mechanical testing indicates rolled Isogrid possesses improved mechanical properties when compared to a CNC milled equivalent structure; however, the process generates some undesirable effects, such as variation in microstructure, which lead to a reduction in performance under cyclic loading. In conclusion, the proposed rolling method for the industrial mass production of Isogrid has been shown to have merit, but further study of the Isogrid rolling process is recommended to explore these effects and develop the process.

8.2 Future work

The following proposed work would improve understanding of the Isogrid rolling technique and build a scientific knowledge base through which it can be evaluated.

8.2.1 Isogrid rolling of heat treatable aluminium alloys

The microstructural variation reported within rolled Isogrid is a key point of interest for fatigue performance; annealing heat treatments were shown to minimise this variation in AA1050 aluminium to the detriment of overall strength. Heat treatable aluminium alloys (such as 2XXX or 6XXX series) have a greater range of potential heat treatment options to homogenise the final rolled microstructure, such as artificial aging. Artificial aging could be investigated as a method of reducing the variation in microstructure and hardness found within rolled Isogrid, thereby improving its fatigue performance while simultaneously strengthening the final structure. Furthermore, the increased chemical complexity of heat treatable alloys compared to AA1050 presents an opportunity to study the microstructural evolution generated through Isogrid rolling, such as changes in precipitates between areas of high and low plastic deformation.

8.2.2 *Finite element modelling and process optimisation*

The development of a 3D finite element model would enable a parametric investigation into multiple facets of the Isogrid rolling process. The goal of this work is to generate a scientific understanding of the material flow and force interactions present during Isogrid rolling, hence define the limits of the process, optimise geometric variables and process parameters. Finite element modelling of the process for the determination of stress systems within the roll gap would generate useful data on the maximum deformations achievable, clarify the origin of the shear deformation textures reported in Chapter 5 and predict areas of undesirable residual stress. Geometric optimisation of the roller and target geometry based on these analyses could potentially reduce the gradient of plastic deformation present in the rolled Isogrid and compensate for any curvature caused by residual stress based springback. Further finite element modelling could be performed on the resultant rolled Isogrid geometry, to predict its mechanical behaviour (tensile, bending and fatigue performance) and guide the optimisation process. Finite element modelling should be validated via comparison with the results of the Isogrid rolling process as detailed in this thesis.

An example metric to optimise is the maximum ratio of rib height to skin thickness, which is directly related to the mechanical performance of grid stiffened structures in bending. Similarly, a multi-variable optimisation of the groove geometry would be performed to improve the geometric consistency of rib formation. In Chapter 4, the roller grooves were assigned a draft angle of 30° based on an involute relation. The reduction of this angle would improve the mechanical efficiency of the reinforcing ribs in bending; however, a reduced draft angle carries the risk of inhibiting the formed structure from exiting the roll gap. Part of the optimisation study would be performed on a range of draft angles, groove geometries and groove orientations to refine the design of the grooved roller.

8.2.3 Experimental studies of advanced process phenomena

Future investigations of the Isogrid rolling process could vary fundamental process parameters such as process temperature, individual roller speeds, and the force applied in the roll gap. Work on the effects of Isogrid rolling temperature, via either pre-heating or continuous heating of the billet during the process, would present an opportunity to study and control microstructural evolution and rib formation. Variation of roller speed ratios via independent roller speed control would allow research into the shear forces which generated the curling effect as seen in Chapter 4. This work should be accompanied by advanced microstructural characterisation and measurements of residual stresses. The production of larger samples with a high-powered rolling mill would enable application specific studies; for example, rolled Isogrid could be used to fabricate a pressure vessel for performance evaluation in that context.

9 Publications

Garrick, A. J. H., Toumpis, A. I., & Galloway, A. M. (2021). Developing a novel manufacturing method to produce stiffened plate structures. *International Journal of Advanced Manufacturing Technology*, 2805–2813. https://doi.org/10.1007/s00170-020-06525-x

Abstract

Isogrid is a highly efficient stiffened plate structure which was developed in the aerospace industry for use in rocketry and space structures. Its current form is unviable outwith these applications, as the available production methods are expensive due to excessive machining time in addition to considerable material wastage. The method detailed in this body of work was developed to manufacture Isogrid in a more efficient manner, so that its weight-saving properties may become more widely accessible. This novel Isogrid manufacturing process uses a rolling mill with patterned rollers to imprint a 3D structure of ribs into the surface of a billet material. To validate this method, a patterned roller was designed, manufactured and fitted to a rolling mill to produce sheets of aluminium AA1050 Isogrid. This process successfully created Isogrid in a sustainable, rapid manner. The samples produced were tested in 3-point bending and compared against flat plate of the same material. They were found to be 100% stronger in bending compared to a neutral flat plate with a strength shape factor of 1.6 after discounting the effect of cold work.